

## INFORMATION TO USERS

This manuscript has been reproduced from the microfilm master. UMI films the text directly from the original or copy submitted. Thus, some thesis and dissertation copies are in typewriter face, while others may be from any type of computer printer.

**The quality of this reproduction is dependent upon the quality of the copy submitted.** Broken or indistinct print, colored or poor quality illustrations and photographs, print bleedthrough, substandard margins, and improper alignment can adversely affect reproduction.

In the unlikely event that the author did not send UMI a complete manuscript and there are missing pages, these will be noted. Also, if unauthorized copyright material had to be removed, a note will indicate the deletion.

Oversize materials (e.g., maps, drawings, charts) are reproduced by sectioning the original, beginning at the upper left-hand corner and continuing from left to right in equal sections with small overlaps.

ProQuest Information and Learning  
300 North Zeeb Road, Ann Arbor, MI 48106-1346 USA  
800-521-0600

UMI<sup>®</sup>



SOFT-MATERIALS: FROM COLLOIDS ON TEMPLATES  
TO POLYMERS IN NEMATICS

JIAN ZHANG

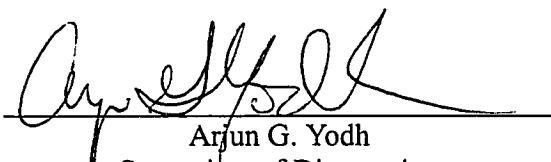
A Dissertation

in

PHYSICS AND ASTRONOMY

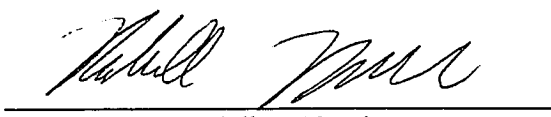
Presented to the Faculties of the University of Pennsylvania in Partial  
Fulfillment of the Requirements for the Degree of Doctor of Philosophy.

2003



---

Arjun G. Yodh  
Supervisor of Dissertation



---

Randall D. Kamien  
Graduate Group Chair

UMI Number: 3109240

Copyright 2003 by  
Zhang, Jian

All rights reserved.

UMI<sup>®</sup>

---

UMI Microform 3109240

Copyright 2004 by ProQuest Information and Learning Company.  
All rights reserved. This microform edition is protected against  
unauthorized copying under Title 17, United States Code.

---

ProQuest Information and Learning Company  
300 North Zeeb Road  
P.O. Box 1346  
Ann Arbor, MI 48106-1346

**COPYRIGHT**

**Jian Zhang**

**2003**

# ACKNOWLEDGMENTS

During my graduate student career I have tried my best to learn how to do good research. During this learning period, I got a lot of help from many people around me.

First of all, I thank my supervisor, Arjun G. Yodh. Under his guidance, I began an adventure to become a good scientist. I benefited and learned a lot from his drive to do creative work, his criticism about what good research is, and his patience with the progress of the work. I think the most important thing I learned from Arjun is that every time when you start a project, you should ask yourself: "What's the new about it?" I believe that Arjun's guidance has helped me to realize how great work is done.

Also, I want to thank two people who helped me to start my experimental research career. One is William J. Work, who taught me how to synthesize colloidal particles; beyond this he showed me how to do research in a systematic way. The other scientist was Hu Gang, who taught me the basics of light scattering and colloid science. I still remember how amazed I was when we used dynamic light scattering to easily measure the size of SDS micelles in solution, which was below 10 nm.

I am grateful to three postdocs: Zvonimir Dogic, Mohammad Islam, and Jean-Christophe

Loudet. They are all excellent researchers. I benefit a lot by working with them. Especially, I collaborated with Zvonimir on the project of polymers immersed in nematic solvents. During this collaboration, I learned to be a careful and creative scientist. From Mohammad, his determination in his work and intuition about his projects show me how good research is done. From JC, I benefited from his systematic and extremely organized approach.

Through my graduate life, I have spent my research period in two groups. I spent one year in Professor Charlie Johnson's group and a little bit more than four years in Professor Arjun Yodh's group. I thank Charlie Johnson's support when I was in his group. There are many persons I have worked with and I think I owe my thanks to them. They are John C. Crocker, Eric Weeks, Sanyan Subrata, Ningping Yang, Keng-hui Lin, Ahmed Alsayed, Daniel Chen, and Mateusz Bryning. Also in my personal life outside of research, I have spent a lot of great time with my friends. They are Qinghua Guo, Min Zhang, Lei Ji, Xin Zhu, Bo Lu, Yong Liao, and Xiunan Xuan.

I am grateful to Professor Paul Heiney for his help during the collaboration of template directed convective assembly. Without his help, this work could have not been done.

I also thank Professor Younan Xia for inviting me to visit his group for one week. During that week, I learned a lot and my knowledge was extended.

Finally, I should thank my parents for their understanding and support.

## ABSTRACT

### SOFT-MATERIALS: FROM COLLOIDS ON TEMPLATES TO POLYMERS IN NEMATICS

Jian Zhang

Advisor: Arjun G. Yodh

We describe two major experimental studies on colloidal systems.

We demonstrate that square two-dimensional grating templates can drive the growth of three-dimensional, face-centered-cubic (fcc) colloidal crystals by convective assembly. The square symmetry [i.e. (100) planes parallel to the substrate] of the underlying templates was transferred to the colloidal crystals and maintained throughout their growth of  $\sim 50$  layers. We characterized crystals grown on flat and on templated substrates using electron microscopy and small-angle x-ray scattering (SAXS). SAXS measurements of the templated samples clearly revealed four-fold diffraction patterns that arise from fcc domains without stacking faults.

In a different vein, we investigated how polymers behave in colloidal nematic liquid crystals. Semi-flexible polymers with persistence lengths varying from 0.05 to 16  $\mu m$  were dissolved in a nematic liquid crystal of rod-like virus fd. The polymers were directly visualized with fluorescence optical microscopy and their fluctuations were quantitatively analyzed. A coil-to-rod transition of the semiflexible polymers was observed when the background phase evolved from isotropic to the nematic phase. We found that semiflexible filaments' long wavelength fluctuations were the result of the tight coupling to the



background nematic field's fluctuation. The Odijk deflection length and the elastic constant of the background nematic phase were extracted from our experimental data.

In addition to the experimental work described above, we have developed a wide range of particle synthesis capabilities in the laboratory. While all of these procedures were based on previous work, in many cases we developed techniques to improve yield and/or generate new kinds of colloidal particles. We used emulsion polymerization and sol-gel process to synthesize organic PMMA colloid particles and inorganic silica and Zinc Sulfide (ZnS) colloid particles. For the PMMA (polymethyl methacrylate) particles, we used surfactant free emulsion polymerization to achieve highly monodispersed particles with sizes larger than 250 nm; for sizes below 250 nm, we turned to emulsion polymerization. For the preparation of silica beads, we largely followed Stober method. For ZnS, we used a controlled homogeneous precipitation of zinc and sulfide ions to fabricate monodispersed submicron particles. Finally we obtained ellipsoidal organic particles with the method of mechanical stretching.

# Contents

<b>ACKNOWLEDGMENTS</b>	<b>iii</b>
<b>1 Introduction</b>	<b>1</b>
1.1 Brief Review of Thermal Colloids . . . . .	3
1.2 Brief Review of Hard Rod Suspension . . . . .	5
1.3 Brief Review on Particle Synthesis . . . . .	7
<b>2 Template-Directed Convective Assembly of Three-Dimensional Colloidal Crystallization</b>	<b>8</b>
2.1 Introduction . . . . .	8
2.2 Two-Dimensional Convective Assembly . . . . .	13
2.3 Three-Dimensional Convective Assembly . . . . .	19
2.4 Template Technique . . . . .	24
2.4.1 Lithography with Photons, e-beam and Scanning Probes . . . . .	25
2.4.2 Soft Imprint . . . . .	26
2.4.3 Self-Assembly . . . . .	27

2.5	Template-directed convective assembly . . . . .	28
2.6	Conclusion and Future Work . . . . .	40
<b>3</b>	<b>Direct Visualization of Polymers in Nematic Liquid Crystals: Coil-to-Rod</b>	
	<b>Transition</b>	<b>42</b>
3.1	Introduction . . . . .	42
3.2	Polymer Flexibility and Configuration . . . . .	47
3.3	Experiment . . . . .	51
3.3.1	fd Virus and Its Phase Behavior . . . . .	51
3.3.2	Preparation of Biopolymers . . . . .	52
3.3.3	Sample Preparation . . . . .	55
3.3.4	Fluorescent Optical Microscopy . . . . .	56
3.3.5	Image Analysis . . . . .	58
3.4	Theoretical Models . . . . .	60
3.4.1	Demixing Phase Behavior and Order Behavior of Binary Rod So-	
	lutions . . . . .	60
3.4.2	Tangent-Tangent Correlation Function . . . . .	65
3.5	Results . . . . .	73
3.5.1	Coil-Rod transition . . . . .	73
3.5.2	Orientational Distribution Function and Order Parameter S . . . .	74
3.5.3	Tangent-tangent Correlation Function (TTCF) . . . . .	83
3.6	Conclusion . . . . .	87

3.7	Appendix . . . . .	87
3.7.1	Appendix A: Isotropic-Nematic Phase Transition . . . . .	87
3.7.2	Appendix B: Order Parameter $S$ and Orientational Distribution Function . . . . .	94
<b>4</b>	<b>Colloidal Particle Synthesis</b>	<b>100</b>
4.1	Introduction . . . . .	100
4.2	Colloidal Particle synthesis . . . . .	101
4.2.1	PMMA Colloidal Particle Synthesis . . . . .	102
4.2.2	Silica Colloidal Particle Synthesis . . . . .	118
4.2.3	ZnS Particle Synthesis . . . . .	122
4.2.4	Synthesis of Ellipsoid Particles . . . . .	127
4.3	Conclusion . . . . .	134
<b>5</b>	<b>Conclusions and Future Work</b>	<b>135</b>

# List of Tables

3.1	Contour length $L_c$ , persistence length $l_p$ and diameter $D$ of the different polymers used in our experiments. . . . .	55
3.2	The Fitting Results of TTCF for the Samples of Wormlike Micelles in fd Solution . . . . .	87
4.1	Physical Properties of Commonly and Uncommonly Used Particles . . .	101
4.2	Recipe of the Synthesis of PMMA 250 nm Seed Particles . . . . .	109
4.3	Recipe of the Synthesis of 420 nm PMMA Particles . . . . .	110
4.4	Recipe of the Synthesis of 70 nm PMMA Particles . . . . .	113
4.5	Recipe of the Synthesis of Monodispersed Silica Particles . . . . .	119
4.6	Particle Diameter ( $\mu\text{m}$ ) of Silica Obtained by Aging at 40 °C for 1 h Solutions of Reactants at Given Concentrations ( $\text{mol dm}^{-3}$ ) and Volumes ( $\text{cm}^3$ ). <sup>a</sup> Indicates a two-step addition of TEOS, as described in the text. <sup>b</sup> Ethanol. <sup>c</sup> Isopropanol. . . . .	121
4.7	Recipe of the Synthesis of Monodispersed ZnS Particles . . . . .	125
4.8	Particle Size Dependence on TAA Concentration. . . . .	126

4.9 PVA We Have Tried in Our Experiment . . . . .	133
---	-----

# List of Figures

1.1	Equilibrium phase diagram from computer simulation for uniformly sized hard spheres (insets are schematic depictions of the various phases). The liquid-crystal coexistence region is $0.494 < \phi < 0.545$ . Face centered cubic structure has the highest entropy for volume fraction $\phi$ larger than $\phi_M=0.545$ and less than crystal close packing 0.7404. The highest volume fraction for amorphous phase is random close packing $\phi_{rcp}=0.63$ , close to which the dynamics of the system is very low, formerly glass phase was attributed to $0.58 < \phi < 0.63$ . . . . .	4
2.1	Sketch of the setup of 2D convective assembly. The inset shows how the water surface deformed by the neighboring particles. Here, $v_w$ is the substrate pulling speed, $v_c$ is the crystal growth speed, $j_e$ is the water evaporation flux along the edge, $l$ is the evaporation length, $j_w$ is the convective water flux, $j_p$ is the convective particle flux, and $h$ is the thickness of the array, which is the same as particles' diameter, $D$ . (from ref. [44]) . . . .	15

2.2	Sketch of the attractive lateral immersion capillary force between two particles partially immersed in water. $\psi_1$ and $\psi_2$ are meniscus slope angles. .	18
2.3	SEM picture of 3D colloidal crystal from 246 nm polystyrene beads. It is prepared by convective assembly from 1 % in volume aqueous solution at room temperature. . . . .	20
2.4	X-ray patterns of the samples prepared by convective assembly. a) The sample is prepared from 1% 246 nm polystyrene beads solution; b) The sample is prepared from 1% 550 nm polystyrene beads solution. . . . .	23
2.5	Cartoon of how a square template can avoid stacking faults. The upper picture shows that if the first layer's structure is hexagonal, as it always is for a flat substrate, and denote its position as A, then there exist twin positions B and C for the spheres to fill at the second layer. The lower picture shows that there is only one way to fill the second layer if the the first layer is a square lattice. . . . .	29
2.6	SEM pictures of 2D convective assembly with templates. The particle size is ~500 nm, and the template periodicity is 550 nm. In a). is line template, and in b). is square template. . . . .	31
2.7	SEM picture of 3D colloidal crystal from ~500 nm polystyrene beads. It is prepared by convective assembly with square template. The template period is 550 nm. The colloidal crystal's structure is fcc. . . . .	32



2.8	Picture of the wetting behavior of a drop of polystyrene beads solution on both glass substrate (left) and on Au/Pd coated substrate (right). The solution's concentration is 0.01 and the bead's size is $\sim 500$ nm. . . . .	33
2.9	Flow chart of how we prepared our template. The basic method used here is imprint technique. . . . .	35
2.10	SEM picture of a portion of our template. The groove spacing is 550 nm, groove depth is 100 to 200 nm, and lateral dimensions are 6 mm $\times$ 18 mm. . . . .	36
2.11	SEM pictures of the crystal convective assembled (a) with template and (b) without template. The particle diameter was $\sim 500$ nm, and the template period was 550 nm. . . . .	37
2.12	Diffraction pattern from convective assembled crystals (a) Hexagonal domains (without template) and (b) Square domains (with template). In Fig (b), the superimposed grid facilitates recognition of the square symmetry. . . . .	39
3.1	Sketch of how the monomers are bound together. Bond angle ( $\theta$ ) and dihedral angle ( $\phi$ ) are as shown in the figure. . . . .	47
3.2	The scheme of a polymer; the conformation of the polymer is parameterized by s. . . . .	49

3.3	Phase diagram of fd solution. The filled circle points are experimental data for nematic phase, the open circle points are experimental data for isotropic phase. The upper curve is theoretical curve for nematic phase, and the lower curve is theoretical curve for isotropic phase. The region between these two curves are isotropic-nematic coexistence region. (From ref. [109].) . . . . .	53
3.4	The absorption and emission curves of rhodamine-phalloidin. The absorption wavelength is 542 nm and the emission wavelength is 565 nm [110].	58
3.5	Figure (a) is a image of elongated actin filament. Figure (b) is a plot of the Gaussian fit of the intensity profile. The dark line is the intensity profile and the light line is the Gaussian fitting result. Figure (c) exhibits the fitting result over the real actin filament. Figure (d) is the fitting result. . .	59
3.6	Cartoons of this theory's two main predictions [18]. Figure a) shows in a binary solution long rods have better alignment than short rods. Figure b) shows in a binary solution the long rods will phase separate out from the short rods when their length ratio exceeds 3.2. . . . .	66
3.7	Schematic of a polymer in the background nematic field; the conformation of the polymer is parameterized by $\vec{R}(z) = (\vec{R}_\perp(z), z)$ . The nematic director points along the z axis. . . . .	69

3.8	Images of fluorescently labelled biopolymers in the isotropic (left) and nematic (right) phase of fd virus. Figures (a)-(d) are, respectively, the images of actin, wormlike micelles, neurofilaments and DNA. (e) A sequence of images illustrating an actin filament escaping from a hairpin defect. The scale bar indicates $5\text{ }\mu\text{m}$ . (f) Schematic of a biopolymer in the background nematic field; the conformation of the polymer is parameterized by $\mathbf{R}(z) = (r_x(z), r_y(z), z)$ . The nematic director points along the $z$ axis. . . . .	75
3.9	Schematics of definitions of the angles. Figure a) is the definition of angle $\theta_0$ . Figure b) is the definition of angles $(\theta, \phi)$ . . . . .	76
3.10	The order parameter of actin filaments ( $S_{actin}$ ) vs. the order parameter of the background fd nematic ( $S_{fd}$ ). Dashed line is a guide to the eye. The contour length of actin filaments is $15\text{ }\mu\text{m}$ or higher. Inset: The orientational distribution function (ODF) of actin filaments. The ODF is well approximated by a gaussian for a wide range of concentrations. . . . .	81
3.11	$S_{actin}$ vs. contour lengths of actin. The concentrations of the background nematic fd are 41 mg/ml (circles, $S_{fd}=0.75$ ) and 28 mg/ml (squares, $S_{fd}=0.855$ ). Dashed lines are a guide to the eye. . . . .	82

3.12	The x component of the tangent-tangent correlation function for worm-like micelles measured at three different fd concentrations ( $c_{fd}$ ). With increasing fd concentration, the overall magnitude of the correlation function correlation decreases. The solid lines are theoretical curves generated from our theoretical model with the best-fit parameters listed in Table 4.2. Inset: TTCF for the lowest concentration of the fd virus. The dashed and dotted lines are, respectively, the contributions from the first and the second terms in the theoretical model. The data points below $0.5 \mu m$ are unreliable and have been excluded from the fitting. . . . .	86
4.1	Sketch of the experiment setup of our surfactant free emulsion polymerization of PMMA particles. The milky solution is the PMMA colloidal dispersion in reaction. . . . .	107
4.2	Flow chart of the synthesis of 250 nm PMMA particles. . . . .	108
4.3	Flow Chart of how to use semi-batch method to grow particles with size bigger than 250 nm. . . . .	111
4.4	(a) A bottle of 248 nm PMMA particles synthesized by us. The particles crystallize at the bottom of the bottle and give iridescent color. (b) Surface crystallization of 580 nm PMMA particles synthesized by us. . . . .	111
4.5	Flow Chart of how to synthesize 70 nm PMMA particles. . . . .	113
4.6	Flow Chart of how to synthesize amino surface grouped PMMA particles. . . . .	115
4.7	SEM picture of $\sim 300$ nm PMMA particles we synthesized. . . . .	116

4.8	Flow Chart of how to synthesize fluorescently labelled, nonaqueous PMMA particles. . . . .	117
4.9	SEM picture of $\sim 500$ nm silica particles we synthesized. . . . .	120
4.10	Flow Chart of how to synthesize monodispersed silica particles. . . . .	121
4.11	Flow Chart of how to synthesize fluorescently labelled silica particles. . .	121
4.12	Flowchart of how to synthesize monodispersed ZnS particles. . . . .	125
4.13	SEM picture of $\sim 500$ nm ZnS particles we synthesized. . . . .	126
4.14	SEM picture of the rods we made. a) is a sample with dilute ellipsoid concentration. From which we can see individual rods' configuration. b) is a sample with high ellipsoid concentration. . . . .	131

/

# Chapter 1

## Introduction

This thesis is concerned with a subfield of soft condensed matter physics, namely complex fluids and colloid science. Advances in complex fluids and colloid physics touch on a variety of problems at the meso- and nano-scale. These problems are relevant to cell biology on the one hand, and nanotechnology on the other.

Colloid refers to a suspension of particles with size ranging from 10 nm to 10 micron. Colloid science originated from observations of the behavior of such minute particles in nineteenth- and early twentieth century. This movement is referred to as Brownian motion. Nowadays interest in colloids has resurrected because of requirements from both academics and industry. We have learned to directly measure the size, shape, concentration of the suspended particles, as well as the forces between particles. Monodispersed colloidal particles can be synthesized and are used as model particles for systematic research into self-assembly and statistical physics. In industry, colloids have played a role

in enhanced oil recovery, the development of new fuels, environmental pollution, food products, paints, ceramics fabrication, and biotechnology.

Most recently, colloid science and complex fluid research has become an extremely active field. There are many reasons for this increase in activity, but most are experimental. First, we are readily able to directly visualize particle motion with optical microscopy; three-dimensional (3D) confocal microscopy further enable us to reconstruct the 3D configurations of assemblies in suspension. Secondly, sophisticated software has been developed to digitize these optical microscopy images of colloidal particles, and then tracking the particles is possible. The tracking methods offer an opportunity to quantitatively describe the colloidal suspension [1], and to investigate the kinetics of various phase behaviors, such as colloidal crystallization [4], gelation [3], and glass formation [2]. Thirdly, the development of a broad range of self-assembly has made colloidal crystals an attractive candidate for “bottom-up” synthesis of photonic bandgap (PBG) materials. PBG materials, in turn, have broad high-tech application potential. Finally, substantial cell biology and biotechnology research overlaps with colloid science because micro-organisms, organelles and related structures are in the same size range as colloidal particles, and in some cases exist under similar conditions.

## 1.1 Brief Review of Thermal Colloids

In the “thermal” colloid world, the equilibrium state of the suspension is the state of minimum free energy. When the interactions between colloidal particles are hard-core repulsive, then the equilibrium phases have maximum entropy, and the phase behavior is temperature independent. Because of steric repulsion and finite size effects, there is always a region around each particle which is inaccessible to the centers of the other particles. This region of space is referred to as excluded volume. Packing entropy is connected to the excluded volume effect. For example, in order to create more free space for themselves, suspended particles might spontaneously organize into a lattice structure. Packing entropy generally favors ordered phases. Another kind of entropy is mixing entropy, which favors disordered phases. In a colloidal suspension, when the particle concentration is sufficiently high, the system’s packing entropy will dominate its mixing entropy [5].

Thus ordered phases (such as face-centered-cubic (fcc) crystals) are produced in simple hard-core systems, and entropy is simultaneously maximized. Because the free energy difference between the fcc structure and the hexagonal closed packed (hcp) structure is so tiny, people usually observe random closed packed (rcp) structures in practice [4]. For a monodispersed system of hard spheres, however, these problems have been extensively studied and the detailed phase behavior is as follows. When the sphere volume fraction is below 0.494, a liquid state is the stable phase; when the sphere volume fraction is between the range of 0.494 to 0.545, there exists a coexistence of liquid and solid states; when the volume fraction is above 0.545 and below 0.63, the stable state is fcc crystal, and there



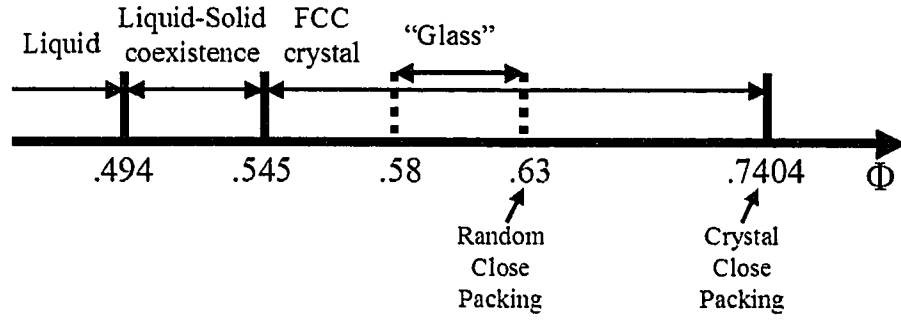


Figure 1.1: Equilibrium phase diagram from computer simulation for uniformly sized hard spheres (insets are schematic depictions of the various phases). The liquid-crystal coexistence region is  $0.494 < \phi < 0.545$ . Face centered cubic structure has the highest entropy for volume fraction  $\phi$  larger than  $\phi_M = 0.545$  and less than crystal close packing  $0.7404$ . The highest volume fraction for amorphous phase is random close packing  $\phi_{rcp} = 0.63$ , close to which the dynamics of the system is very low, formerly glass phase was attributed to  $0.58 < \phi < 0.63$ .

exists a glass formation window between  $0.58$  and  $0.63$  [6, 7, 8, 9]. In the glassy region, the particle suspension is trapped in local free energy minima. In this state, the particles are randomly packed. Because the diffusion of those particles is small, they remain in a box formed by their neighbors [2]. A phase diagram for this system is shown in Fig. 1.1.

Another interesting set of physical system is the binary mixture of two different sized particles. In this case, an ordered crystalline phase of large diameter particles can spontaneously formed by increasing the disorder of the small particles [43]. This “depletion” effect is also an entropy driven transition.

In Chapter 2 we will describe a set of experiments that explores a non-equilibrium crystallization process: convective assembly. We will show how to use square templates to modify the convective colloidal crystallization processes, and achieve colloidal crystals with few stacking faults. We also use optical imaging and small-angle X-ray scattering

in our experiment to confirm the final crystal structure, which has four-fold symmetry with a square template, compared to six-fold symmetry without template. Ultimately our understanding of these processes requires insight about equilibrium packing as well as convective effect. These experiments introduced an important new knowledge for colloid self-assembly.

## **1.2 Brief Review of Hard Rod Suspension**

The other major topic of this thesis concerns semi-flexible polymers in colloidal nematic liquid crystals composed of rod shaped colloidal particles. Because of their anisotropic shape and their internal motions, these systems are in many ways richer than the system of colloidal spherical particles. The rod system has orientational order, in addition to positional order. Consequently, these systems exhibit isotropic, nematic and even smectic phases as its constituent concentration is increased [10]. In the nematic phase there is only long range orientational order. The orientational order and accompanying phase behavior is unique to anisotropic particle colloids. These anisotropic phases are, of course, used in industry for display devices based on molecular liquid crystals, and for Bragg switches [11].

Extensive studies, both theoretical and experimental, have been carried out on isotropic-nematic phase transition of a monodispersed rod system. Onsager did pioneering theoretical work on the phase behavior of hard rods in suspension [10]. In his theory, he carried out a virial expansion of the hard rod's free energy up to the second order term. Taking an

assumed form for the rod's orientational distribution function, he predicted an isotropic-nematic phase transition when the rod concentration exceeded  $4\frac{D}{L}$ , where  $D$  is the diameter of the rod and  $L$  is the length of the rod. He also extended the theory to the charged hard-rod systems.

Later on, Cotter and coworkers developed a scaled particle theory to describe the hard-rod isotropic-nematic phase transition [15, 16]. In their theory, they took into account the third and higher virial coefficients in an approximate way. As a continuation, Chen investigated the rod flexibility effect on the isotropic-nematic(I-N) phase transition [17]. In general, flexibility increases the required rod concentration at I-N coexistence, and decreases the width of the coexistence region. It also decreases the solution order parameter in coexistence region.

Experimentally, Dogic and Fraden systematically studied hard-rod's phase behavior by using hard-rod-like monodispersed fd virus solution as a model system [12, 13]. In their work, they found Onsager's theory was in fairly good qualitative agreement with the fd virus suspension's isotropic-nematic phase behavior. They also found other interesting phenomena such as the isotropic-smectic phase transition in fd and in polymer-rod mixtures [14]. Lekkerkerker and coworkers studied binary mixtures of long hard rods and short hard rods [18]. They found that longer rods have a higher order parameter than the short rods even when they are in the same dispersion. In addition, they predicted the existence of an isotropic-nematic-nematic phase separation, i.e. a demixing phase transition when the length ratio exceeds 3.2. When the shorter rods' length is negligible compared

to longer rods' length, then the shorter rods can be viewed as a continuous background. Kamien developed a theory of polymers in such nematic solvents [19]. He predicted that the polymer would be elongated in such nematic fields.

In Chapter 3 of this thesis we describe experiments wherein we experimentally immersed four different fluorescently labelled biopolymers in an fd virus nematic solvent. The four biopolymers were DNA, neurofilaments, wormlike micelles, and actin. We observed a coil-to-rod conformation transition of the biopolymers in three of the four polymers dissolved in the nematic fd solvent. This transition occurred when the solvent changed from isotropic to nematic phases. For DNA, we observed demixing. With fluorescent optical microscopy and quantitative image analysis, we are able to investigate the polymer order parameter behavior in the fd virus nematic solvent. Furthermore, we studied the tangent-tangent correlation function (TTCF) of the polymer to get further understanding of the polymer's conformation in nematic solvent. These are the first measurements of the biopolymer coil-to-rod transition.

### **1.3 Brief Review on Particle Synthesis**

Finally in Chapter 4 of this synthesis we describe our techniques for colloidal particle synthesis. While some of these basic ideas are well known, in many cases significant innovations were introduced. These particle synthesis provide the background materials that is critical for many of the experiments done in our labs.

## **Chapter 2**

# **Template-Directed Convective Assembly of Three-Dimensional Colloidal Crystallization**

### **2.1 Introduction**

It is difficult, but desirable, to create patterned nano- and microscale materials ordered in three dimensions. These kinds of materials can have novel optical properties [34, 35], potentially leading to new classes of optical filters, switches and photonic band gap materials [36, 37, 38]. Alternatively, precision mesoporous materials have a wide range of potential chemical applications, for example, as catalytic supports [39] and separation media [40, 41].

One important route for creation of three-dimensional patterned materials is through self-assembly. Under the right conditions, a variety of colloidal particle species can assemble spontaneously into ordered phases. For example, excluded volume effects at high concentration induce monodispersed, sterically stabilized PMMA particles in solution to form crystalline phases, rather than liquid phases in thermal equilibrium [42]. In a different vein, Dinsmore and coworkers used entropic depletion effects to grow ordered colloidal crystals out of suspensions of binary mixtures of two different sized particles [43]. The particle volume fraction required for formation of the crystalline phase transition, in this case, is much lower for binary suspensions compared to the monodispersed suspensions.

Beyond the thermal equilibrium techniques, researchers have explored the use of external fields for synthesis of colloidal array. van Blaaderen and coworkers combined sedimentation in a gravitation field and the template technique to achieve template-directed epitaxial growth of colloidal crystals [44]. Using this method they fabricated for the first time pure face-centered-cubic(fcc) structured colloidal crystals, in contrast to the random-closed-packed(rcp) structures achieved by most methods without templates. Yeh and coworkers induced formation of a variety of ordered planar structures by applying normal A.C. and/or D.C. electric fields to the system [45]. More recently, by applying an electric field to an organic solvent containing fluorescently dyed and monodispersed PMMA particles, Yethiraj and van Blaaderen synthesized body-centered-cubic (bcc) and rcp colloidal crystals, and new phases, such as space-filling tetragonal (sft),

body-centered-orthorhombic (bco), and body-centered-tetragonal (bct) [46]. Both the Whitesides group and the Wiltzius group showed how to grow 2D ordered structures against a chemically modified template [47, 48]. With injection forces, Xia's group managed to grow high quality colloidal crystals [49]. Finally the Nagayama group and the Colvin group developed a convenient way to grow highly ordered colloidal crystal with so called convective assembly method [50, 51, 52, 53].

Convective assembly is arguably the simplest method for the creation of ordered particle structures. Pioneering work in convective assembly was done by the Nagayama group [51, 52]. Motivated by the observation that a drop of monodispersed colloidal solution will crystallize during the drying process, the Nagayama group carried out extensive work understanding how this crystallization process occurred. They found convective flow played an important role during the crystallization process. Thus they defined this process as convective assembly. As was the case with Langmuir-Blodgett films, they grew monolayers of 2D hexagonal colloidal crystals by controlling the vertical speed at which they pulled a hydrophilic substrate up and out of a monodispersed colloidal solution [51, 52]. Later on, the Colvin group discovered that high quality three-dimensional (3D) colloidal crystals are produced by simply leaving the substrate in the solution and waiting for the solvent to dry [53]. The simplicity of the procedure motivated many other researchers to do further creative work on convective assembly. As an example, van Bladeren group used convective assembly to achieve layer-by-layer growth of a binary crystal [54]. With this method, they made hexagonal non-closed-packed colloidal structures. As a further step of

their convective assembly research, the Colvin group succeeded in fabricating heterostructures with potential for industrial application [55].

In the 3D convective assembly scheme, a colloidal crystal is formed through the evaporation of a suspension solvent containing monodispersed colloidal particles. The evaporation process causes suspended particles to flow from the bulk liquid to the drying edge, where they assemble and crystallize. Convective assembly is controlled by several factors that are not as yet fully understood: surface tension tends to pull the particles together to form closed packed two-dimensional structures, and crystallization is facilitated via nucleation onto these two-dimensional structures. The resulting crystals are closed packed with triangular (111) planes parallel to the substrate. The resulting colloidal crystal is generally neither fcc, nor hcp, but random closed-packed (rcp) with a lot of stacking faults. Ultimately these stacking faults will have a negative impact on, for example, the photonic properties of the nanoscale material.

In the two-dimensional convective assembly process, a crystal monolayer is formed as the solvent evaporates. When the fluid thickness is comparable to the particle's diameter, capillary forces pull the particles together into contact with one another. On a flat surface, planar close-packed triangular crystals form because these structures have the highest packing density. Templating the surface can get around the close-packed structure and form new structures.

Thus far, templating has been used in convective assembly to produce ordered two-dimensional structures: Ye and coworkers grew various 2D structured colloidal array on



a periodic one dimensional template [68]. Later on, Kim's group fabricated a bilayer colloidal structure out of 2D template [69]. Square templates were used by van Blaaderen and coworkers in their sedimentation work [44]. Lin and coworkers combined depletion effect and the square template technique together to grow various equilibrium colloidal structures [56]. Recently Xia's group succeeded in adding templates to its injection assembly method to nucleate 3D fcc colloidal crystals [57].

In our experiment, we demonstrated that two-dimensional square grating templates can be used to grow three-dimensional fcc colloidal crystals by "convective assembly". The square symmetry [i.e., (100) planes parallel to the substrate] of the template is transferred to the colloidal crystal and maintained throughout its growth. Crystals with thickness of  $\sim 50$  layers are grown. Using scanning electron microscopy (SEM) and small-angle x-ray scattering (SAXS) we characterize the square-symmetric structures and compare their yield on templates with different material compositions. SEM measurements are useful to observe isolated crystallites, and SAXS provides more complete information about bulk samples. We also describe in situ microscopic observations of the growth process. Our work shows that the natural tendency for convective assembly to form close-packed planes can be overcome in two and even three dimensions. Our work also provided detailed information about bulk (3D) structures due to convective assembly, with and without templates.

In this chapter, we review 2D convective assembly in §2.2, and 3D convective assembly in §2.3. We also review the template technique in §2.4. In §2.5 we describe how we combine convective assembly and the template technique together to grow 3D ordered

colloidal crystals.

## 2.2 Two-Dimensional Convective Assembly

People have noticed for a long time that two-dimensional (2D) latex crystals can be formed on top of a flat hydrophilic, solid substrate by drying a drop of aqueous suspension of monodispersed colloidal particles [58, 59, 60, 61, 62, 63, 64]. K. Nagayama's group was the first to start systematic work on this phenomenon and try to understand the basic mechanism [51]. Ultimately, they devised a scheme for colloidal crystallization during the solution drying process, and subsequently developed a clever method to grow ordered 2D colloidal crystals [52]. Because convective flow plays a key role in the assembly process, K. Nagayama and coworkers called this colloidal self-assembly process "convective assembly".

The experimental apparatus used by K. Nagayama and coworkers to grow well ordered 2D colloidal crystal is shown in Fig. 2.1. Briefly they insert a hydrophilic flat substrate, usually a glass slide, into an aqueous reservoir solution of monodispersed colloidal particles. Because water wets the hydrophilic substrate, water will form a thin meniscus layer at the air/water/substrate interface. The thickness of the meniscus layer is the same order of magnitude as the particle size. Thus, as shown in the inset of Fig. 2.1, the particles will protrude out of the water surface and deform the shape of water surface. This deformation will induce a strong capillary force among the neighboring particles. This strong

force overcomes the Brownian force and pulls the particles together to form a high area-packing-fraction 2D structure. Thus, a triangular, closed-packed 2D colloid crystal will form at the edge of the meniscus. Another consequence of the deformation of the water surface is that water evaporates much more quickly at the edge than in the bulk. This rapid evaporation induces a steady convective water flow from the bulk to the edge. This water flow transports particles from the bulk to the edge and thus continues the crystallization process.

To summarize, the entire scheme is composed of two repeating steps: 1) The capillary forces drive particles to the edge of the meniscus layer where they crystallize; 2) The convective water flow transports particles from the bulk to the edge wherein crystallization continues. As long as the substrate is pulled with exactly the same speed as the crystal growth speed, a continuous, two-dimensional, closed-packed triangular structured colloidal crystal array is formed. With this method, K. Nagayama and coworkers managed to grow polycrystalline, closed-packed triangular structured monolayers from polystyrene particles with diameters ranging from 79 *nm* to 2106 *nm*. When water at the meniscus layer evaporates too fast, the particles do not have enough time to relax into the equilibrated mono-domain structure. This is a possible origin for defects in the polycrystalline domain.

We next describe existing models for 2D convective assembly process. They provide a basis for understanding 3D convective assembly, albeit, no theoretical treatment exists that thoroughly explains this (i.e. the 3D) process. There are two mass conservation processes

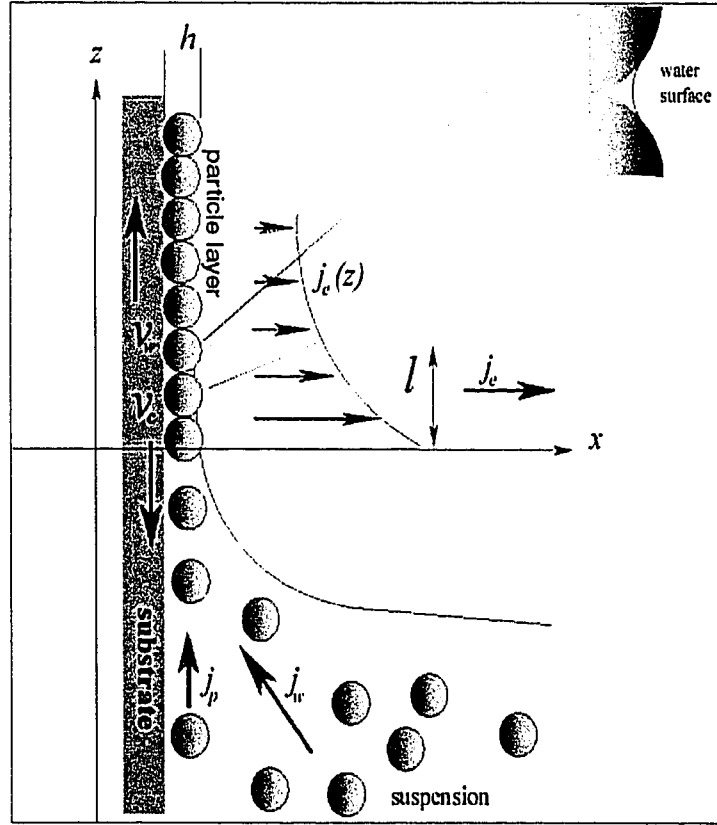


Figure 2.1: Sketch of the setup of 2D convective assembly. The inset shows how the water surface deformed by the neighboring particles. Here,  $v_w$  is the substrate pulling speed,  $v_c$  is the crystal growth speed,  $j_e$  is the water evaporation flux along the edge,  $l$  is the evaporation length,  $j_w$  is the convective water flux,  $j_p$  is the convective particle flux, and  $h$  is the thickness of the array, which is the same as particles' diameter,  $D$ . (from ref. [44])

during convective assembly: 1) The water consumed by the quick evaporation at the edge is compensated by the water transported by convective flow from the bulk; 2) The particles consumed by crystallization process at the edge are compensated by particles transported by convective water flow from the bulk. We define  $j_w$  as water convective flux, and  $j_p$  as particle convective flux. Since the particle flux is driven by the water flux, we can use a parameter,  $\beta$ , to link them together:

$$j_p = \frac{\beta\phi}{1-\phi} j_w. \quad (2.1)$$

where  $\phi$  is particle's volume fraction. The value of  $\beta$  varies from 0 to 1. The exact value of  $\beta$  depends on the density mismatch between particles and water, and the viscosity of the suspension. The transported particle speed is usually slower than the surrounding transporting water speed. Then there will exist a viscous force to drag the particles along the flow to the edge. And it is this viscous force that balances the effective weight of the particles. Thus,  $\beta$  will be 1 for a density matched particle solution. For heavier particles,  $\beta$  will be smaller.

It is too complicated for us to investigate the details of the evaporation along the meniscus layer. For simplicity, we just assume the evaporation happens uniformly along a region with length,  $l_e$ , which should be some fraction of the total length of the meniscus layer. We define the uniform evaporation flux as  $j_e$ . Convective water flow will stop at the crystal leading edge as shown in Fig. 2.1. We define the thickness there as  $h_f$ . From the

conservation of water mass, we get:

$$h_f j_w = l_e j_e. \quad (2.2)$$

If we define  $v_c$  as crystal growth speed,  $h$  as particle diameter, and  $\epsilon$  as the area fraction of the closed-packed, 2D triangular crystal, whose value is around 0.91. We can get the particle conservation equation as below:

$$v_c h \epsilon = h_f j_p. \quad (2.3)$$

Plug equation 2.1 and equation 2.2 into equation 2.3, we finally get the expression for the crystal growth speed as:

$$v_c = \frac{\beta j_e \phi}{h \epsilon (1 - \phi)}. \quad (2.4)$$

From equation 2.4, we can see that, for dilute particle suspensions, the crystal growth speed is proportional to the particle volume fraction. Also, the more hydrophilic the substrate is, the more quickly the crystal will grow.

As we have discussed above, convective water flow plays an important role in colloidal crystal growth process, but it is the capillary force which drives the particles together to crystallize. The origin of the lateral immersion capillary force is the superposition of the deformations produced by the immersed neighboring particles. This force can be attractive, or repulsive. The sign of the force is determined by the signs of the meniscus

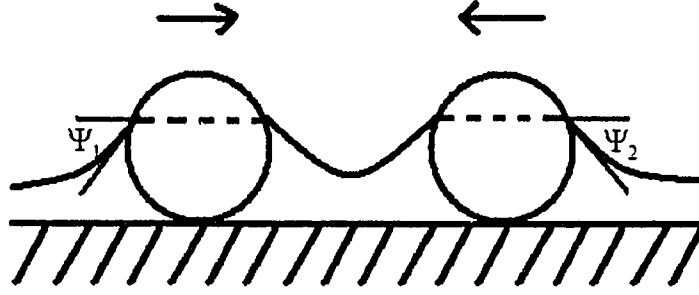


Figure 2.2: Sketch of the attractive lateral immersion capillary force between two particles partially immersed in water.  $\psi_1$  and  $\psi_2$  are meniscus slope angles.

slope angles  $\psi_1$  and  $\psi_2$  at the two contact lines between the water and the particles, as showed in Fig. 2.2. If  $\sin \psi_1 \sin \psi_2 > 0$ , the capillary force is attractive; if  $\sin \psi_1 \sin \psi_2 < 0$ , the capillary force is repulsive. For hydrophilic particles immersed in water,  $\psi_{1,2} > 0$ , so the immersion capillary force is attractive. It is a tedious process to deduce the final analytical expression for the lateral capillary forces. Here we just discuss the final results. Nagayama and coworkers have proved that the immersion capillary force is similar to electrostatic charge interaction [65]. They define capillary charge as  $Q_k$ :

$$Q_k = r_k \sin \psi_k, \quad k = 1, 2. \quad (2.5)$$

where  $r_k$  and  $\psi_k$ ,  $k = 1, 2$ , are the contact lines radii of the two interacting particles and meniscus slope angles. The analytical expression for the immersion capillary force is:

$$F = 2\pi\gamma Q_1 Q_2 q K_1(qL). \quad (2.6)$$

where  $\gamma$  is the surface tension,  $K_1$  is the modified Bessel function,  $L$  is the distance

between two particles, and  $q^{-1}$  is the capillary length, defined as

$$q^{-1} = \left(\frac{\gamma}{\Delta\rho g}\right)^{1/2} \quad (2.7)$$

where  $\Delta\rho$  is the density mismatch between the particle and water. For the case of silica beads partially immersed in water,  $q^{-1} = 2.7mm$ . We can see that the capillary force is really a long range interaction for colloidal particles ( $q^{-1}/R \sim 10^3$ ). For  $L \ll q^{-1}$ , Equ. 2.6 can be approximated as:

$$F = 2\pi\gamma \frac{Q_1 Q_2}{L}. \quad (2.8)$$

We can see that the magnitude of the immersion capillary force is inverse to the distance between the particles, and behaves the same as Coulomb charge interaction. For the case of micron sized silica beads partially immersed in water, the capillary force between them is  $\sim 10$  nN when the inter-particle distance is about ten particles' diameter. This is about seven orders higher than Brownian force ( $\frac{k_B T}{R} \sim fN$ ). So obviously the capillary force alone is strong enough to pull the particles together to crystallize, and completely dominates thermal interactions.

## 2.3 Three-Dimensional Convective Assembly

It is much more desirable to grow a 3D colloidal crystal than a 2D one, since 3D colloidal crystal has much broader and better application potential. For example, a photonic



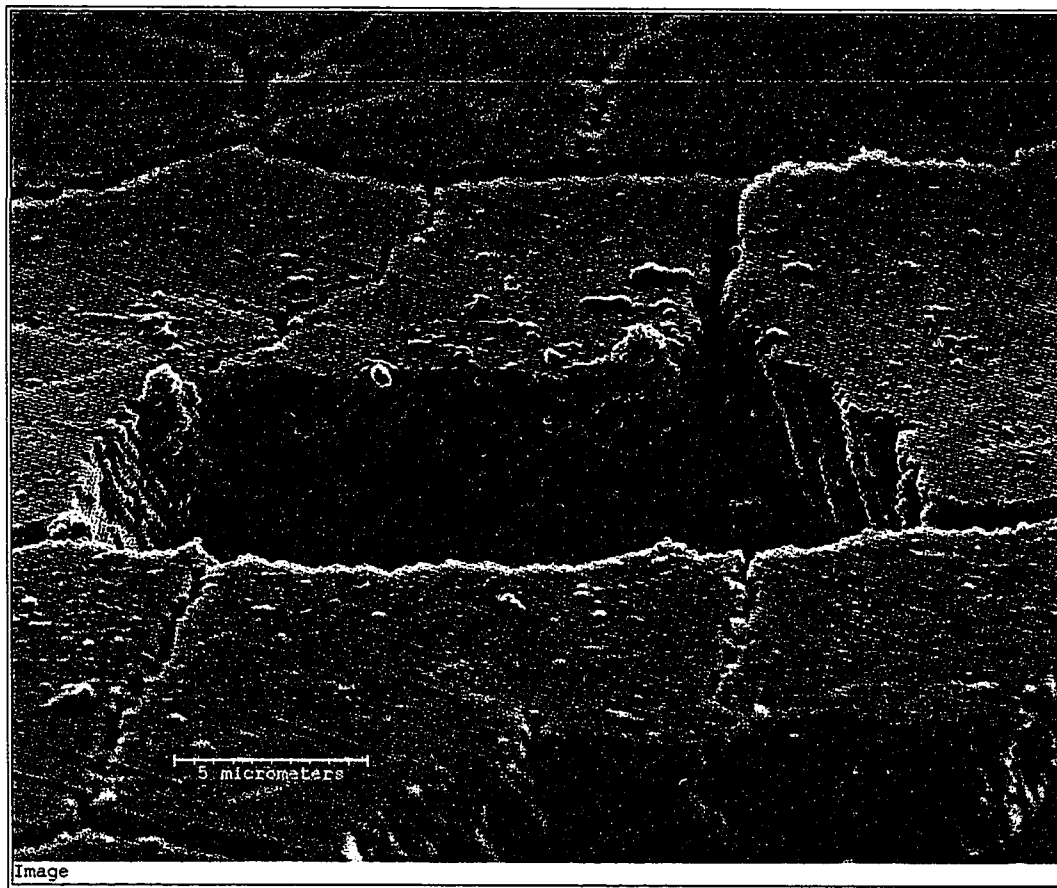


Figure 2.3: SEM picture of 3D colloidal crystal from 246 *nm* polystyrene beads. It is prepared by convective assembly from 1 % in volume aqueous solution at room temperature.

bandgap (PBG) material requires full 3D ordering from colloidal crystal to achieve a complete photonic band gap. Indeed, this was V.L. Colvin's group's significant breakthrough related to the convective assembly method. With the modified convective assembly technique, they achieved 3D colloidal crystal (or at least a closed-packed structure) [53]. The modification they made was simple: leave the substrate in the monodispersed colloidal solution (instead of pulling it up with some appropriate speed), and let the solvent evaporate.

The setup they used for 3D convective assembly is similar to the 2D case, discussed in §2.2. In order to ensure the substrate is perfectly hydrophilic, they pay a lot of attention to the cleanliness of the set-up. They clean the glass microslides by soaking them in a chromic-sulfuric acid solution overnight, and then rinsing them with ultrapure water from a Milli-Q water purify system. They use a cleaned microslide as the substrate and place it into a glass vial containing monodispersed silica sol solution. They clean the glass vial in the same way as they clean the glass microslides. The cleaned glass vial contains the colloidal solution. They put the entire apparatus on a vibration-free bench, keep it at room temperature, and wait the solvent to dry. In their experiments, they synthesized 200 nm to 500 nm monodispersed silica beads themselves for the purpose of convective assembly. The solvent they used is ethanol. The solution's concentration is around 1% in volume. Eventually, they obtained high quality 3D colloidal crystals with iridescent color. Their SEM pictures show high quality colloidal crystals with the structure as rcp. They also noticed that the number of layers of the colloidal crystal is proportional to the colloidal particles' volume fraction in solution, and inverse proportional to the particles'

diameter.

Later, V. Truon's group did a systematic work on the temperature's effect on the final colloidal crystal's quality [66]. In their experiment, the colloidal solution is composed of 0.5 % (v/v), 310 nm, polystyrene beads in water. They did the experiment at three different temperatures: 45°C, 55°C, and 65°C respectively. They find that 55 °C is the optimum temperature to achieve highest quality colloidal crystal.

We repeated these experiments with both silica beads and polystyrene beads. The solvent we used is water. We found that for silica beads, convective assembly works well for particle sizes smaller than 400 nm; while for polystyrene beads, convective assembly works well for particle sizes smaller than 500 nm. One colloidal crystal achieved by us through convective assembly is shown in Fig. 2.3. The crystal is about 50 layers. The structure of the crystal is fcc. We also did X-ray measurements to characterize our crystal quality. For good quality colloidal crystals, we saw a well defined 6 spot diffraction pattern; while for amorphous samples, we saw "liquid" ring diffraction patterns. As shown in Fig. 2.4(a), the sample assembled from 246 nm sized polystyrene particles shows a well defined 6 spot pattern, which indicates that good quality of colloidal crystal is obtained for the sample; while in Fig. 2.4(b) the sample assembled from 550 nm sized polystyrene particles shows liquid ring like diffraction pattern, which indicates amorphous structure is obtained for the sample. This proves convective assembly only works for polystyrene particles with diameter below 500 nm.

The mechanism behind 3D convective assembly has not been understood very clearly

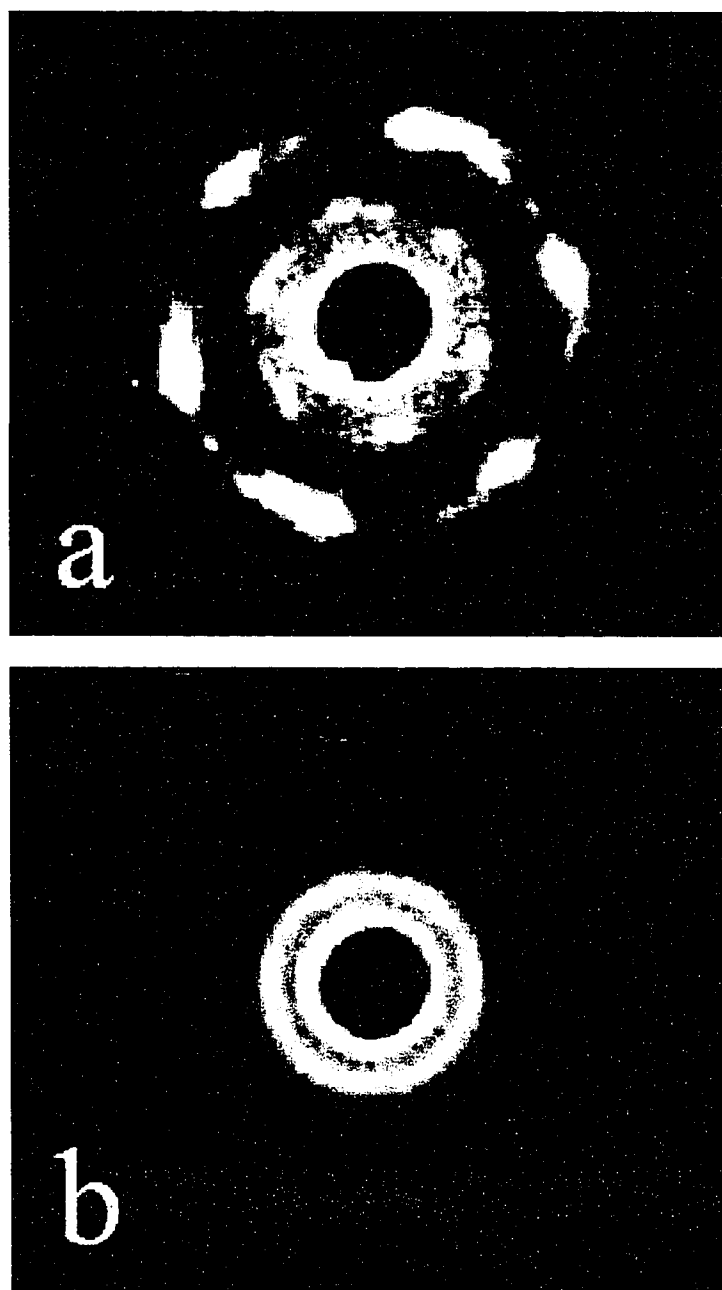


Figure 2.4: X-ray patterns of the samples prepared by convective assembly. a) The sample is prepared from 1% 246 nm polystyrene beads solution; b) The sample is prepared from 1% 550 nm polystyrene beads solution.

yet. Colvin and her coworkers speculate 3D convective assembly shares the same mechanism with 2D convective assembly. But they do not give a clear picture of how the crystal evolves from monolayer to multilayers. By direct microscopic visualization, we find that the 3D convective assembly's mechanism was rather different from the 2D case. For 2D convective assembly, the driving force of crystallization is the capillary force, while for 3D case, the driving force should include excluded volume effects.

We used optical microscopy to investigate the real-time crystallization of a drop of colloidal suspension on a glass coverslip. This slightly different system shares some of the same mechanisms as the three-dimensional convective assembly processes of our primary experiments. By direct visualization, we noticed that (except in the area near the drying edge) the crystallization process appeared to be similar to the equilibrium hard-sphere (Kirkwood-Alder) phase transition; the high local particle concentration required for the transition was driven by convective flow. The particle's concentration was higher near the substrate, and crystallization started from the substrate. Thus many of the standard considerations about crystallization kinetics may apply to this system.

## **2.4 Template Technique**

Fabricating high quality templates has both academic and industrial importance. There exist at least three strategies to synthesize templates: i) lithography with photons, e-beam, and scanning probes; ii) soft imprint (replication against molds via physical contact), and iii) self-assembly.

### **2.4.1 Lithography with Photons, e-beam and Scanning Probes**

The principle of photolithography is to expose certain kind of material, so called photoresist, to electromagnetic radiation ( visible light, UV, DUV, EUV, or X-ray). The exposure of the photoresist to radiation changes the photoresist's solubility in certain kind of solvent. This solvent is called the developing solution. If the photoresist becomes soluble in the developing solution after photon exposure, it is called positive photoresist; if it becomes insoluble after exposure, it is called negative photoresist. In photolithography, exposure is always patterned by interposing a mask between the source of radiation and the material. Photolithography processing yields a replica (perhaps reduced in size) of the pattern of the mask. There are two modes of photolithography: one is projection mode photolithography, where the radiation projects onto the resist with an focusing optical system and the image of the mask is usually reduced by a factor of four; the other one is contact mode photolithography, where the mask is placed in physical contact with the photoresist. Projection-mode photolithography is heavily used in the integrated circuit (IC) industry.

The advantage of photolithography is that it is a quick process and easy to manipulate. But the disadvantage is its resolution, which is limited by the source wavelength. The resolution of photolithography increases as the wavelength of the photon used for exposure decreases. With 193 nm photon from an ArF excimer laser and synthetic fused silica lenses, projection photolithography can repeatedly reach feature sizes as small as  $\sim 150$  nm. It is rather difficult to try wavelengthes smaller than 193 nm photons because of the

lack of transparent materials suitable for lenses at these short wavelengths. Thus, the technical challenge for extending photolithographic methods into the sub-100-nm range is the development of reflection optics or stencil masks. Another way to improve resolution is to play tricks with the chemistry of the photoresist. One example is a nonlinear photoresist. It is based on two-photon absorption. This will significantly increase the resolution.

E-beam lithography has much higher resolution than photolithography because the de Broglie wavelength of an energetic electron is fairly short ( $\sim 0.1$  nm). E-beam lithography can offer at least  $\sim 10$  nm resolution. The disadvantage of e-beam lithography is the slow processing time. It takes hours to write a 4 inch silicon wafer. One commonly used resist for e-beam lithography is PMMA. There also exist positive and negative resist for e-beam lithography. Besides e-beam lithography, people have tried scanning probe lithography (SPL). The principle of SPL is to allow the small ( $\sim 50$  nm) tips to scan close to the sample's surface via scanning tunneling microscopes (STMs), and atomic force microscopes (AFMs). The advantage of SPL is its high resolution; again the disadvantage is its slow writing speed.

### **2.4.2 Soft Imprint**

Because of high cost of lithography method to prepare templates, people have started to seek nonlithography methods for pattern transfer. One of them is the soft imprint method. The soft imprint method is a technique that imprints a UV (or thermally) curable precursor material against a rigid master and then cures it. Optical glue (Norland Optical Adhesive)

is used as a UV curable precursor, and PDMS is used as a thermal curable precursor. Because of its low price, the high-fidelity of pattern transfer, and the ease of processing, the soft imprint scheme has been widely used in industry to manufacture micro- and even nanostructures, for example, holograms and compact disks (CDs). Soft imprint resolution is mainly determined by van der Waals interactions, by wetting of the precursor solution against the mold, by kinetic factors such as filling speed of the capillaries on a master surface, and by the physical properties of the precursor materials (for example, the thermal expansion property). This method is not limited by optical diffraction. It can achieve much higher resolution than the photolithography technique. According to published results, soft imprint methods can be used to achieve a few nanometer resolution [70]. The disadvantage of this method is that you need to create a good original mold.

### 2.4.3 Self-Assembly

Another non-lithographic method is to use self-assembly to spontaneously form a pattern. The concept of self-assembly originates from biological processes such as the folding of polypeptides into functional proteins, the formation of chromatin from DNA double-helix, and the formation of cell membranes from phospholipids. In self-assembly, those subunits are commonly driven by entropy to gather together and to form ordered, higher level structures. One example is diblock polymer poly(phenylquinoline)-block-polystyrene ( $PPQ_mPS_n$ , where  $m$  and  $n$  are the number of repeat units of the respective blocks) in carbon disulfide



( $CS_2$ ) [71]. The diblock polymer will form cylindrical micelle like structure in good solvent for coil. After evaporating the solvent, like convective assembly, those micelle like structures self-assembled into close-packed-hexagonal structure. This ordered structure can be used as template for further process.

## 2.5 Template-directed convective assembly

The motivation for combining template technology with convective assembly is to fabricate truly 3D ordered colloidal crystals. As we have mentioned in §2.3, the structure of crystal prepared by convective assembly is rcp. Strictly speaking, a rcp structure is not a true crystal structure, because of its randomness along one crystallographic direction. However, if we direct the crystal growth with a two-dimensional square grating template [i.e., fcc's (100) planes parallel to the substrate], a fcc colloidal crystal will be achieved without stacking faults. As showed in Fig. 2.5, without a square template, the colloidal crystal's first layer structure is hexagonal. If we denote the first layer's position as A, then we'll find that we'll have two equal possible ways to fill the spheres at second layer, which are denoted as B or C. Consequently a random series of A, B and C along z direction will be produced. Thus, a rcp crystal is formed. However, with a square template, the crystal's first layer structure is a square lattice. If we denote the first layer's position as A, then we have only one possible way to fill the spheres at second layer, which is denoted as B. Consequently, a true (100) oriented, fcc colloidal crystal is achieved.

Our convective assembly procedures largely follow previous work. We immerse clean

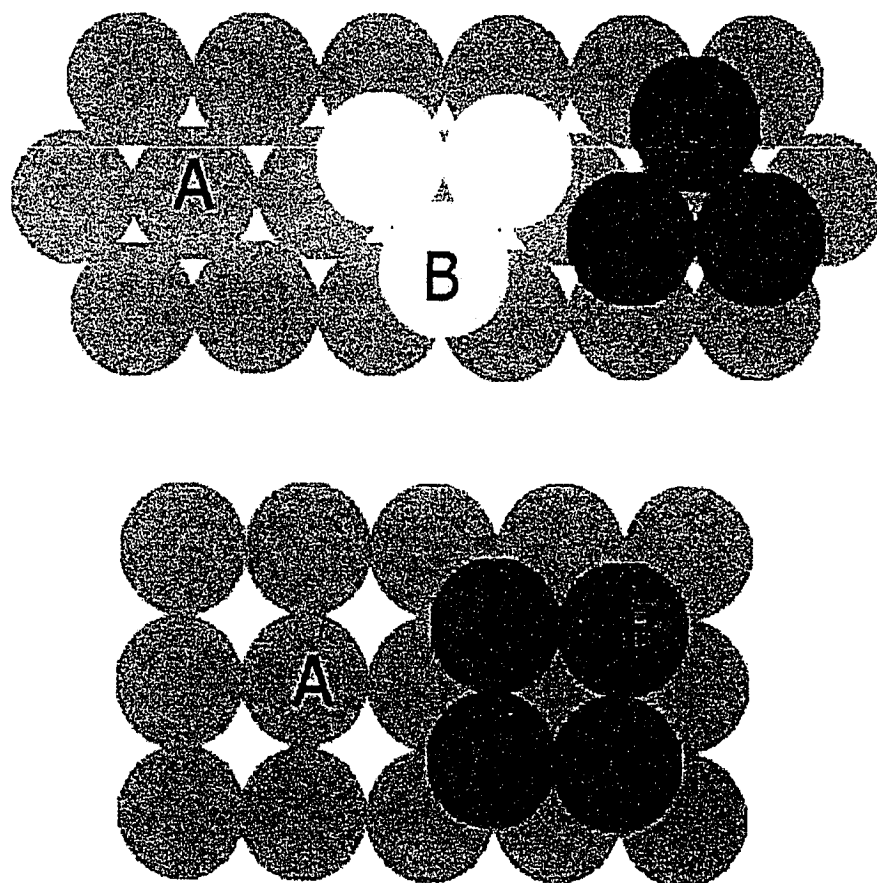


Figure 2.5: Cartoon of how a square template can avoid stacking faults. The upper picture shows that if the first layer's structure is hexagonal, as it always is for a flat substrate, and denote its position as A, then there exist twin positions B and C for the spheres to fill at the second layer. The lower picture shows that there is only one way to fill the second layer if the the first layer is a square lattice.

substrates (with and without templates) vertically in a glass vial containing an aqueous suspension of polystyrene spheres. The particle volume fraction of the suspension is  $\sim 0.01$ . The samples are placed in an oven and the temperature is set at 55 °C. The solvent is slowly evaporated over a period of  $\sim 80$  hours. On the flat substrates we used particles with diameters ranging from 250 nm to 550 nm. Most of the work on the template substrates, however, used  $\sim 500$  nm particles in order to match the template periodicity. The template we used is either a series of parallel lines or a square with period 550 nm. After evaporation, we observe iridescent colloidal crystals on the substrate. Before we tried 3D convective assembly with the template, we tried 2D convective assembly with the template. In 2D convective assembly, we used a low volume concentration ( $10^{-4}$ )  $\sim 500$  nm polystyrene particle suspension. As for the template, we tried both line and square templates whose periodicity is 550 nm. As showed in Fig 2.6, the templates did modulate the convective assembly process: in Fig 2.6(a), the particles spontaneously line up along the line template, and in Fig 2.6(b), the particles form square clusters. Thus, we are convinced that it is possible to use template to direct convect assembly crystallization process. In Fig. 2.7, we show a SEM picture that illustrating the high quality of the final crystal prepared by template driven convective assembly. The colloid structure appears to be fcc without observable stacking faults, instead of rcp by normal convective assembly.

In Fig. 2.9, we show templates fabricated by soft imprint techniques [67]. We use a commercial optical diffraction grating as our starting mold. We obtain a LDPE (low density polyethylene) replica of the original diffraction grating by pressing the diffraction

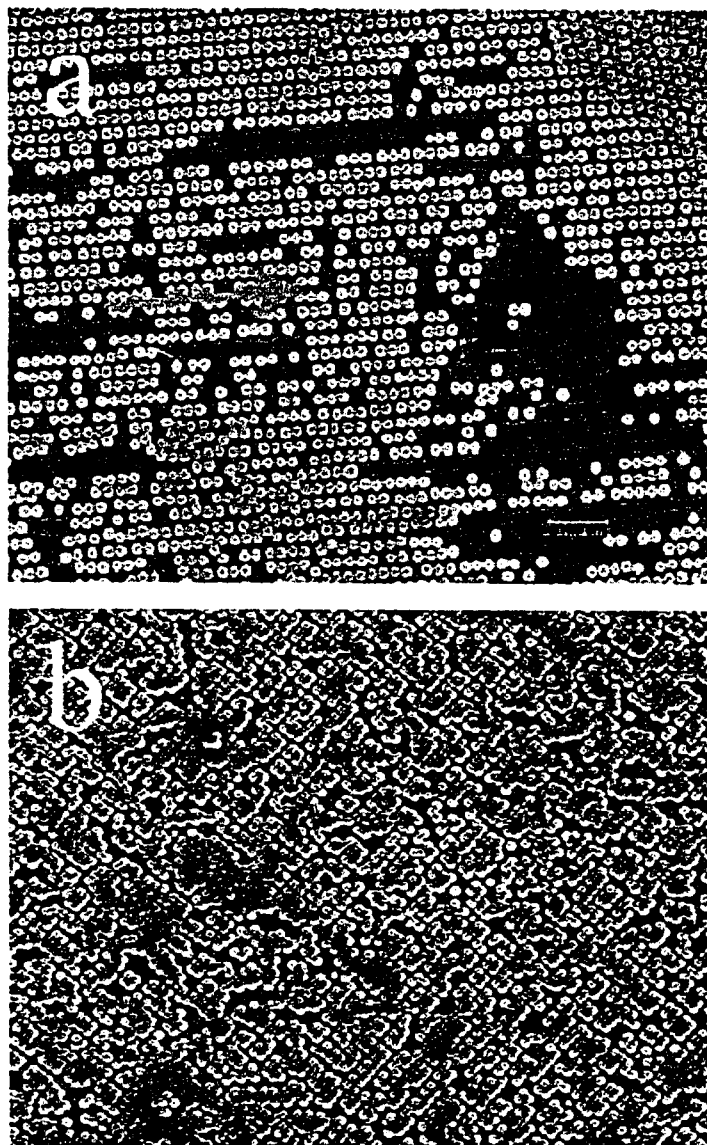


Figure 2.6: SEM pictures of 2D convective assembly with templates. The particle size is  $\sim 500$  nm, and the template periodicity is 550 nm. In a). is line template, and in b). is square template.

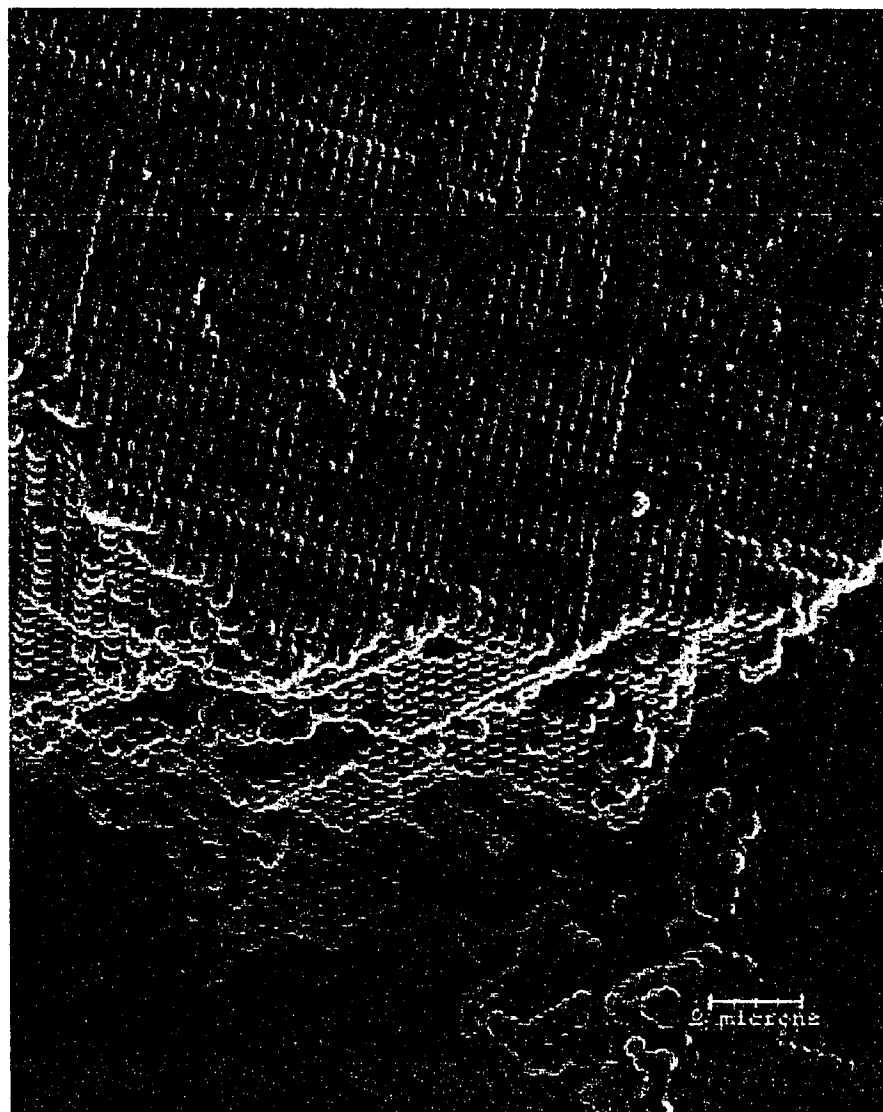


Figure 2.7: SEM picture of 3D colloidal crystal from  $\sim 500$  nm polystyrene beads. It is prepared by convective assembly with square template. The template period is 550 nm. The colloidal crystal's structure is fcc.

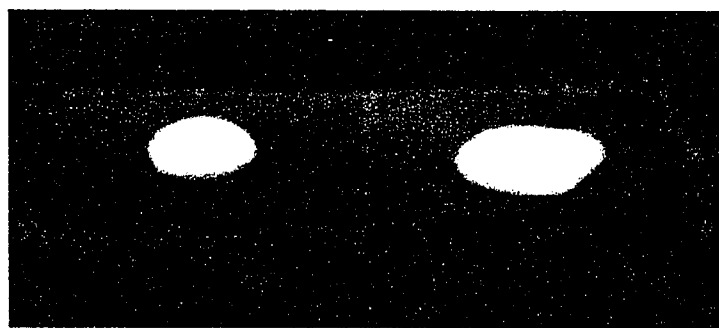


Figure 2.8: Picture of the wetting behavior of a drop of polystyrene beads solution on both glass substrate (left) and on Au/Pd coated substrate (right). The solution's concentration is 0.01 and the bead's size is  $\sim 500$  nm.

grating into a LDPE sheet held at  $90^{\circ}\text{C}$ . Since LDPE's melting temperature is around  $105^{\circ}\text{C}$ , the diffraction grating's structure will be effectively transferred to the LDPE sheet during the mechanical pressing process. In order to make two-dimensional square patterns, we imprinted the grating twice with grooves oriented in orthogonal directions. In our experiment, we make two types of templates, one based on PDMS (poly-dimethylsiloxane) and one based on Norland Optical Adhesive coated with a thin Au/Pd film. In the case of the Norland Optical glue, we place the LDPE grating-replica face down on a glass coverslip, and apply a drop of Norland Optical Adhesive 63 (NOA63) to the glass coverslip. The optical glue droplet is pulled between the coverslip and the LDPE replica by capillary forces. The glue is then cured by UV illumination for one minute. The result is a NOA63 based template that can be peeled away from the LDPE replica. Because the optical glue NOA63 is hydrophobic, we used a Au/Pd sputtering machine to coat the surface of the NOA63 template with a thin layer (10 to 20 nm) of Au/Pd, which significantly improves the surface's wetting behavior. As shown in Fig 2.8, a drop of 0.01 volume

fraction,  $\sim 500$  nm sized polystyrene beads solution has much flatter configuration on a Au/Pd coated substrate than on a pure glass substrate. This indicates that after coating with Au/Pd, the NOA63 substrate becomes more hydrophilic than glass. For the PDMS films, we followed the same procedure. This time we used a drop of PDMS precursor fluid (i.e. Sylgard 184 silicone elastomer/curing agent, which are mixed by 8/1 weight ratio). We cured the PDMS by oven heating ( $55^\circ\text{C}$ ) for  $\sim 36$  hours. The PDMS could then be readily peeled from the replica template. We used plasma oxidization to make the surface more hydrophilic. Since the plasma oxidization process also destroys the template structure, we use the lowest possible oxidization power, and choose oxidization time as 20 seconds. Ultimately we found the Au/Pd coated NOA63 yielded far superior templated crystals, at least in part due to the improved wetting of the aqueous suspension onto its surface. An image of the final Au/Pd/(NOA63 adhesive) template is in Figure 2.10.

Our two-dimensional square template (see Fig. 2.10) introduces geometric barriers for convective assembly at the surface which favor the square lattice over the hexagonal one; our hypothesis was that this ordered two-dimensional structure would bias the system and induce a three-dimensional stacking-fault-free FCC crystal to form via convective assembly. This is what we observed.

In Fig. 2.11(a) we show an SEM picture of a (100)-oriented FCC colloidal crystal achieved with the Au/Pd template. This crystal is about 50 layers thick, and has a domain size of about  $(50\text{ }\mu\text{m})^2$ . Square symmetry has been transferred from the two-dimensional template to the three-dimensional structure as can be readily observed on the top layer

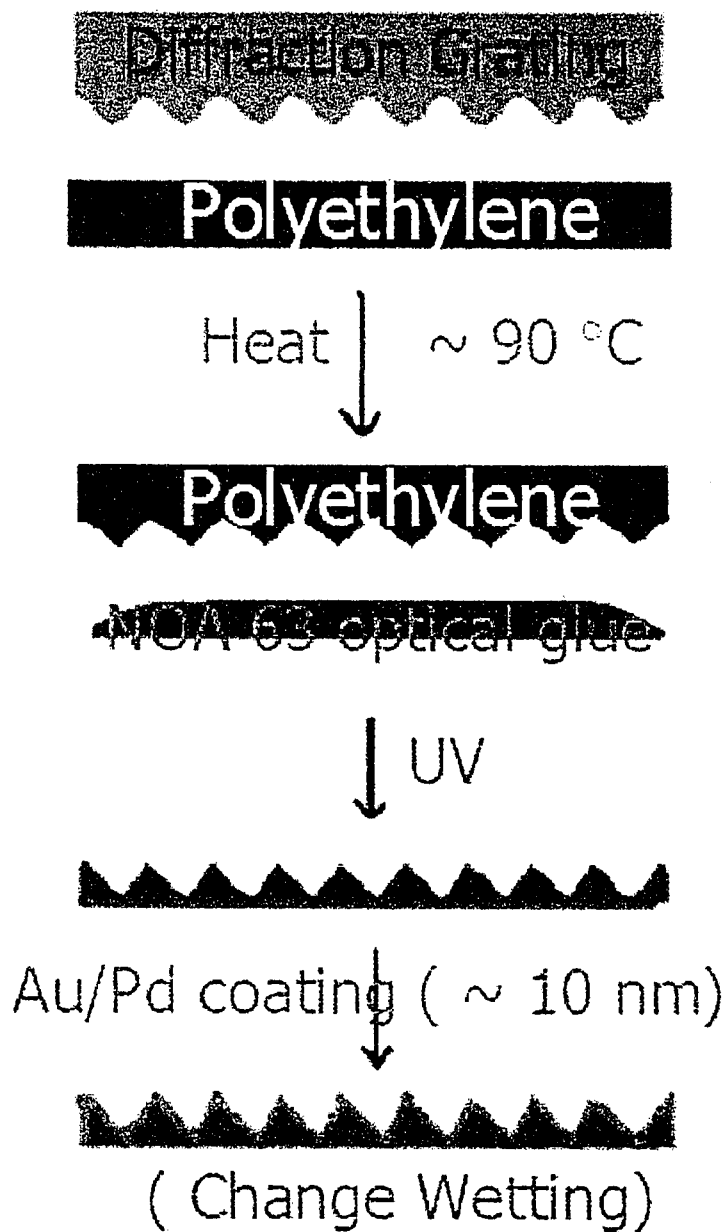


Figure 2.9: Flow chart of how we prepared our template. The basic method used here is imprint technique.



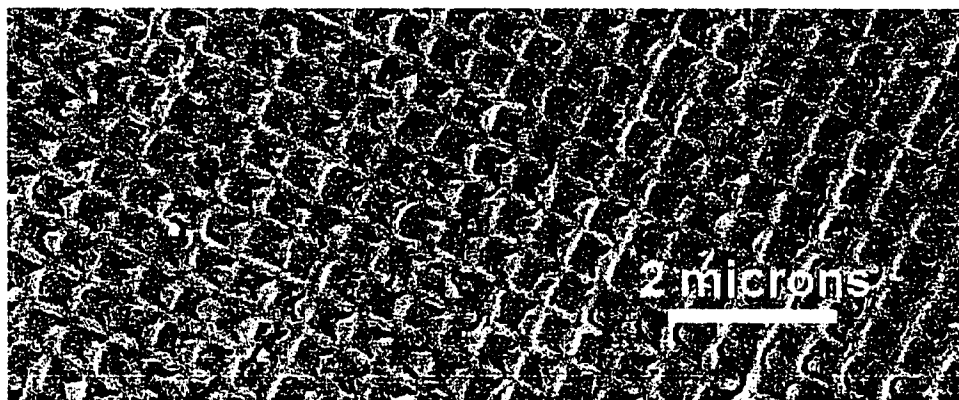


Figure 2.10: SEM picture of a portion of our template. The groove spacing is 550 nm, groove depth is 100 to 200 nm, and lateral dimensions are 6 mm  $\times$  18 mm.

of the crystal. For comparison, in Fig. 2.11(b) we show a control sample grown under exactly the same conditions starting from a flat substrate. Hexagonal symmetry is clearly exhibited; the presence or absence of random stacking faults can not be deduced from these measurements.

The SAXS measurements use beamline 9-ID (CMC-CAT) at the Advanced Photon Source with a selected x-ray energy of 9.0 keV. The beam is collimated using vertical and horizontal mirrors and X-Y slits, and the diffracted signals are measured using a Bruker CCD detector with a 5.2 m camera length. The beam size is approximately  $(200 \mu\text{m})^2$ . Fig. 2.12(a) shows a typical diffraction pattern from  $\sim 500$  nm diameter colloidal spheres convectively deposited on a flat glass substrate. The six-fold symmetry is clearly seen, indicating the diffraction arises from three- or six-fold planes. This observation implies that triangular close-packed sheets of spheres must be parallel to the substrate; such sheets are found in FCC, hexagonal-close-packed, and random-close-packed lattices. Interestingly the same orientation is observed over the entire sample; it is correlated with the growth

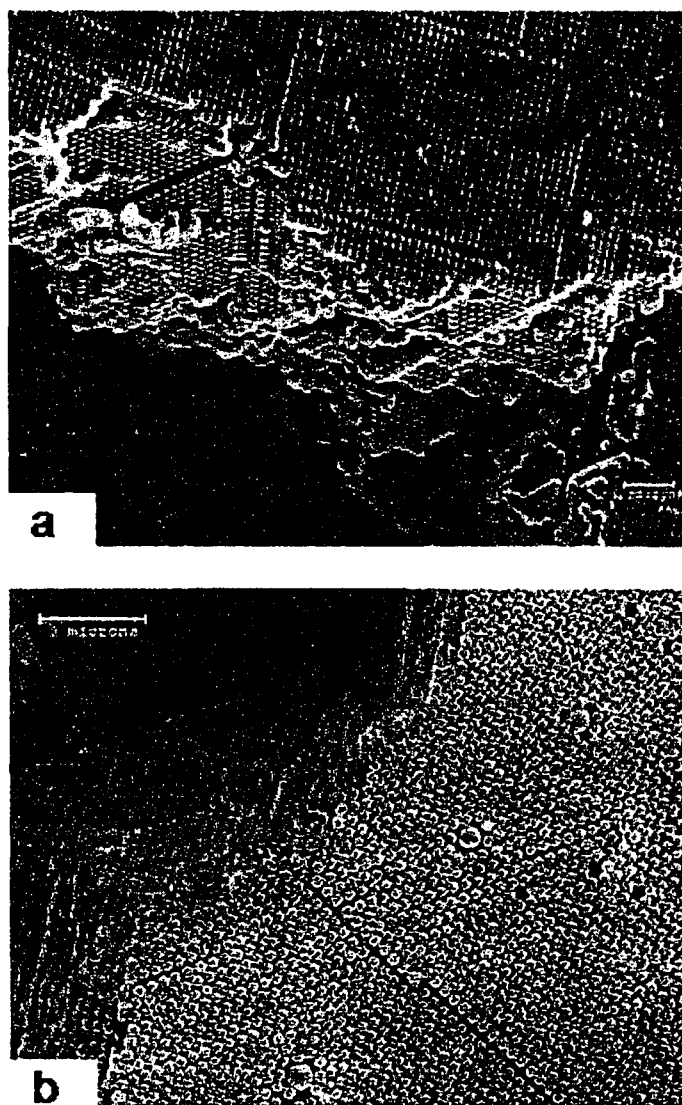


Figure 2.11: SEM pictures of the crystal convective assembled (a) with template and (b) without template. The particle diameter was  $\sim 500$  nm, and the template period was 550 nm.

front. It suggests that the growth process also induces a preferred orientation of the resultant crystal. Because the sample can be rotated tens of degrees relative to the incoming beam with only slight distortion of the pattern, the bright features in the pattern are actually cross-sections of Bragg rods, which in turn indicate a high density of stacking faults. Similar features were seen over a wide range of particle sizes, although in general a higher degree of orientation is observed for smaller particles (250 - 400 nm) than larger particles (450 - 550 nm).

In Fig. 2.12(b) we exhibit the diffraction pattern from 500 nm colloidal spheres convectively assembled on the templated (Au/Pd) glass substrate. Several types of pattern are seen: Bragg rings corresponding to a powder of unoriented domains, six-fold patterns such as in Fig. 2.12(a) (but with poorer orientational order), and four-fold patterns. The four-fold patterns always have some admixture of hexagonal symmetry. The four-fold patterns are indicative of the underlying square structures. The poorly oriented six-fold symmetry and the Bragg ring structure implies that the competition between the template and the natural rcp packing driven by convective assembly process. By scanning the x-ray beam over the surface we find that the diffraction pattern changes when the beam is displaced a distance comparable to its diameter, indicating that typical domain sizes were less than  $(200 \mu m)^2$ . We also estimate that 10-40% of the sample has square symmetry. The rest is disordered or hexagonal. This observation is in agreement with rough estimates from SEM, where we found 30-50% square-symmetric crystals.

In order to improve on the present scheme it is desirable to understand the underlying

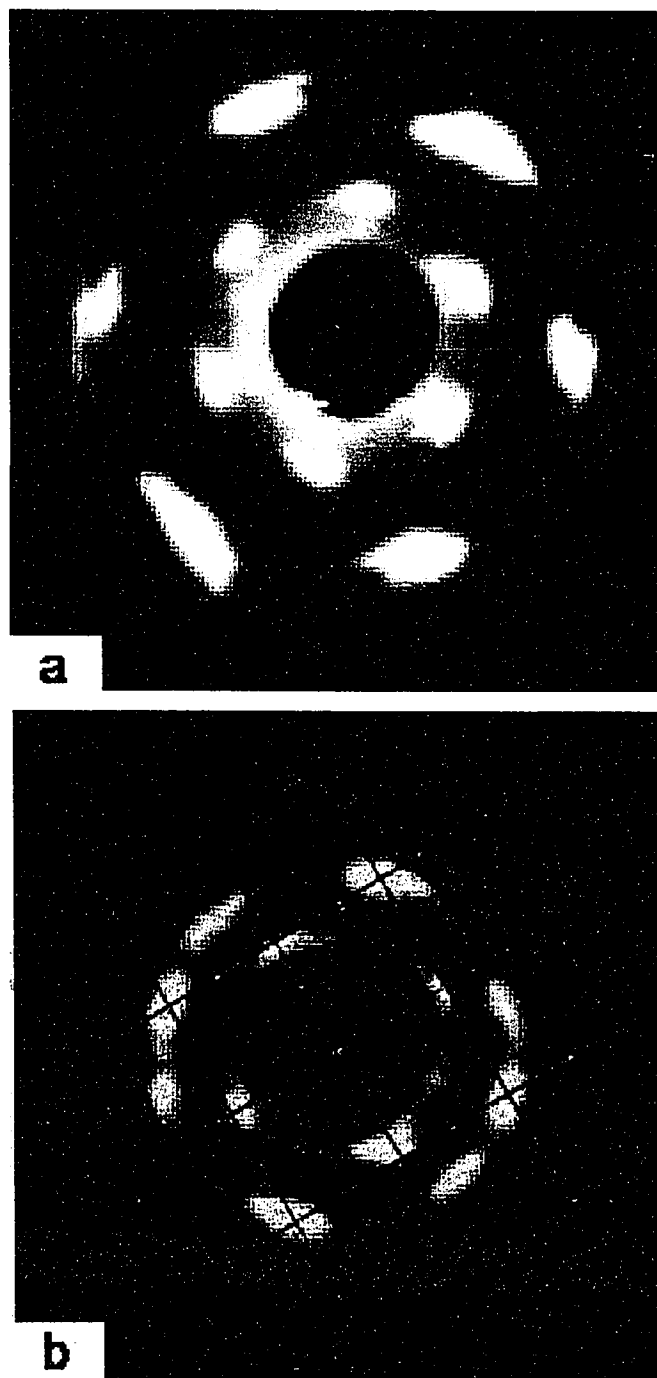


Figure 2.12: Diffraction pattern from convective assembled crystals (a) Hexagonal domains (without template) and (b) Square domains (with template). In Fig (b), the superimposed grid facilitates recognition of the square symmetry.

growth mechanisms. While we cannot offer a full explanation, we have made several observations about this system, providing pieces of information that may be useful for future work.

Growth on Au/Pd-NOA63 templates is superior to growth on NOA63-only and PDMS templates. We believe the most important reason for this effect is that water wets the Au/Pd-NOA63 template extremely well. The PDMS templates show only 5-10% square-symmetric regions, but was still superior to the NOA63 template (which had the worst wetting properties of the three templates). It is also very likely that the yield could be improved with increased groove depth and quality; groove depth is not well controlled, varying from 100 to 200 nm, and growth is better in the deeper regions. Finally, it is important to match particle size to groove spacing. The same experiment with 400 nm particles does not exhibit square-symmetry, and showed no difference for samples with and without the template.

## **2.6 Conclusion and Future Work**

In this chapter we reviewed the history of convective assembly and demonstrated that square two-dimensional grating templates can drive the growth of three-dimensional, face-centered-cubic (fcc) colloidal crystals by convective assembly. The square symmetry [i.e., (100) planes parallel to the substrate] of the underlying template is transferred to the colloidal crystal and maintained throughout its growth of  $\sim 50$  layers. We characterize crystals grown on flat and on templated substrates using electron microscopy and small-angle

X-ray scattering (SAXS). SAXS measurements of the templated samples clearly show fourfold diffraction patterns that arise from fcc domains without stacking faults.

As a continuation of this work, it will be desirable to fabricate new colloidal crystal structures with convective assembly via new templates. People have done extensive work to pursue bcc colloidal crystal for pure research interest, but up to now the bcc structure fails to appear in template directed colloidal crystallization processes. Theoretically, fcc is a more free energetically favorable state than bcc. However, convective assembly via templates is a non-equilibrium process. Thus, it may be possible to achieve bcc colloidal crystal as long as we prepare a deep enough template with right pattern [(100)- or (110)-plane of bcc]. We can also try to synthesize non-close-packing crystals out of convective assembly via template. This might be done through adjusting the size ratio between the particle diameter and the template periodicity. Also, the template need not necessarily be square; it can be rectangular structured instead of square structured, or other periodic structure. This kind of new template may produce new structured colloidal crystals. Furthermore, template can also be used to assemble nonspherical particles.

## **Chapter 3**

# **Direct Visualization of Polymers in Nematic Liquid Crystals: Coil-to-Rod Transition**

### **3.1 Introduction**

Semi-flexible polymers have drawn tremendous attention not only because of their interesting static and dynamic behaviors, but also because of their important role in biophysics. DNA, neurofilaments, and f-actin are all semi-flexible biopolymers; their persistence lengths are much larger than their diameters. Their phase behavior and their mechanical responses are significant for cell biology. Extensive work has been devoted to schemes to elongate semi-flexible polymers, for example with flow stresses [72, 73],

AFM [74], micro-needles [75], optical tweezers [76], magnetic tweezers [77], AC electric fields [78], and capillary forces [79]. Perhaps the most celebrated example comes from researchers trying to understand the static and dynamic extension-versus-force relationship of DNA during stretching. In our research, we have found a new way to elongate semi-flexible polymers. We elongate them by immersion in a nematic liquid crystal solvent. Our experimental system can be viewed as a binary mixture of mesogens of two different lengths. When the length difference between these two mesogens is large, the binary mixture can be viewed as long filament immersed in a continuous nematic solvent. This system poses interesting, challenging and fundamental experimental and theoretical questions.

The problem of a semi-flexible polymer in a nematic liquid crystal is related to the liquid crystal problem itself, a problem with a long and rich history. Theoretically, Onsager did the pioneering work, investigating the hard rod isotropic-nematic (I-N) phase transition with the method of virial expansion [10]. In his theory, he kept only up to second order terms in the virial expansion, which limited the application of his theory to long rods ( $L/D > 100$ ,  $L$  is rod length, and  $D$  is rod diameter). Later, Cotter and coworkers developed a scaled particle theory to include all higher order virial coefficients in an approximate way [15, 16]. Thus, the theory was extended to include hard rods with different size ratios. However, in both theories it was assumed the rods were perfectly rigid objects. In most experimental systems, rods have finite rigidity. Khokhlov and Semenov were



the first to study the effect of rod semi-flexibility on the isotropic-nematic phase transition [80, 81]. With further work from Hentscke, Odijk, and Yang, a theory was developed that could be applied to rods with arbitrary persistence length [82, 83, 84]. Generally, finite rigidity will increase the required fd concentration at the I-N transition, and will decrease the width of I-N coexistence region; in addition the order parameter of the semiflexible polymer solution will be reduced. For example, for fd virus, the order parameter at I-N coexistence is 0.55, instead of 0.79 for perfect hard rods. Theorists have also started to work on binary solutions composed of hard rods of different lengths. Lekkerkerker and coworkers noticed that for a binary mixture of long and short rods, the longer rods have much higher order parameter than the shorter ones. Vroege and Lekkerkerker also found that there exists an isotropic-nematic-nematic phase separation, or a demixing phase transition when the ratio of the lengths of two rods exceeded 3.2 [18]. When the length ratio between the two rods is sufficiently large, i.e. large enough, so that we can approximate the short rods as continuous nematic background, another theoretical approach is required for the binary mixture. Both deGennes and Kamien have studied this last case and have found there exists a coil-rod phase transition for long semiflexible polymers immersed in the background nematic solvent formed by short polymers [19].

The nematic liquid crystalline phase is characterized by long range orientational order in which the anisotropic constituent particles are preferentially aligned along the same direction. This alignment is characterized by the orientational distribution function (ODF) which describes the probability that a rod is aligned along a certain direction. For the

isotropic phase, the ODF is a constant, while in nematic phase, the ODF can be approximated by a Gaussian distribution function. The half-width of the Gaussian distribution describes how much the molecule deviates from the common nematic director direction. The properties of the isotropic and nematic phases of perfectly rigid rods are well described by the density functional theory due to Onsager. The main difficulty for describing the isotropic to nematic phase transition of semi-flexible rods arises because, in addition to the change in the orientational distribution function, there is also a change in the internal shape of the polymer. Theoretical work predicts the polymer will become highly elongated along the director when entering the nematic phase, in other words, the polymer undergoes a coil-rod phase transition. In addition, the existence of hairpin defects wherein the polymer rapidly changes its direction by 180 degree has been predicted [85]. Some theoretical models suggest there exists a demixing phase transition when the length ratio between the long and short hard rods reaches a critical value. If we treat our polymer persistence length as one rod, and the fd-virus as the other rod, then this model might also apply to our experimental situation. To our knowledge, there has not been a theory to describe binary mixtures of short and long semi-flexible polymers.

Up to now the conformations of the liquid crystalline polymers have been experimentally studied using neutron scattering in a mixture of deuterated and non-deuterated polymers [86]. These experiments have provided evidence for chain elongation along the nematic director and the existence of hairpin defects [87]. No work, however, has been done on the conformations of semi-flexible polymers imbedded in a nematic solvent.

In our experiment we study, for the first time, conformations of isolated semi-flexible polymers dissolved in a nematic phase liquid crystal formed by other semi-flexible rods. The imbedded polymers are fluorescently labelled and directly visualized by optical microscopy. The real space images of those polymers enable us to quantitatively measure the dynamic and static properties of the conformations of the polymers dissolved in a nematic phase. This information is difficult to extract from scattering experiments.

In this Chapter, we start with a general discussion about polymer flexibility and configuration, and then we move to a discussion of our experiment on four different semiflexible polymers' configuration in a nematic field. The four different semiflexible polymers are DNA, neurofilaments, wormlike micelles, and actin. The nematic field is generated by the fd virus solution. Finally we describe the theoretical explanations for our experimental observations. In the experiments we observe that neurofilaments, wormlike micelles and actin exhibit a coil-rod phase transition when they are dispersed in a fd solution that undergoes an isotropic-nematic transition. However, for DNA, we observe demixing phase behavior. This may be due, in part, to its small persistence length ( $l_p = 50nm$ ). We also obtained the biopolymers' order parameter by determining their orientational distribution function (ODF). We found the immersed polymer's order parameter is much higher than the background nematic solvent order parameter. Furthermore, we discovered that the longer the polymer filament, the higher average order parameter it has. Besides order parameters, we also measure the elongated filaments' tangent-tangent correlation function

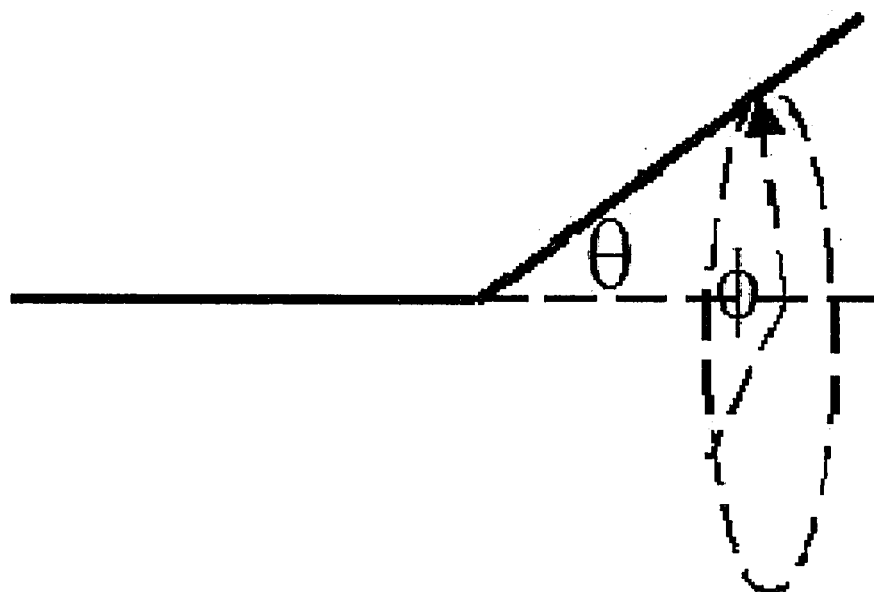


Figure 3.1: Sketch of how the monomers are bound together. Bond angle ( $\theta$ ) and dihedral angle ( $\phi$ ) are as shown in the figure.

(TTCF). From the TTCF, we obtained other system parameters, such as the Odijk deflection length (for the first time), and the elastic constant of the background nematic solvent.

## 3.2 Polymer Flexibility and Configuration

Polymers are giant molecules built by identical monomers. Mostly, those monomers are composed of carbon (C), hydrogen (H) and oxygen (O). These atoms are bound together with covalent bonds. For a covalent bond, there exists a special bond length, bond angle ( $\theta$ ), and dihedral (torsion) angle ( $\phi$ ) as shown in Fig. 3.1. It costs energy for atoms to deviate from their equilibrium positions. For an organic, aliphatic molecule, the energy cost to deviate from the equilibrium bond angle ( $\theta$ ) is far bigger than  $k_B T$  at  $T=300^\circ\text{K}$  (room temperature). Consequently bond angles are very stiff. However, dihedral angles

$(\phi)$  can vary from the primary to the secondary free energy minimum rather easily; the energy difference between these angles is less than  $k_B T$ , and the tunnelling barrier is often not too high. Thus, the flexibility of polymers comes from the torsional degrees of freedom. The persistence length is a physical quantity describing polymer stiffness. In order to quantitatively understand/describe this stiffness, we introduce a scalar variable  $s$ , with  $s = 0$  at one end of the polymer and  $s = Nl_0$  at the other, where  $N$  is the number of monomers and  $l_0$  is the monomer length (and diameter for flexible polymers). Thus,  $s$  represents the distance along the polymer chain. As shown in Fig. 3.2,  $\mathbf{u}(s)$  is defined as the tangent unit vector at position  $s$  along the polymer chain. The tangent-tangent correlation function (TTCF),  $C(\Delta s)$ , is defined as:

$$C(\Delta s) = \langle \mathbf{u}(s) \cdot \mathbf{u}(s + \Delta s) \rangle. \quad (3.1)$$

The persistence length measures the decay of  $C$  and therefore gives a measure of the stiffness of a polymer. It is defined as:

$$l_p = \int_0^\infty C(s') ds'. \quad (3.2)$$

If a polymer's persistence length is of order of the monomer's diameter, it is called a flexible polymer, if a polymer's persistence length is much bigger than the monomer's diameter, it is called a semiflexible polymer.

For a flexible polymer, the bond angle  $\theta$  is fixed, but the dihedral angle is completely

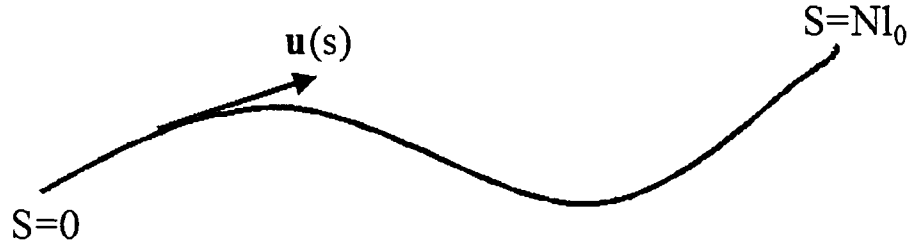


Figure 3.2: The scheme of a polymer; the conformation of the polymer is parameterized by  $s$ .

free. According to this freely rotating chain model, the polymer's end-to-end distance  $\mathbf{R}$  can be expressed as:

$$\langle \mathbf{R}^2 \rangle = Nb_0^2 \frac{1 + \cos \theta}{1 - \cos \theta}. \quad (3.3)$$

For a semiflexible polymer with constant contour length, we define  $\mathbf{R}(s)$  to be the position of a point on the chain at the contour length  $s$ . The vector  $\mathbf{u}(s) = \frac{\partial \mathbf{R}}{\partial s}$  is the unit vector tangent to the chain. The bending energy of the polymer can be expressed as:

$$U_{bend} = \frac{1}{2} E \int_0^L ds \left( \frac{\partial \mathbf{u}}{\partial s} \right)^2 \quad (3.4)$$

where  $E$  is the bending constant. The conformational distribution of the polymer is given by the Boltzmann distribution:

$$\Psi[\mathbf{u}] \propto \exp\left(-\frac{U_{bend}}{k_B T}\right) = \exp\left[-\frac{l_p}{2} \int_0^L ds \left( \frac{\partial \mathbf{u}}{\partial s} \right)^2\right]. \quad (3.5)$$

where  $l_p = \frac{E}{k_B T}$ . From Equation 3.5, for small  $s$  we obtain:

$$\langle (\mathbf{u}(s) - \mathbf{u}(0))^2 \rangle = \frac{2s}{l_p}. \quad (3.6)$$

From Equation 3.6, we obtain the tangent-tangent correlation function (3D):

$$\langle \mathbf{u}(s) \cdot \mathbf{u}(0) \rangle = \exp\left(-\frac{s}{l_p}\right). \quad (3.7)$$

For 2D situation, the tangent-tangent correlation function is:

$$\langle \mathbf{u}(s) \cdot \mathbf{u}(0) \rangle = \exp\left(-\frac{s}{2l_p}\right). \quad (3.8)$$

Thus, for an isotropic semiflexible polymer, we can obtain its persistence length by measuring its TTCF. What's more, from TTCF we can calculate the mean end-to-end distance:

$$\begin{aligned} \bar{R}^2 &\equiv \langle (\mathbf{R}(L) - \mathbf{R}(0))^2 \rangle = \int_0^L ds \int_0^L ds' \langle \mathbf{u}(s) \cdot \mathbf{u}(s') \rangle \\ &= 2 \int_0^L ds \int_0^L ds' \exp\left(-\frac{s-s'}{l_p}\right) = 2Ll_p - 2l_p^2[1 - \exp\left(-\frac{L}{l_p}\right)]. \end{aligned} \quad (3.9)$$

Equation 3.9 is valid for the three-dimensional case. For the two-dimensional case, the

expression for square end-to-end distance is:

$$\bar{R}^2 = Ll_p - \frac{l_p^2}{2} [1 - \exp(-\frac{2L}{l_p})]. \quad (3.10)$$

From Equation 3.10, it can be proved that a polymer's end-to-end distance decreases with decreasing polymer persistence length. When  $l_p$  goes to the monomer size, the polymer behaves like a random coil, and the end-to-end distance is proportional to  $N^{0.5}$ , where  $N$  is the number of monomers the polymer has. For  $l_p$  much larger than the polymer's contour length  $L$ , the polymer behaves like a hard rod, with end to end distance equal to  $L$ . When  $l_p$  is at the same order of  $L$ , the polymer behaves like a bending coil.

### 3.3 Experiment

#### 3.3.1 fd Virus and Its Phase Behavior

In our experiment, we use the fd virus solution as our background nematic field “generator”. Bacteriophage fd is a rod-like molecule. Its contour length ( $L_c$ ) is 880 nm, diameter ( $D$ ) is 6.6 nm, and persistence length ( $L_p$ ) has been measured to range between 1  $\mu\text{m}$  and 2.2  $\mu\text{m}$  [98]. Fd virus is a semi-flexible polymer, since  $L_p/D \cong 300$ . Because of its anisotropic shape ( $L_c/D=135$ ), fd virus suspensions exhibit isotropic, nematic and smectic phases as a function of fd concentration. In the isotropic phase, the rods orient randomly; in the nematic phase, the rods align along approximately the same direction, but the positions of their centers-of-mass are disordered; in the smectic phase, the rods have both long



range orientational order and long range one-dimensional positional order.

Fd virus is a highly charged macromolecule. Its charge density is  $1\text{ e}/\text{\AA}$ . But at a high suspension salt concentration ( $\sim 200\text{ mM}$  of the buffer), the surface charge is effectively screened. The resultant charged rod can be viewed as a hard rod with larger effective diameter. Since the hard-core excluded-volume effect is temperature-independent, the fd concentration is the only parameter determining the suspension phase behavior.

The phase diagram for fd suspensions is shown in Fig. 3.3. In the figure, the filled circles are experimental data for the nematic phase, and the open circles are experimental data for the isotropic phase. The upper curve is a theoretical prediction for the nematic phase, and the lower curve is a theoretical prediction for the isotropic phase. The region between these two curves corresponds to the I-N coexistence regime.

In our experiment we dissolved fluorescently labelled semi-flexible polymers at very low volume-fraction into the fd suspensions. The polymers are  $\lambda$ -DNA, neurofilaments, wormlike micelles (assembled from diblock copolymer), and self-assembled f-actin. The DNA, neurofilaments and actin were negatively charged and therefore also charge stabilized in the suspension of negatively charged fd virus. The wormlike micelles were sterically stabilized with a PEO layer which also does not stick to fd virus.

### 3.3.2 Preparation of Biopolymers

**fd virus:** The fd virus was prepared by standard biological protocols [88]. We used the JM101 strain of *E. coli* as our host bacteria. The standard yield is around 50 mg of fd per

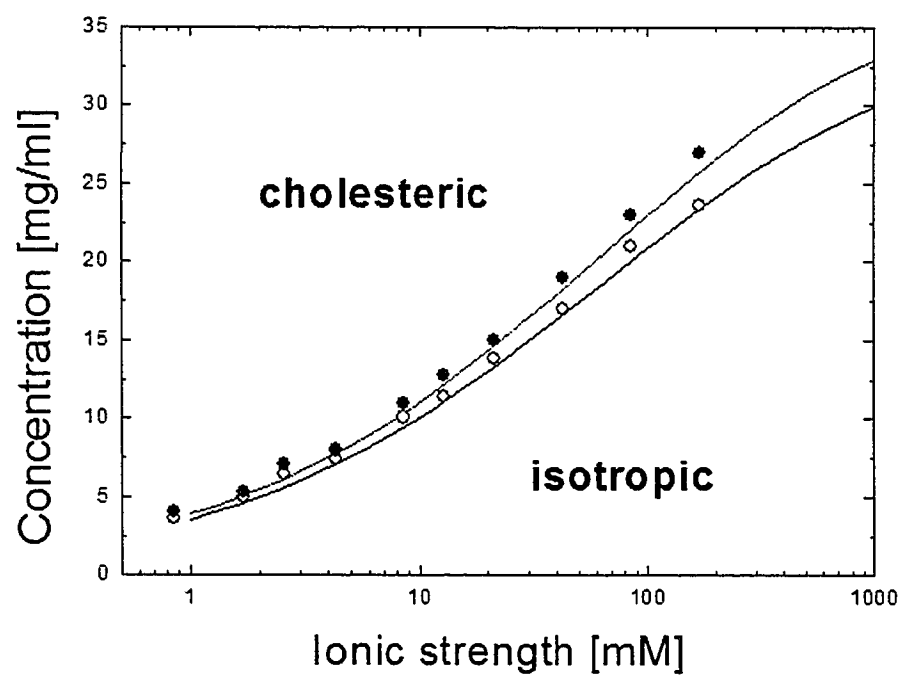


Figure 3.3: Phase diagram of fd solution. The filled circle points are experimental data for nematic phase, the open circle points are experimental data for isotropic phase. The upper curve is theoretical curve for nematic phase, and the lower curve is theoretical curve for isotropic phase. The region between these two curves are isotropic-nematic coexistence region. (From ref. [109].)

liter of infected bacteria, and the virus is typically grown in 10-12 liter batches. The virus was extensively dialyzed against a 20 mM Tris-HCl buffer at pH 8.2. In our experiment, bacteriophage fd was suspended in a phosphate buffer (150 mM KCl, 20 mM phosphate, pH=7.0).

$\lambda$  – DNA:  $\lambda$ -DNA was ordered from New England Biolabs with original concentration at 500  $\mu\text{g/ml}$ .  $\lambda$ -DNA's contour length  $L_c$  is 16  $\mu\text{m}$ , diameter is 2 nm, and persistence length  $L_p$  is 0.05  $\mu\text{m}$  [91].  $\lambda$ -DNA was fluorescently labelled by YOYO-1 (Molecular Probes, Eugene OR) at a ratio of 5 base-pair DNA to 1 molecule of YOYO-1.

**Neurofilaments:** Neurofilaments were purified from bovine spinal cord according to Leterrier et al [89]. Their  $L_c$  is from 2 to 10  $\mu\text{m}$ , diameter is 20 nm, and  $L_p$  is  $\sim 0.2 \mu\text{m}$  [92]. Neurofilaments were fluorescently labelled by incubating with succinimidyl rhodamine B at 24 °C at a molar ratio 1:1000 as described by Lettreier et al.

**Wormlike micelles:** Wormlike micelles were assembled from diblock copolymers (polyethyleneoxide-polybutadiene PEO-PBD, MW 4900). The copolymer's hydrophobic part (polybutadiene) formed the core of the wormlike micelle, and hydrophilic part (polyethyleneoxide) formed the outlayer of wormlike micelle. Those diblock copolymers were synthesized by a two-step anionic polymerization procedure [90]. Their  $L_c$  ranges from 5 to 50  $\mu\text{m}$ , diameter is 14 nm, and  $L_p$  is  $\sim 0.5 \mu\text{m}$  [93]). Wormlike micelles were fluorescently labelled by dissolving PKH26 dye (Sigma, St. Louis MO) which preferentially partitions into the hydrophobic cores of the micelles. The dye PKH26 was added to wormlike micelle at a ratio at 1:1000 by weight.

Table 3.1: Contour length  $L_c$ , persistence length  $l_p$  and diameter  $D$  of the different polymers used in our experiments.

polymer	$L_c$ [ $\mu$ m]	$l_p$ [ $\mu$ m]	$D$ [nm]	Ref
$\lambda - DNA$	16	0.05	2	[91]
neurofilaments	2-10	0.2	20	[92]
wormlike micelles	5-50	0.5	12	[93]
f-actin	2-20	16	7	[95]
fd virus	0.9	2.2	7	[98]

**Self – Assembled f – actin:** Monomeric Actin (G-actin) was purified from rabbit muscle by the method of Spudich and Watt [94]. G-actin was rapidly frozen in liquid  $N_2$  and stored at  $-80^\circ\text{C}$ . On the day of use aliquouts of actin were quickly thawed at room temperature. Actin was polymerized for 12 h at  $5^\circ\text{C}$  in buffer (300 mM KCl, 2 mM  $MgCl_2$ , 10 mM phosphate, 0.2 mM  $CaCl_2$ , 0.5 mM ATP and pH=7.0). The self-assembled f-actin was stored at  $5^\circ\text{C}$  [94]. Its  $L_c$  is from 2 to 20  $\mu\text{m}$ , diameter is 7 nm, and  $L_p$  is 16  $\mu\text{m}$  [95]. We fluorescently labelled f-actin with rhodamine-phalloidin (Sigma, St. Louis, MO) at a molar ratio 1:1.

### 3.3.3 Sample Preparation

The physical properties of the four semiflexible polymers and fd virus are shown in Table 3.1. We prepared our samples by mixing dilute, fluorescently labelled, polymer solutions into the fd solutions. Because of the high viscosity of the nematic fd solution, we carefully mixed the sample solution to ensure uniform distribution of fd concentration over the

entire sample. When handling the biopolymers during the mixing process, we cut the head of the micropipet tip in order to prevent breakage of biopolymers. We also put the sample solution under cross polarizers to ensure that the sample was nematic.

We prepared our samples in two ways. In order to achieve a 2D sample chamber, we injected  $\sim 5 \mu\text{L}$  sample solution between a glass cover slip and a glass slide without spacers, and then we sealed the container. The sample thickness in this case was around  $10 \mu\text{m}$ . Unfortunately there always exists flow when the sample is prepared in this way. The flow has a noticeable effect on the polymer's TTCF. Thus to obtain TTCF, we made 3D samples. We added stretched parafilm as a spacer between the coverslip and the glass slide; the sample chamber's thickness was around  $50 \mu\text{m}$  in this case. Because the wall will also affect the polymer's configuration, we collected all images  $5 \mu\text{m}$  away from the walls. In order to eliminate the sticking behavior of the polymers to the glass coverslip, we treated the glass coverslip by sonicating with soap solution, cleaning with ethanol solution, and then immersing in 1 % agarose solution. To prevent photobleaching, we added an anti-bleaching solution (360 U/ml catalase, 2 mg/ml glucose, 8 U/ml glucose oxidase, and 0.5 vol% mercaptoethanol) to the sample.

### **3.3.4 Fluorescent Optical Microscopy**

Fluorescent optical microscopy is an excellent method for studying materials which can be made to fluoresce, either in their natural form (primary or autofluorescence) or when treated with chemicals capable of fluorescing (secondary fluorescence). The phenomenon

of fluorescence describes light emission during the absorption of the excitation light by a chromophore or other conjugated molecule, which is capable of emitting secondary fluorescence. During absorption, the chromophore or other conjugated molecule's electron is excited from ground state to excited state. Because of the vibration loss at the excited state, the emission light's wavelength is longer than the absorption wavelength. By means of appropriate selection of excitation filter, dichromatic beamsplitter (in reflected light fluorescence), and barrier filter, we can achieve maximum emission from the fluorescent samples and also well be able to separate the absorption and the emission signal. Many samples, especially biological and medical ones, are hardly visible with conventional optical microscope. Fluorescent optical microscopy becomes a powerful tool to visualize those samples since many biological and medical samples can be fluorescently labelled. That is why fluorescent optical microscopy is a rapidly expanding microscopy technique employed today, both in the medical and biological sciences. Our actin samples are fluorescently labelled by rhodamine-phalloidin. Rhodamine-phalloidin's absorption and emission curves are shown in Fig. 3.4. The absorption wavelength is 542 nm and the emission wavelength is 565 nm [110].

In our experiment, all samples were imaged with an inverted fluorescence optical microscope (Leica IRBE) equipped with a 100x oil-immersion objective and a 100 W mercury illumination lamp. The microscope was controlled with software Openlab. With programming under Openlab, we can set the sample's exposure time and delay time. The stronger the fluorescence, the shorter the exposure time needed. Usually, we choose an

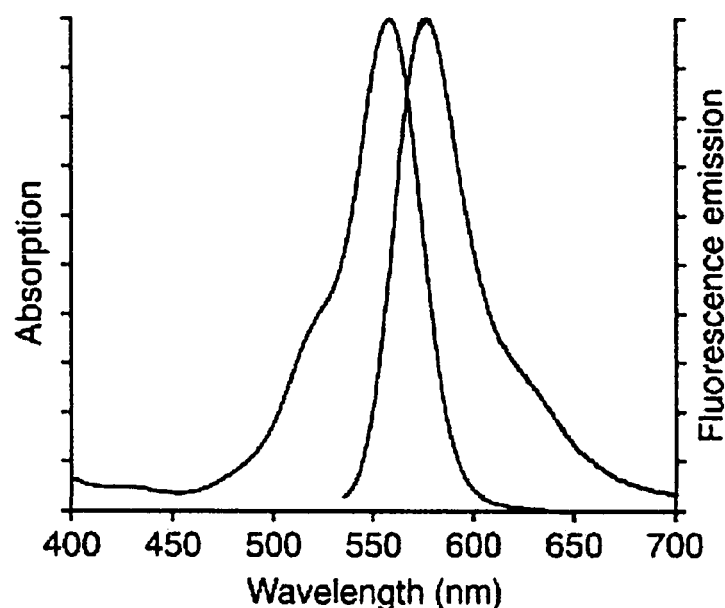


Figure 3.4: The absorption and emission curves of rhodamine-phalloidin. The absorption wavelength is 542 nm and the emission wavelength is 565 nm [110].

exposure time around 250 ms and delay time 200 ms. Thus, the time difference between each image was around one-half second. Images were collected with a cooled CCD camera (CoolSnap HQ, Roper Scientific). The dynamic range of the camera was 12 bytes.

### 3.3.5 Image Analysis

We record the elongated actin filament's image with fluorescent optical microscopy. After we obtain the optical image, we Gaussian fit the intensity profile perpendicular to its elongation direction. As shown in Fig. 3.5(b), this Gaussian fitting can achieve sub-pix accuracy. As shown in Fig. 3.5(c), the fitting result overlaps with real filament quite well. From the fitting result shown in Fig. 3.5(d), the filament is a smooth curve with long wavelength fluctuation. The amplitude of the long wavelength fluctuation is  $\sim 0.5 \mu\text{m}$ .

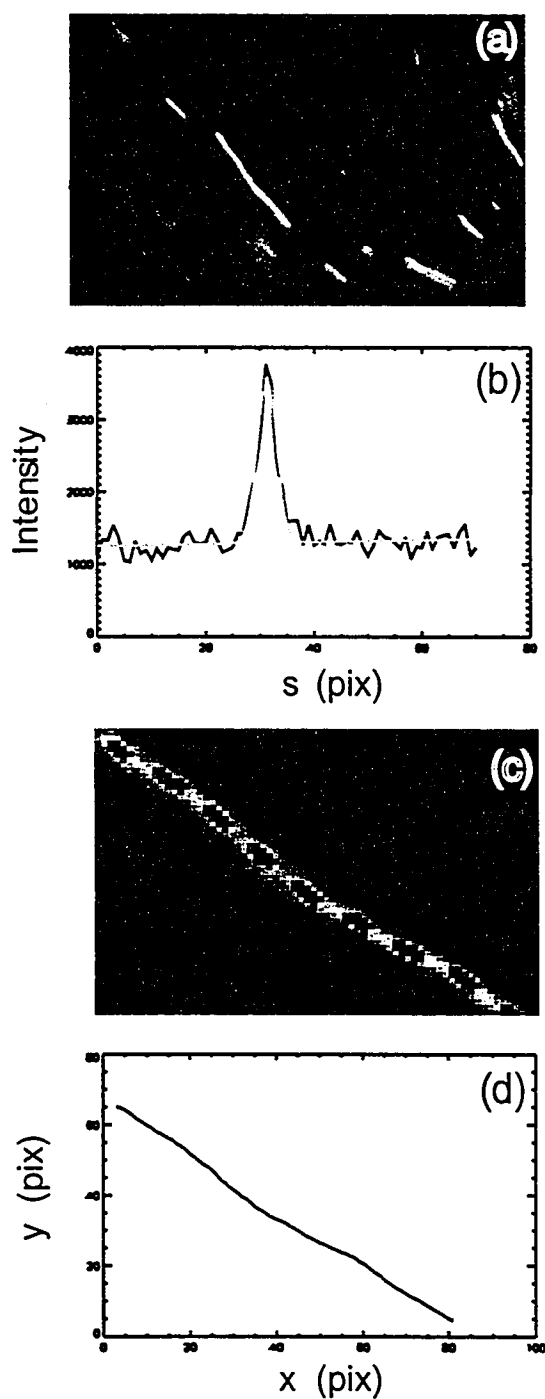


Figure 3.5: Figure (a) is a image of elongated actin filament. Figure (b) is a plot of the Gaussian fit of the intensity profile. The dark line is the intensity profile and the light line is the Gaussian fitting result. Figure (c) exhibits the fitting result over the real actin filament. Figure (d) is the fitting result.



The smoothness of the curve may be due to the fact that the filament's short wavelength fluctuation is so quick that we only observe the averaged signal.

In the nematic solvent, the actin filament fluctuates perpendicular to the elongation direction and diffuses along the elongation direction. The periods of the fluctuation and the diffusion are on the order of couple of seconds. For this time scale, it should not take too long for the actin filament to be in an equilibrium state. We compared different locations' actin filaments' tangent-tangent correlation function and found they were similar to each other. We believed that this was an indication of those filaments were in an equilibrium state.

## **3.4 Theoretical Models**

### **3.4.1 Demixing Phase Behavior and Order Behavior of Binary Rod Solutions**

In our experiment, we found that some biopolymers (neurofilaments, wormlike micelles, and actin) mixed with the background nematic solvent, while other biopolymers (DNA) demixed with the background nematic solvent. Lekkerkerker and coworkers developed a theory that may be relevant to our observations. They did research on the phase behavior of binary mixtures composed of different length hard rods. They extended Onsager's virial expansion theory to the binary solution, using a Gaussian profile for the trial ODF function. The theoretical expression for the free energy of a solution of  $N_1$  rods with length

$L_1$  and  $N_2$  rods with length  $L_2$  (both with the same diameter  $D$ ) in binary equilibrium with the solvent at temperature  $T$  was given by:

$$\begin{aligned}\frac{\Delta F}{Nk_B T} &= \frac{F(\text{solution}) - F(\text{solvent})}{Nk_B T} \\ &= \text{constant} + \ln \rho + (1-x) \ln(1-x) + x \ln x + (1-x)\sigma_1 \\ &\quad + x\sigma_2 + \rho\{(1-x)^2\xi_{11} + 2x(1-x)q\xi_{12} + x^2q^2\xi_{22}\}.\end{aligned}\quad (3.11)$$

Here  $N = N_1 + N_2$  is the total number of rod particles,  $x$  is the mole fraction of rod 2,  $\rho$  is the dimensionless number density  $\rho = \frac{\pi}{4}L_1^2 D \frac{N}{V}$ ,  $q = \frac{L_2}{L_1}$ , and  $\sigma_j$  and  $\xi_{jk}$  are abbreviations for the following functionals with single particle orientation distribution functions  $f_1(\Omega)$  and  $f_2(\Omega)$ .

$$\sigma_j = \int f_j(\Omega) \ln[4\pi f_j(\Omega)] d\Omega, \quad j = 1, 2 \quad (3.12)$$

and

$$\xi_{jk} = \frac{4}{\pi} \int \int \sin \gamma(\Omega, \Omega') f_j(\Omega) f_k(\Omega') d\Omega d\Omega', \quad j, k = 1, 2. \quad (3.13)$$

Gaussian functions were used as trial functions for the ODF:

$$\begin{aligned}f_j(\theta) &\equiv \frac{\alpha_j}{4\pi} \exp\left(-\frac{1}{2}\alpha_j\theta^2\right), & 0 \leq \theta \leq \pi/2 \\ &\equiv \frac{\alpha_j}{4\pi} \exp\left(-\frac{1}{2}\alpha_j(\pi - \theta)^2\right), & \pi/2 \leq \theta \leq \pi.\end{aligned}\quad (3.14)$$

This approach gave good results for the highly ordered nematic phase.  $\alpha_j$  is the variation parameter of this trial function. Plugging the Gaussian distribution function into the

expressions for  $\sigma_j$  and  $\xi_{jk}$ , we obtain:

$$\sigma_j \sim \ln \alpha_j - 1, \quad (3.15)$$

and

$$\xi_{jk} \sim \frac{4(\alpha_j + \alpha_k)^{1/2}}{(2\pi)^{1/2} \alpha_j^{1/2} \alpha_k^{1/2}}. \quad (3.16)$$

which are the first terms of asymptotic expansions valid for large  $\alpha_j$ . Now we minimize the free energy with respect to  $\alpha_j$ :

$$1/2\pi^{1/2}\rho^{-1}\alpha_1^{1/2} = (1-x) + 2^{1/2}xqh(Q), \quad (3.17)$$

and

$$1/2\pi^{1/2}\rho^{-1}\alpha_2^{1/2} = 2^{1/2}(1-x)qg(Q) + xq^2. \quad (3.18)$$

where

$$Q \equiv \frac{\alpha_2}{\alpha_1}, \quad (3.19)$$

$$h(Q) \equiv \left(\frac{Q}{Q+1}\right)^{1/2}, \quad (3.20)$$

$$g(Q) \equiv (1+Q)^{-1/2}. \quad (3.21)$$

Dividing Equation 3.18 by Equation 3.17, we obtain:

$$Q^{1/2} = \frac{q[xq + 2^{1/2}g(Q)(1-x)]}{[2^{1/2}h(Q)xq + (1-x)]}. \quad (3.22)$$

Further mathematical analysis showed that for  $q > 1$ ,  $Q > 1/2(8q^2 + 1)^{1/2} - 1/2 > 1$ .

In our experiment, the actin filaments are  $\sim 10 \mu\text{m}$  long, and the fd is  $\sim 1 \mu\text{m}$  long. So  $q \sim 10$  and  $Q \sim 14$ . As a result, when fd's order parameter is 0.70 ( $\alpha=0.5$ ), the actin's order parameter is 0.998 ( $\alpha=0.036$ ). This qualitatively agrees with our experiment observation that the longer rods always have higher order parameter than the shorter rods. But further experimental data indicates that when fd's order parameter is 0.7, the actin's order parameter is  $\sim 0.93$ , much lower than 0.998 predicted by the theory. The discrepancy is probably due to the fact that both actin filaments and fd are not rigid rods. One easy way to understand the longer rods have larger order parameters is to assume the long rods are composed of the short rods. Because of the internal rigidity, the long rods' orientations are the average of the short ones' orientations. Thus, long rods have better alignment than short rods.

In order to study the possible coexistence between two nematic phases, or the demixing phase transition, they obtained the expression for osmotic pressure and chemical potential of both types of rods in isotropic and two nematic phases. For the isotropic phase (all parameter denoted by subscripts i):

$$\Pi_i \equiv -\frac{b}{k_B T} \left( \frac{\partial F}{\partial V} \right)_{N_1, N_2, T} = \rho_i + \rho_i^2 [(1 - x_i)^2 + 2x_i(1 - x_i)q + x_i^2 q^2], \quad (3.23)$$

$$\mu_{1i} \equiv \frac{1}{k_B T} \left( \frac{\partial F}{\partial N_1} \right)_{N_2, V, T} = \ln \rho_i + \ln(1 - x_i) + 2\rho_i [(1 - x_i) + x_i q], \quad (3.24)$$

$$\mu_{2i} \equiv \frac{1}{k_B T} \left( \frac{\partial F}{\partial N_2} \right)_{N_1, V, T} = \ln \rho_i + \ln x_i + 2\rho_i [(1 - x_i)q + x_i q^2]. \quad (3.25)$$

For nematic phases, we have:

$$\Pi_a \sim 3\rho_a, \quad (3.26)$$

$$\mu_{1a} \sim 3 \ln \rho_a + \ln \frac{4}{\pi} + 3 + \chi'(x_a), \quad (3.27)$$

$$\mu_{2a} \sim 3 \ln \rho_a + \ln \frac{4}{\pi} + 3 + \chi''(x_a), \quad (3.28)$$

where

$$\chi'(x_a) \equiv \ln(1 - x_a) + 2 \ln(1 - x_a + 2^{1/2} x_a q h) - \frac{2^{3/2}(Q - 1)x_a g}{[2^{1/2}(1 - x_a)g + x_a q]}, \quad (3.29)$$

$$\chi''(x_a) \equiv 2 \ln\{q[2^{1/2}(1 - x_a)g + x_a q]\} + \frac{2^{3/2}(Q - 1)(1 - x_a)g}{[2^{1/2}(1 - x_a)g + x_a q]}. \quad (3.30)$$

For possible isotropic-nematic-nematic phase separation, the three coexisting phases reach osmotic pressure and chemical potential equilibrium. The equality of osmotic pressure leads to the equality of the number density of rods in two nematic phase respectively ( $\rho_{aI} = \rho_{aII}$ ). From chemical potential equilibrium, we obtain:

$$\chi'(x_{aI}) = \chi'(x_{aII}), \quad (3.31)$$

and

$$\chi''(x_{aI}) = \chi''(x_{aII}). \quad (3.32)$$

Thus if we can find  $(x_{aI}, x_{aII})$  fulfill Equation 3.31 and Equation 3.32, then there exists a

I-N-N phase separation, or a demixing phase behavior; otherwise, there only exists I-N co-existence. Further mathematical analysis shows that for  $q \equiv \frac{L_2}{L_1} > 3.2$ , there exist possible solutions for  $(x_{aI}, x_{aII})$ . Thus 3.2 is the critical value for the onset of possible demixing phase behavior. Although the binary mixture's components are both semi-flexible polymers in our experiment, this theory still can be used to qualitatively understand the phase behavior of our system. If we want to quantitatively analyze our experiment result, however, we must include the polymers' flexibility in the theory.

In summary, Lekkerkerker and coworkers developed a theory to describe the phase behaviors of binary mixture of different lengths hard rods. As shown in Fig. 3.6, this theory qualitatively explains why in a binary solution of long rods have higher order parameter than short rods; it also qualitatively explains why only DNA demixed with background nematic solvent.

### 3.4.2 Tangent-Tangent Correlation Function

There is no existing theory to describe a polymer's tangent-tangent correlation function (TTCF) when it is immersed in nematic solvent. Accordingly Lau and Lubensky developed a theory aiming to understand a polymer's TTCF in a nematic solvent. In our experiment, the system is composed of a semiflexible polymer and a nematic solvent. We define the general nematic field's director direction as z direction. We also define  $\vec{t}$  as the polymer's local tangent direction, and  $\delta\vec{n}$  as the local nematic director. Subsequently the total free energy is composed of three terms. One is bending energy of the semi-flexible

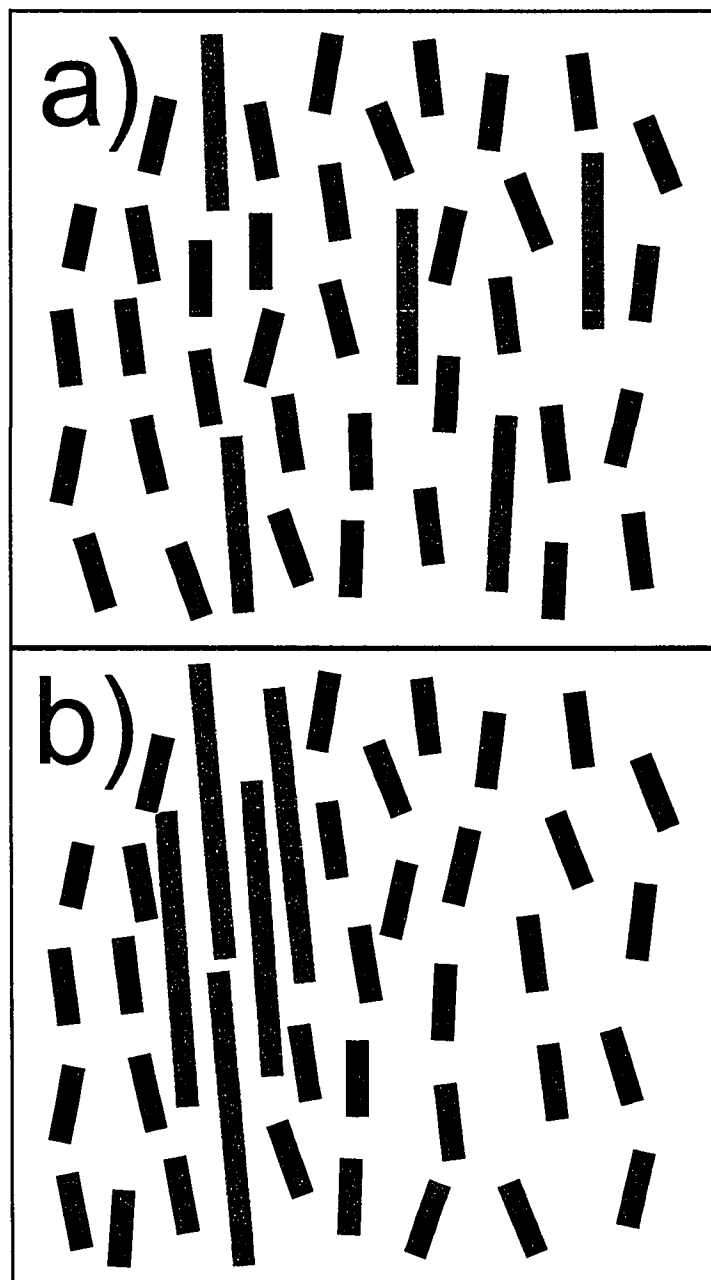


Figure 3.6: Cartoons of this theory's two main predictions [18]. Figure a) shows in a binary solution long rods have better alignment than short rods. Figure b) shows in a binary solution the long rods will phase separate out from the short rods when their length ratio exceeds 3.2.

polymer. It describes the energy cost to deform the polymer, and it is proportional to its persistence length  $l_p$ :

$$\beta F_1 = \frac{l_p}{2} \int_0^L dz \left( \frac{\partial \vec{t}}{\partial z} \right)^2. \quad (3.33)$$

The second term of the total free energy is the elastic energy of the nematic solvent. It describes the energy cost to deform the nematic solvent. There are three kinds of deformations: splay, twist and bending. Subsequently there are three elastic constants: splay constant  $K_1$ , twist constant  $K_2$ , and bending constant  $K_3$ . The nematic solvent's elastic energy is as below:

$$\beta F_2 = \frac{1}{2} \int d^2 \vec{\rho} \int dz [K_1 (\vec{\nabla}_\perp \cdot \delta \vec{n})^2 + K_2 (\vec{\nabla}_\perp \times \delta \vec{n})^2 + K_3 (\partial_z \delta \vec{n})^2]. \quad (3.34)$$

The third term of the total free energy is the coupling energy between the polymer and the nematic solvent. It describes the interaction between the polymer and the nematic solvent. And the coupling energy is proportional to the coupling constant  $\Gamma$ :

$$\beta F_3 = \frac{\Gamma}{2} \int_0^L dz (\vec{t}(z) - \delta \vec{n}_\perp(\vec{r}(z), z))^2. \quad (3.35)$$



Thus the system's total free energy can be expressed as:

$$\begin{aligned}
\beta F &= \beta F_1 + \beta F_2 + \beta F_3 \\
&= \frac{l_p}{2} \int_0^L dz \left( \frac{\partial \vec{t}}{\partial z} \right)^2 + \frac{\Gamma}{2} \int_0^L dz (\vec{t}(z) - \delta \vec{n}_\perp(\vec{r}(z), z))^2 \\
&\quad + \frac{1}{2} \int d^2 \vec{\rho} \int dz [K_1 (\vec{\nabla}_\perp \cdot \delta \vec{n})^2 + K_2 (\vec{\nabla}_\perp \times \delta \vec{n})^2 + K_3 (\partial_z \delta \vec{n})^2]. \quad (3.36)
\end{aligned}$$

It is not easy to exactly solve for the free energy. However we can get exact solutions by solving in two simplified limits of the free energy. One limit is when  $K$  is very large; in this case we can ignore the background nematic field's fluctuation. The other limit is when  $K$  is smaller, and the nematic background's fluctuation is large. In this case the polymer's fluctuations are locked with the nematic director's background fluctuations. For the case when  $K$  is very large, the system's free energy can be simplified to:

$$\beta F = \frac{l_p}{2} \int_0^L dz \left( \frac{\partial \vec{t}}{\partial z} \right)^2 + \frac{\Gamma}{2} \int_0^L dz \vec{t}_\perp^2. \quad (3.37)$$

This free energy can be used to describe any polymer in an external field.

To parameterize the polymer, we define  $\vec{R}_\perp(z)$  as polymer's deviation from nematic director. Then in cylindrical coordinate system we define  $\vec{R}(z) = (\vec{R}_\perp(z), z)$  (as shown in Fig. 3.7). And

$$\vec{t} \cong \left[ \frac{\partial \vec{R}_\perp}{\partial z}, 1 - \frac{1}{2} \left( \frac{\partial \vec{R}_\perp}{\partial z} \right)^2 \right]. \quad (3.38)$$

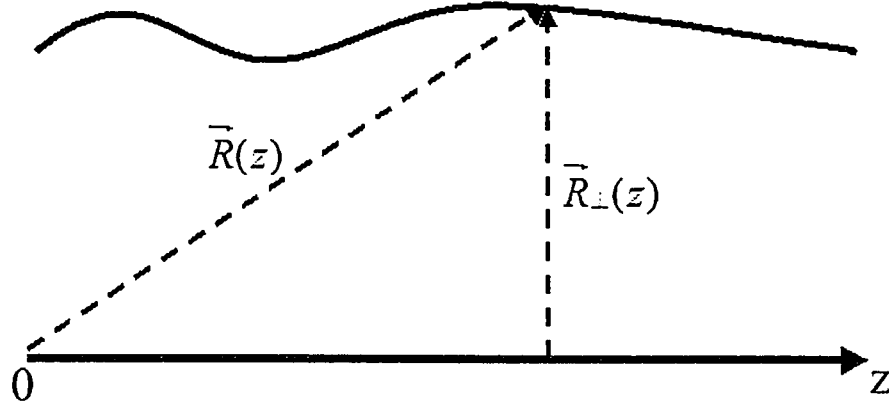


Figure 3.7: Schematic of a polymer in the background nematic field; the conformation of the polymer is parameterized by  $\vec{R}(z) = (\vec{R}_\perp(z), z)$ . The nematic director points along the  $z$  axis.

Thus, the system's free energy can be expressed as:

$$\beta F = \frac{l_p}{2} \int_0^L dz \left( \frac{\partial^2 \vec{R}_\perp}{\partial z^2} \right)^2 + \frac{\Gamma}{2} \int_0^L dz \left( \frac{\partial \vec{R}_\perp}{\partial z} \right)^2. \quad (3.39)$$

Let  $\vec{R}_\perp(z) = \sum_{n=1}^{\infty} \vec{R}_n \sin(\frac{n\pi z}{L})$ . Finally, we obtain:

$$\beta F = \frac{L}{2} \sum_n \left[ \frac{l_p}{2} \left( \frac{n\pi}{L} \right)^4 + \frac{\Gamma}{2} \left( \frac{n\pi}{L} \right)^2 \right] \vec{R}_n^2. \quad (3.40)$$

Equipartition theory states that:

$$\langle \vec{R}_m \cdot \vec{R}_n \rangle = \delta_{mn} \cdot \frac{2}{L} \cdot \frac{1}{l_p \left( \frac{n\pi}{L} \right)^4 + \Gamma \left( \frac{n\pi}{L} \right)^2}. \quad (3.41)$$

For the tangent-tangent correlation function, we have

$$\begin{aligned}
\langle \vec{t}(z) \cdot \vec{t}(0) \rangle &= \langle \vec{t}_\perp(z) \cdot \vec{t}_\perp(0) \rangle + \langle \vec{t}_z(z) \vec{t}_z(0) \rangle \\
&= 1 - \langle \vec{t}_\perp^2(z) \rangle + \langle \vec{t}_\perp(z) \cdot \vec{t}_\perp(0) \rangle \\
&= 1 - \int_0^\infty \frac{dq}{\pi} \frac{1 - \cos(qz)}{l_p q^2 + \Gamma} \\
&= 1 - \frac{1}{2\sqrt{l_p \Gamma}} [1 - e^{-\sqrt{\frac{\Gamma}{l_p}} z}].
\end{aligned} \tag{3.42}$$

For the case when  $K$  is small, we can minimize the free energy with respect to  $\vec{t}_\perp(z)$ , and we obtain

$$-l_p \frac{\partial^2 \vec{t}_\perp}{\partial z^2} + \Gamma [\vec{t}_\perp - \delta \vec{n}_\perp(0, z)] = 0. \tag{3.43}$$

Here with translation symmetry, we implicitly assume that  $\delta \vec{n}_\perp(\vec{r}(z), z) \approx \delta \vec{n}_\perp(0, z)$ .

With Fourier transformation, we get:

$$\vec{t}_\perp(q_z) = \frac{\delta \vec{n}_\perp(0, q_z)}{\lambda^2 q_z^2 + 1}. \tag{3.44}$$

where  $\lambda = \sqrt{\frac{l_p}{\Gamma}}$  is the Odijk deflection length.

For small fluctuations, we have:

$$\begin{aligned}
\vec{t}_z &= \sqrt{1 - \vec{t}_\perp^2} \\
&\approx 1 - \frac{1}{2} \vec{t}_\perp^2.
\end{aligned} \tag{3.45}$$

Thus, we can express TTCF as below:

$$\langle \vec{t}(z) \cdot \vec{t}(0) \rangle = 1 - [\langle \vec{t}_\perp^2(0) \rangle - \langle \vec{t}_\perp(z) \cdot \vec{t}_\perp(0) \rangle]. \quad (3.46)$$

With translation symmetry, we have

$$\begin{aligned} \langle \vec{t}_\perp(z) \cdot \vec{t}_\perp(0) \rangle &= \int_0^L \frac{ds}{L} \langle \vec{t}_\perp(z+s) \cdot \vec{t}_\perp(s) \rangle \\ &= \int_0^L \frac{ds}{L} \langle \vec{t}_\perp(z+s) \cdot \vec{t}_\perp(s) \rangle \\ &= \int_0^L \frac{ds}{L} e^{i(q_z+q'_z)s} \int_0^\infty \frac{dq_z}{\pi} \cos(q_z z) \vec{t}_\perp(q_z) \int_0^\infty \frac{dq'_z}{\pi} \vec{t}_\perp(q'_z) \\ &= \int_0^\infty \frac{dq_z}{\pi} \cos(q_z z) \vec{t}_\perp(q_z) \vec{t}_\perp(-q_z). \end{aligned} \quad (3.47)$$

By combining Equation 3.46 and Equation 3.47, we obtain:

$$\langle \vec{t}(z) \cdot \vec{t}(0) \rangle = 1 - \int_0^\infty \frac{dq_z}{\pi} \frac{(1 - \cos(q_z z)) \langle \delta \vec{n}_\perp(0, q_z) \cdot \delta \vec{n}_\perp(0, -q_z) \rangle}{(1 + q_z^2 \lambda^2)^2}. \quad (3.48)$$

As shown in Equation 3.48, the TTCF is related to the background nematic field's fluctuation. As we have mentioned, the third term in the system's total free energy independently describes the nematic background's elastic energy. With Fourier transformation and applying equipartition theorem, we obtain:

$$\langle \delta \vec{n}(\vec{q}_\perp, q_z) \cdot \delta \vec{n}(-\vec{q}_\perp, -q_z) \rangle = \frac{1}{K_1 q_\perp^2 + K_3 q_z^2}. \quad (3.49)$$

Furthermore, we get:

$$\begin{aligned}
\langle \delta \vec{n}(0, q_z) \cdot \delta \vec{n}(0, -q_z) \rangle &= \int \frac{d^2 q_{\perp}}{(2\pi)^2} \frac{1}{K_1 q_{\perp}^2 + K_3 q_z^2} \\
&= \frac{1}{4\pi K_1} \log\left[1 + \frac{K_1}{K_3} \frac{\Lambda^2}{q_z^2}\right].
\end{aligned} \tag{3.50}$$

where  $\Lambda = \frac{2\pi}{a}$ , and  $a$  is the radius of the polymer. If we plug Equation 3.50 into Equation 3.48, we finally get an explicit expression for TTCF:

$$\langle \vec{t}(z) \cdot \vec{t}(0) \rangle = 1 - \frac{1}{4\pi^2 K_1 \lambda} \int_0^\infty dx \frac{\{1 - \cos[x(\frac{z}{\lambda})]\} \log(1 + \frac{D^2}{x^2})}{(1 + x^2)^2}. \tag{3.51}$$

where the cutoff  $D$  satisfies  $D^2 = \frac{K_1}{K_3} (\Lambda \lambda)^2 = \frac{4\pi^2 K_1}{K_3} (\frac{\lambda}{a})^2$ .

Unfortunately, Equation 3.51 can not be evaluated analytically, but we can numerically solve it. The exact solution turns out to be:

$$\langle t_x(z + z') t_x(z') \rangle = \frac{\exp(-z/\lambda)}{4\Gamma\lambda} + \frac{1}{8\pi^2 K \lambda} \int_0^\infty \frac{\cos(xz/\lambda) \log(1 + \frac{D^2}{x^2}) dx}{(1 + x^2)(1 + x^2 + \frac{\Gamma x^2}{4\pi K} \log(1 + \frac{D^2}{x^2}))}. \tag{3.52}$$

where  $K$  is the nematic elastic constant. Here  $K = K_1 = K_2 = K_3$ , this is the result obtained by de Gennes by explicitly carrying out the integration over the nematic field [85].

It turned out this theory explains our experimental results quite well. The fitting curves based on this theory are in good agreement with experimental data. The fitting results, Odijk deflection length ( $\lambda$ ), nematic elastic constant ( $K$ ), and coupling constant ( $\Gamma$ ) agree with intuition or previous result.

## 3.5 Results

### 3.5.1 Coil-Rod transition

Our qualitative observations are summarized in Fig. 3.8. From Fig. 3.8a to Fig. 3.8d, there are the configurations of DNA, neurofilaments, wormlike micelles and f-actin in isotropic solutions (left hand side), and there are the configurations of the four polymers in nematic fd solutions (right hand side). The neurofilament, wormlike micelle and f-actin are coil-like in the isotropic solution. However, in the nematic fd solution those filaments are highly elongated as rigid rods. For higher concentrations of polymer, as shown in Fig. 3.8a, all the filaments are elongated along the same direction in the nematic solvent, which indicates that all the polymers point along the direction of the background nematic director. Thus, a coil-rod phase transition is observed for the biopolymers as the background suspension changes from isotropic to nematic phases.

However, the situation is different for DNA. Perhaps because of its small persistence length ( $L_p=0.05 \mu\text{m}$ ), the DNA molecules just form spherical droplets when they are in the isotropic phase. When we add them into the nematic fd solution, we find they collapse into anisotropic droplets. From the size and the large light intensity of the droplets, we conclude that there are quite a few DNA molecules in a single droplet. This observation indicates that DNA is immiscible in nematic fd suspensions. At low ionic strength (5 mM salt concentration) where the difference between the effective diameters of DNA and fd virus can be ignored, we still observe a demixing transition. Since the contour length

of DNA and neurofilament are about the same order, we believe that persistence length determines whether the biopolymer mixes or demixes in nematic fd suspensions.

Theory predicts that a binary solution of perfectly rigid rods will undergo an entropy driven phase separation if the length ratio is larger than 3.2 [18]. To our knowledge, this theory has not been extended to the semi-flexible case yet. Nevertheless our experimental results indicate that the persistence length is an important parameter to determine the solubility of polymer in the nematic liquid crystals. The persistence length ratio between DNA and fd is 44, which clearly corresponds to demixing behavior, while the persistence length ratio between neurofilament and fd is 11, which evidently corresponds to mixing behavior.

Finally, we also observe the existence of hairpin defects as the one shown in Fig. 3.8e. The formation of hairpins costs energy and they have been observed rarely and only indirectly [86, 87].

### **3.5.2 Orientational Distribution Function and Order Parameter S**

Wormlike micelles and actin gave high quality optical microscopy images. Their contour lengths were also sufficiently long for further quantitative image processing. Thus we focused on these two polymers for all further quantitative data analysis.

We used IDL as our programming language for quantitative image analysis. In our program, we mark a filament by manually clicking on the two ends of the filament. After we recognize the filament, we Gaussian fit its intensity profile perpendicular to its backbone.

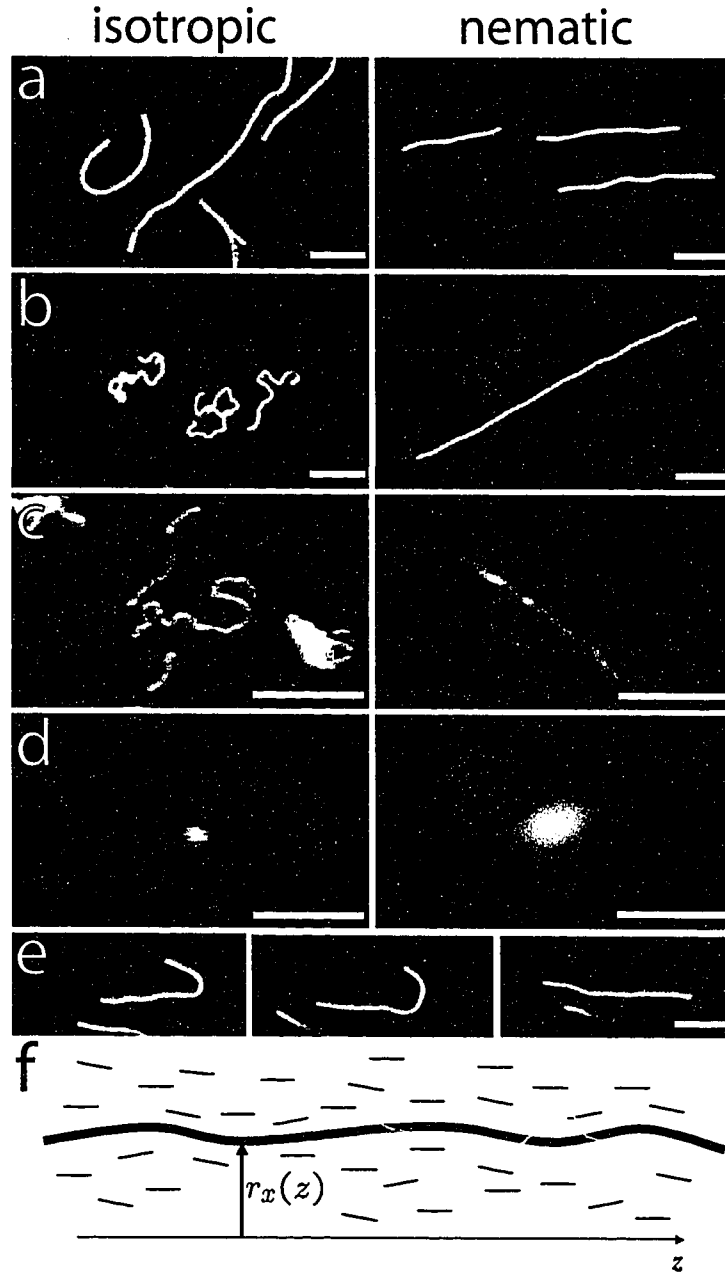


Figure 3.8: Images of fluorescently labelled biopolymers in the isotropic (left) and nematic (right) phase of fd virus. Figures (a)-(d) are, respectively, the images of actin, wormlike micelles, neurofilaments and DNA. (e) A sequence of images illustrating an actin filament escaping from a hairpin defect. The scale bar indicates  $5 \mu\text{m}$ . (f) Schematic of a biopolymer in the background nematic field; the conformation of the polymer is parameterized by  $\mathbf{R}(z) = (r_x(z), r_y(z), z)$ . The nematic director points along the  $z$  axis.



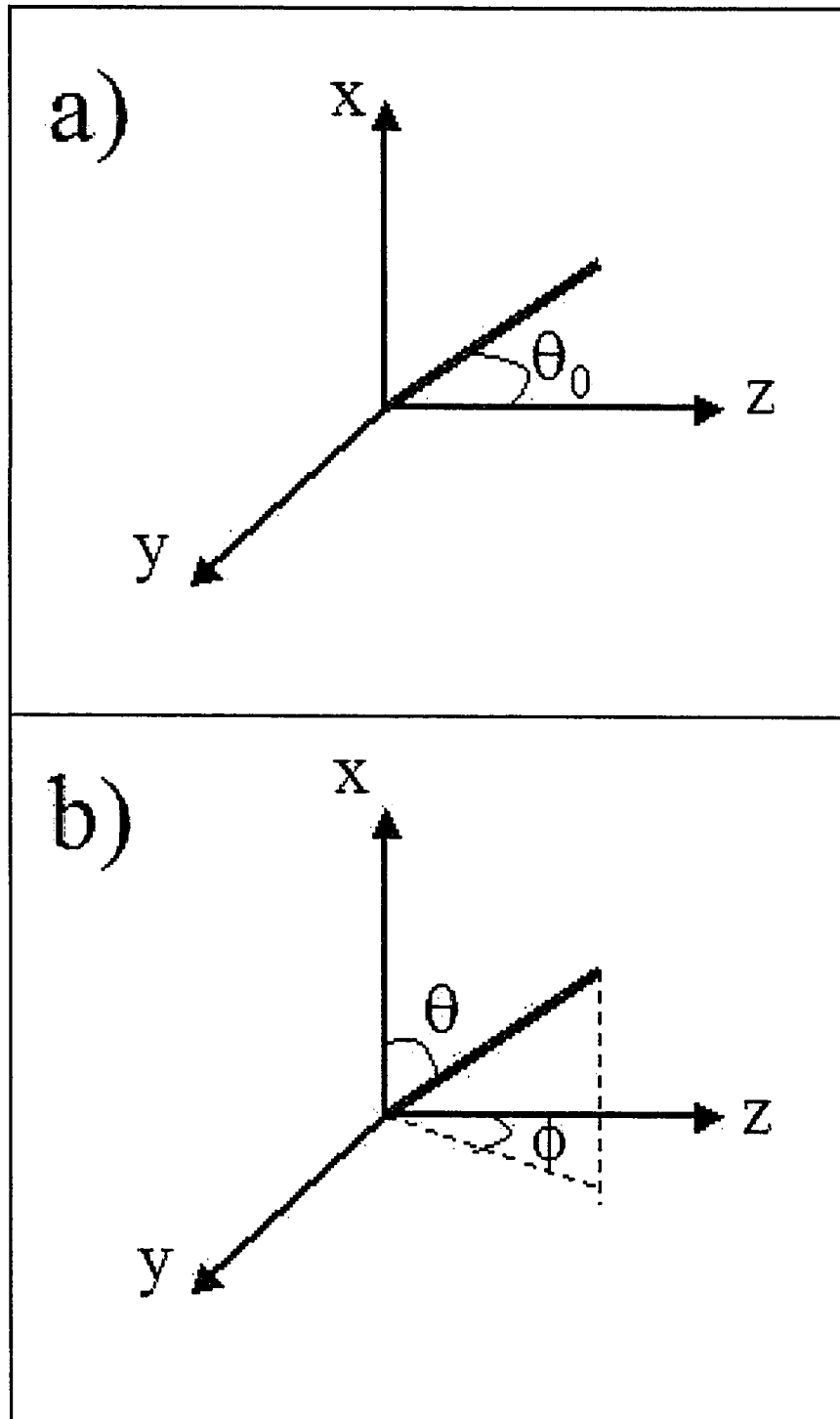


Figure 3.9: Schematics of definitions of the angles. Figure a) is the definition of angle  $\theta_0$ . Figure b) is the definition of angles  $(\theta, \phi)$ .

This Gaussian fit enables us to achieve sub-pixel accuracy of the polymer's configuration. After we obtain the configuration of the filaments, we are able to proceed with further quantitative analysis. For each sample, we took movies of ten filaments. For each movie, we took about 50 to 100 images with a time interval of around half second. Our data analysis shows that there exists no correlation between consecutive images. Thus, we explore most of the possible configurations of these polymer filaments. In our experiment, our temporal resolution is limited by the samples' exposure time. We set the exposure time as 250 ms in order to achieve clear images. As for spatial resolution, due to random noise, we are unable to obtain reliable data on the first  $\sim 0.5 \mu\text{m}$  of the tangent-tangent correlation function.

The first quantitative analysis focused on the polymer's order parameter. In our experiment the director of nematic field is located inside the observation plane. Thus there are two important directions in our system: one is the director and the other one is the one perpendicular to the observation plane. We define the z axis to be along the director direction and the x axis to be perpendicular to the observation plane. Therefore we have to define two sets of angles (as shown in Fig. 3.9): one is  $\theta_0$ , the angle between the polymer tangent direction and z axis, and it is the polymer's 3D deviation angle from the director; the other set angles are  $(\theta, \phi)$ , the spherical coordinates with x axis as the azimuthal axis, and  $\phi$  is the polymer's 2D deviation angle from the nematic director. The angle we measured is  $\phi$ . For small angles, we have  $\theta_0^2 = (\theta - \frac{\pi}{2})^2 + \phi^2$  (see Appendix). Thus  $\theta_0$ ,  $\theta$ , and  $\phi$  share the same probability distribution function. Furthermore, we parameterize the transverse

deviations of the polymer from the  $z$  axis by the 2-component vector  $\mathbf{r}(z)$ , as shown in Fig. 3.8f. In our experiment, we only observe a 2D projection of the polymer's 3D fluctuation. We lose track of polymer's out-of-plane motion during optical microscopy. However, for small fluctuations, with rotational symmetry, the polymer's 3D fluctuation is simply twice that of its 2D projection. Thus optical microscopy is still a powerful tool for the study of polymer's 3D fluctuation. Since our images are 2D projections of the polymer fluctuating in 3D, the  $x$ -component of the tangent vector is measured by  $t_x(z) = \partial r_x(z)/\partial z \approx \phi(z)$ . The ODF is obtained by creating a histogram of angle  $\phi$  at different positions along the contour length for a time sequence of 50-100 images. The experimental obtained ODF is plotted in the inset of Fig. 3.10; as expected, it is well approximated with a Gaussian profile:  $\Psi(\phi) = \exp(-\frac{\phi^2}{2\alpha^2})(-\pi \leq \phi < \pi)$ . Since they share the same distribution function,  $\theta$  and  $\theta_0$  are also Gaussian distributed. From ODF, we can obtain  $\langle t_x^2 \rangle$ , which is related to  $\alpha$ , the half width of the gaussian profile:

$$\langle t_x^2 \rangle = \frac{\int_{-\pi}^{\pi} \phi^2 \exp(-\frac{\phi^2}{2\alpha^2}) d\phi}{\int_{-\pi}^{\pi} \exp(-\frac{\phi^2}{2\alpha^2}) d\phi}. \quad (3.53)$$

Once we obtain  $\langle t_x^2 \rangle$ , and assume  $\langle t_x^2 \rangle = \langle t_y^2 \rangle$ , ( $t_y \approx \frac{\pi}{2} - \theta$ ), we can extract the filament's order parameter using the following relation:

$$S = \int_0^L dz \langle 3(\mathbf{t}(z) \cdot \hat{\mathbf{z}})^2 - 1 \rangle / (2L). \quad (3.54)$$

where for small fluctuations,

$$\begin{aligned} S(z) &= \frac{1}{2} \langle 3(\mathbf{t}(z) \cdot \hat{\mathbf{z}})^2 - 1 \rangle = \frac{1}{2} \langle 3\cos^2(\theta_0) - 1 \rangle \\ &\approx \langle 1 - \frac{3}{2}\theta_0^2 \rangle. \end{aligned} \quad (3.55)$$

and we have

$$\theta_0^2 = (\theta - \frac{\pi}{2})^2 + \phi^2, \quad (3.56)$$

$$(\theta - \frac{\pi}{2})^2 = \phi^2. \quad (3.57)$$

Thus

$$\begin{aligned} S &= \langle \frac{3}{2}(\mathbf{t}(z) \cdot \hat{\mathbf{z}})^2 - \frac{1}{2} \rangle = \langle 1 - \frac{3}{2}\theta_0^2 \rangle \\ &= \langle 1 - 3\phi^2 \rangle = \langle 1 - 3t_x^2 \rangle \end{aligned} \quad (3.58)$$

$$= \frac{\int_{-\pi}^{\pi} (1 - 3\phi^2) \exp(-\frac{\phi^2}{2\alpha^2}) d\phi}{\int_{-\pi}^{\pi} \exp(-\frac{\phi^2}{2\alpha^2}) d\phi}. \quad (3.59)$$

In Fig. 3.10, we plot the order parameter of actin versus that of background nematic order parameter. The order parameter of the background fd nematic phase increases with increasing fd concentration and is well understood [96]. Previous X-ray experiments mapped out the relationship between fd solution's order parameter and its concentration. In this experiment, the director is perpendicular to the observation plane, so this measurement is a 3D one. We determined our samples' fd concentration by UV absorption. The absorption takes place at 269 nm with an absorption coefficient of 3.84 cm<sup>2</sup>/mg.

Thus, as long as we know the background fd concentration, we can determine the nematic background's order parameter. In Fig 3.9, we observe that actin's order parameter is significantly higher than the background nematic fd's order parameter. For example, when the background nematic fd's order parameter is around 0.7, the elongated polymer's order parameter is around 0.9. The difference between the order parameters of polymers and of background fd can be understood in the context of the theoretical work on a bidisperse mixture of hard rod-like particles of different lengths [18]. This theoretical work predicts that in a nematic, coexistence of long hard rods and short hard rods, the long hard rods' order parameter is higher than the short hard rods' order parameter. In our experiment, we only choose polymer lengths above  $10\text{ }\mu\text{m}$  to analyze, while fd's length is around  $1\text{ }\mu\text{m}$ . This is in qualitative agreement with our observations.

To further understand this length-dependent order behavior, we obtain  $S_{actin}$  for filaments with different contour lengths. In Fig. 3.11, the actin filament's order parameter decreases with a decrease in the filament length. The trend suggests that  $S_{actin}$  will reach  $S_{fd}$  when the actin's length approximately equals fd's length. This is again qualitatively in agreement with the theory [18]. Since both actin filaments and fd virus are semiflexible polymers, we did not attempt a quantitative comparison of the experiment data and theoretical predictions (for hard rods).

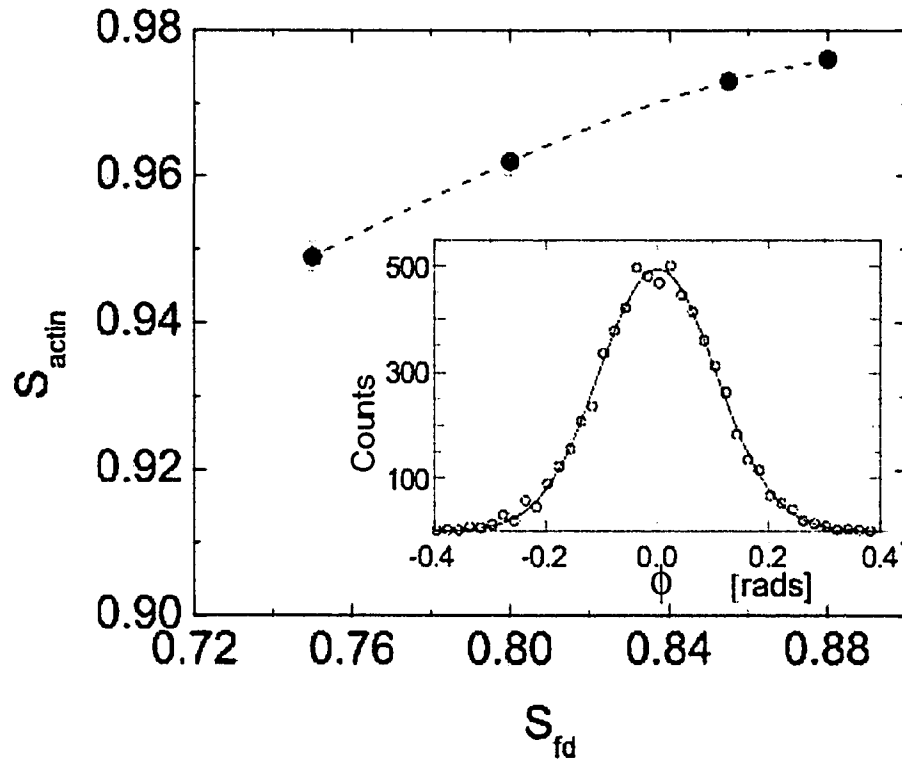


Figure 3.10: The order parameter of actin filaments ( $S_{actin}$ ) vs. the order parameter of the background fd nematic ( $S_{fd}$ ). Dashed line is a guide to the eye. The contour length of actin filaments is  $15\mu\text{m}$  or higher. Inset: The orientational distribution function (ODF) of actin filaments. The ODF is well approximated by a gaussian for a wide range of concentrations.

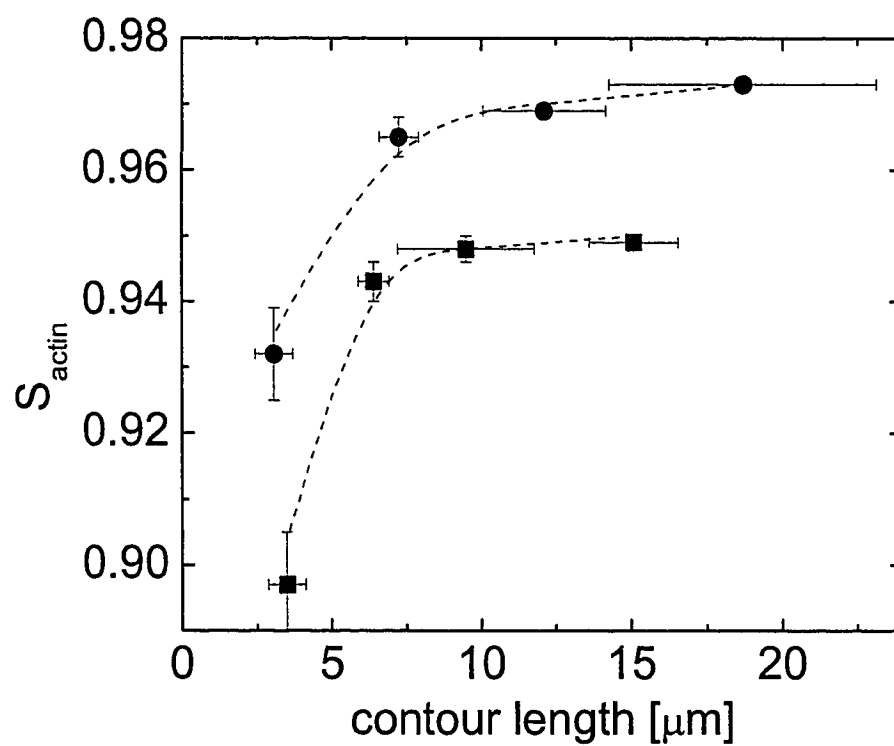


Figure 3.11:  $S_{actin}$  vs. contour lengths of actin. The concentrations of the background nematic fd are 41 mg/ml (circles,  $S_{fd}=0.75$ ) and 28 mg/ml (squares,  $S_{fd}=0.855$ ). Dashed lines are a guide to the eye.

### 3.5.3 Tangent-tangent Correlation Function (TTCF)

From the ODF, we characterized the polymer filament's independent local fluctuations and were able to define an order parameter for the polymer. It is perhaps even more useful to obtain correlations between the polymer's local fluctuations at different locations on the filament. The x-component of the TTCF, ( $\langle t_x(z + z')t_x(z') \rangle$ ), describes how orientational fluctuations decay along the direction of the polymer.

In our experiment, we measured the TTCF for wormlike micelles at concentrations of background fd virus of 40 mg/ml and above. At lower fd concentrations the fluctuations of wormlike micelles are large and spontaneous formation and dissolution of hairpin defects is observed. In this regime it is not clear how to define the ground state. Therefore we focus our analysis on the regime where the background order parameter is high and consequently the amplitude of the polymer fluctuation is low. This makes our data better suited for comparison to existing theoretical models.

Theoretically the fluctuation of a polymer in a nematic phase can be described by the following free energy:

$$\beta F = \frac{l_p}{2} \int_0^L dz \left( \frac{\partial \vec{t}_\perp}{\partial z} \right)^2 + \frac{\Gamma}{2} \int_0^L dz (\vec{t}_\perp(z) - \delta \vec{n}(0, z))^2 + \frac{K}{2} \int dz \int d^2 \vec{r} (\nabla \delta \vec{n})^2 \quad (3.60)$$

where  $l_p$  is the persistence length of the semiflexible polymer,  $\Gamma$  is the strength of the coupling of the polymer to the background nematic field,  $\delta \vec{n}$  is the local direction of the



fluctuating nematic field and  $K$  is the nematic elastic constant. Combining the two initial parameters  $l_p$  and  $\Gamma$ , we obtain a new length scale  $\lambda = \sqrt{l_p/\Gamma}$ , which is the Odijk deflection length [100]. In nematic solvent the polymer freely wanders until it meets the nematic background polymer and is forced to deflect back along the nematic director. The Odijk deflection length is the length for which the polymer freely wanders.

The system's free energy is relatively easy to solve in two limits. One limit is when the elastic constant,  $K$ , is very large and therefore the fluctuations of the nematic field can be ignored (i.e.  $\delta\vec{n} = 0$ ). In this case, the TTCF has a simple form:  $\langle t_x(z+z')t_x(z') \rangle \propto \exp(-z/\lambda)$ . In the other limit  $K$  is smaller, and the internal fluctuations of the polymer are negligible. In this case the polymer fluctuations are driven by a tight coupling to the fluctuations of the background nematic field. This approximation leads the TTCF to decay as a power law which depends on  $K$ , the nematic solvent's elastic constant. If we solve for the TTCF exactly, we obtain:

$$\langle t_x(z+z')t_x(z') \rangle = \frac{\exp(-z/\lambda)}{4\Gamma\lambda} + \frac{1}{8\pi^2 K\lambda} \int_0^\infty \frac{\cos(xz/\lambda) \log(1 + \frac{D^2}{x^2}) dx}{(1+x^2)(1+x^2 + \frac{\Gamma x^2}{4\pi K} \log(1 + \frac{D^2}{x^2}))}. \quad (3.61)$$

In Equation 3.61, the first term can be ignored for  $z \gg \lambda$ . Thus, the polymer's large wavelengths fluctuations are always dominated by the second term, which is due to the coupling to the nematic field.

We theoretically fit the experiment data with our theory result. The software we used

is MATLAB. We numerically expand our theory result with Matlab. There are four parameters in the numerical expansion:  $\Gamma$ ,  $\lambda$ ,  $D$ , and  $K$ . There are only two free parameters:  $\Gamma$  and  $K$ .  $\lambda$  is a function of  $\Gamma$  and  $l_p$ , and  $l_p$  is a known physical value.  $D$  is a function of  $\Gamma$  and the polymer's diameter. The polymer's diameter is also known. Thus we only fit two parameters:  $\Gamma$  and  $K$ . By minimizing the square deviation of the theoretical curve from the experiment data, we are able to locate the optimum values of  $\Gamma$  and  $K$ . As shown in Fig. 3.12, theory and experiment do not agree at distances smaller than  $0.5 \mu\text{m}$ . We believe this is due to limited spatial and temporal resolution of our microscope. When observed with a microscope, the wormlike micelles appear as sharp rapidly fluctuating objects. Due to a weak fluorescent signal, we acquire an image for 250 msec. Over this timescale fast fluctuations at short wavelengths are effectively averaged out. This results in measured value of the TTCF which is lower than its true value.

Another reason for the discrepancy is the fact that a length over which the polymer changes directions (Odijk deflection length) is smaller than the spatial resolution of the microscope. At distances above  $0.5 \mu\text{m}$  the agreement between the theory and experiments is quite good. At these distances, most of the fluctuations of the worms are driven by their coupling to the background nematic field, coming from the second term in Equation 3.61. A best-fit value of  $l_p$  is found to be  $1.5 \mu\text{m}$ , which is somewhat higher than previous measurement [93]. From the fits of the data, we extract the values of the Odijk deflection length  $\lambda$ ,  $K$ , and  $\Gamma$ , as listed in Table 3.2. We observe that with increasing fd

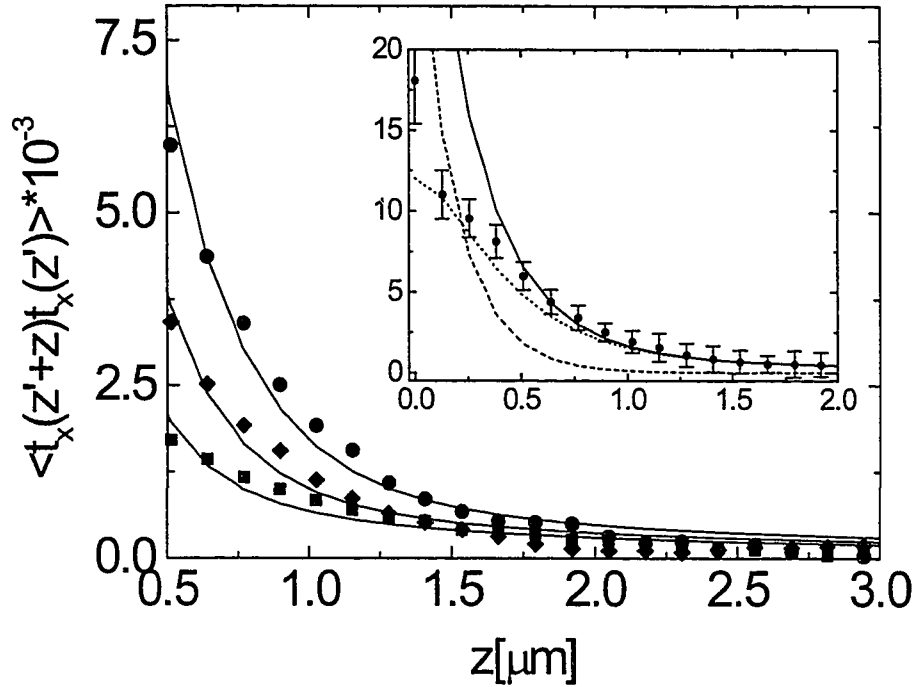


Figure 3.12: The x component of the tangent-tangent correlation function for wormlike micelles measured at three different fd concentrations ( $c_{fd}$ ). With increasing fd concentration, the overall magnitude of the correlation function correlation decreases. The solid lines are theoretical curves generated from our theoretical model with the best-fit parameters listed in Table 4.2. Inset: TTCF for the lowest concentration of the fd virus. The dashed and dotted lines are, respectively, the contributions from the first and the second terms in the theoretical model. The data points below  $0.5 \mu m$  are unreliable and have been excluded from the fitting.

concentration,  $\lambda$  decreases, while  $K$  and  $\Gamma$  increase, as one would intuitively expect. Finally, we note that the values for  $K$  are in good agreement with previous measurements of twist elastic constant  $K_{22} = 3 \cdot 10^{-8}$  dyne for fd samples prepared under similar conditions [99]. The fitting results are as shown in Table 3.2.

Table 3.2: The Fitting Results of TTCF for the Samples of Wormlike Micelles in fd Solution

$c_{fd}$ [mg/ml]	$\lambda$ [ $\mu\text{m}$ ]	$K$ [ $10^{-8}$ dyne]	$\Gamma$ [ $1/\mu\text{m}$ ]
39	0.18	1.9	46
51	0.13	2.4	88
97	0.06	2.8	416

## 3.6 Conclusion

In conclusion, we have shown that direct visualization of semiflexible polymers is a powerful tool to study polymer liquid crystals. Using direct visualization we show semiflexible polymers dissolved in a background fd solution will experience a coil-rod phase transition when we change the background solvent from isotropic to nematic. In addition, we show the polymer fluctuations are driven by fluctuations of the background nematic field. Dissolving semiflexible polymers in nematic liquid crystals provides an easy way to achieve high alignment of polymers which might be complimentary to existing techniques.

## 3.7 Appendix

### 3.7.1 Appendix A: Isotropic-Nematic Phase Transition

There is a good review paper by Lekerkerker on this topic [108]. In 1949, Onsager predicted that hard rod solution would experience an isotropic to nematic phase transition when we increased the rod's concentration. By definition, the nematic phase is a phase

that all the rods try to align the same direction, while their centers are liquid like. Onsager proved that this isotropic-nematic (I-N) phase transition was a result of the anisotropic shape of the rods and the excluded volume effect. Basically, Onsager virial expanded the rod system's free energy up to the second order, which limited his theory to the case of  $L/D > 100$ :

$$\begin{aligned} \frac{F}{k_B T} = \frac{F_{id} + F_{ex}}{k_B T} = \int_V d\Omega d\mathbf{r} \rho(\Omega, \mathbf{r}) \ln(\rho(\mathbf{r}, \Omega)) - \\ \frac{1}{2} \int_V d\mathbf{r}_1 d\Omega_1 \int_V d\mathbf{r}_2 d\Omega_2 \rho(\mathbf{r}_1, \Omega_1) \rho(\mathbf{r}_2, \Omega_2) \Psi(\mathbf{r}_1, \mathbf{r}_2, \Omega_1, \Omega_2). \end{aligned} \quad (3.62)$$

where  $\Psi(\mathbf{r}_1, \mathbf{r}_2, \Omega_1, \Omega_2)$  is the Meyer-Meyer overlap function. Its value will be -1 if there exists any overlap between two particles, whose centers are located at  $\mathbf{r}_1$  and  $\mathbf{r}_2$ , and long axis oriented along  $\Omega_1$  and  $\Omega_2$ . Otherwise its value is zero. Since the system is spatial uniform, we can assume  $\rho(\mathbf{r}, \Omega) = (N/V)f(\Omega)$ . Normalization requires:

$$\int f(\Omega) d\Omega = 1. \quad (3.63)$$

By minimizing Equation 3.63 with respect to the orientation distribution function  $f(\Omega)$ , we obtain the following integral equation:

$$\log[4\pi f(\theta)] = \lambda - \frac{8\rho}{\pi} \int K(\theta, \theta') f(\theta') d\theta, \quad (3.64)$$

where  $\rho$  is the dimensionless density  $\frac{\pi}{4}L^2D\frac{N}{V}$ . and

$$\begin{aligned} K(\theta, \theta') &= \int_0^{2\pi} d\phi |\sin \gamma| = \int_0^{2\pi} d\phi \sqrt{1 - (\cos \theta \cos \theta' + \sin \theta \sin \theta' \cos \phi)} \\ &= 2\pi \sum_{n=0}^{\infty} c_{2n} P_{2n}(\cos \theta). \end{aligned} \quad (3.65)$$

The integral equation (Equation 3.64) can not be solved analytically, but it can be solved numerically. However, Onsager used a trial function to solve this problem. The ansatz solution for the orientational distribution function is:

$$f(\alpha, \cos(\theta)) = \frac{\alpha \cosh(\alpha \cos(\theta))}{4\pi \sinh(\alpha)}. \quad (3.66)$$

Plug the ansatz into Equation 3.63, and we obtain an expression of the free energy which only depend on dimensionless concentration  $\rho$  and orientation parameter  $\alpha$ :

$$\begin{aligned} F(\alpha, \rho) &= \rho \log(\rho) + \sigma(\alpha)\rho + \xi(\alpha)\rho^2, \\ \sigma(\alpha) &= \log\left(\frac{\alpha \cosh(\alpha)}{4\pi \sinh(\alpha)}\right) - 1 + \frac{\arctan(e^\alpha) - \arctan(e^{-\alpha})}{\sinh(\alpha)}, \\ \xi(\alpha) &= \frac{2I_2(\alpha)}{\sinh^2(\alpha)}. \end{aligned} \quad (3.67)$$

where  $\rho \log(\rho)$  is the mixing entropy,  $\sigma(\alpha)\rho$  is orientation entropy, and  $\xi(\alpha)\rho^2$  is the packing entropy.

If we know the orientation distribution function, we can easily obtain the system's

nematic order parameter (S):

$$S = 2\pi \int_0^\pi \left( \frac{3}{2} \cos^2(\theta) - \frac{1}{2} \right) f(\theta) \sin(\theta) d\theta. \quad (3.68)$$

Kayser and Ravenche (1978) performed a bifurcation analysis on Equation 3.64. First of all, isotropic form of the trial function ( $f(\theta) = \frac{1}{4\pi}$ ) satisfies the integral equation at any concentration  $\rho$ . The bifurcation analysis starts with the isotropic ODF, and assumes that when  $\rho$  reaches a certain value, another solution of ODF will branch from the isotropic one. Thus, I-N phase transition happens. Near the branching point, the ODF deviates only infinitesimally (denoted by  $\epsilon$ ) from the isotropic one:

$$f(\theta) = \frac{1}{4\pi} (1 + \epsilon h(\theta)). \quad (3.69)$$

Substituting in Equation 3.64 and keeping the first order term of  $\epsilon$ ,

$$\begin{aligned} h(\theta) &= -\frac{8\rho}{\pi} \int K(\theta, \theta') \frac{h(\theta')}{4\pi} d\Omega' \\ &= -\frac{4\rho}{\pi} \sum c_{2n} P_{2n}(\cos \theta) \langle P_{2n} \rangle_h \end{aligned} \quad (3.70)$$

where  $\langle P_{2n} \rangle_h = \int_{-1}^1 P_{2n}(\cos \theta) h(\theta) d \cos \theta$ . It is obvious that all even Legendre polynomials fulfil Equation 3.70, but different orders corresponds to different  $\rho$ . The lowest

order corresponds to the smallest  $\rho$ , which is the bifurcation point  $\rho^*$ :

$$\rho^* = \left(-\frac{4c_2}{\pi} \langle P_2 \rangle\right)^{-1} = 4. \quad (3.71)$$

with

$$h(\theta) = P_2(\cos \theta). \quad (3.72)$$

Furthermore, when we determine the free energy with achieved bifurcation ODF, we find that:

$$\frac{\Delta F}{Nk_B T} = \ln \rho + \rho + \frac{1}{40}(4 - \rho)\epsilon^2. \quad (3.73)$$

At  $\rho = 4$ , the isotropic state changes from a local minimum to a local maximum. Thus the isotropic state becomes unstable when  $\phi = 4D/L$ , which is the onset concentration of I-N phase transition. Furthermore, we can discuss the I-N coexistence relation. We assume part of the solution is isotropic, and part of it is anisotropic. Their concentrations are  $\rho_i$  for isotropic phase, and  $\rho_a$  for anisotropic phase (From now on, we denote properties of the isotropic and anisotropic phase with subscripts i and a respectively). At coexistence, the two phases' osmotic pressure and the chemical potential should reach equilibrium:

$$\Pi_1(\rho_i) = \Pi_a(\rho_a), \quad \mu_1(\rho_i) = \mu_a(\rho_a). \quad (3.74)$$

We find:

$$\Pi = -(\partial \Delta F / \partial V)_{N,T,\mu_0,\mu_1,\dots} = \frac{k_B T}{v_0(L/D)}(\rho + \rho^2 \xi[f]). \quad (3.75)$$



and

$$\mu = -(\partial\Delta F/\partial N)_{V,T,\mu_0,\mu_1,\dots} = k_B T(\text{constant} + \ln \rho + \sigma[f] + 2\rho\xi[f]). \quad (3.76)$$

For the isotropic phase,  $\sigma = 0$  and  $\xi = 1$ . For the anisotropic phase, here we use Gaussian distribution function as our trial function for ODF. Thus we get:

$$\rho_i + \rho_i^2 = 3\rho_a, \quad (3.77)$$

$$\ln \rho_i + 2\rho_i = 3 \ln \rho_a + 3 + \ln\left(\frac{4}{\pi}\right). \quad (3.78)$$

From the above equations, we find the following coexisting concentrations:

$$\rho_i = 3.45, \quad \rho_a = 5.12, \quad S = 0.910. \quad (3.79)$$

Until now, we have assumed that the rods are hard, non-charged objects. However, real rod-like biopolymers are highly charged and flexible. For highly charged rods, the static coulomb repulsive interaction can be expressed as:

$$\frac{U_{el}(x)}{kT} = \frac{A'e^{-\kappa(x-D)}}{\sin(\gamma)}. \quad (3.80)$$

where  $x$  is the closest distance between two rods,  $A'$  is the proportionality constant,  $\kappa^{-1}$  is the Debye screening length, and  $\gamma$  is the angle between two rods. For charged rods,

both short range hard core excluded volume interaction and long range charge repulsive interaction will contribute to the second virial coefficient:

$$\begin{aligned}\beta(\gamma) &= -2DL^2 \sin(\gamma) + 2L^2 \sin(\gamma) \int_D^\infty (e^{-\frac{U_{el}(x)}{kT}} - 1) dx \\ &= -2DL^2 \sin(\gamma) - 2\kappa^{-1} L^2 \sin(\gamma) \left( \ln \left( \frac{A'}{\sin(\gamma)} \right) + C_E + E_1 \left( \frac{A'}{\sin(\gamma)} \right) \right).\end{aligned}\quad (3.81)$$

Integrating Equation 3.82 over a uniform orientation distribution function, we get:

$$B_2^{\text{iso}} = \frac{1}{4}\pi L^2 D_{\text{eff}} = \frac{1}{4}\pi DL^2 + \frac{1}{4}\pi\kappa^{-1} L^2 (\ln A' + C_E + \ln 2 - \frac{1}{2}). \quad (3.82)$$

Thus, for an isotropic solution, we can renormalize the charge interaction into  $D_{\text{eff}}$ . For the nematic solution, the situation is a little bit more complex because parallel rods have higher electrostatic energy than perpendicular ones. But for highly charged rods, the difference between the isotropic solution and the nematic solution is tiny. So we can view the charged rods with physical diameter  $D$  as hard rods with effective diameter  $D_{\text{eff}}$ .

For a flexible rod, its rigidity can be described by the persistence length. The persistence length is such a length that after which polymer forgets which direction it has pointed to. For rigid rod, its persistence length is infinite; while for random coil, its persistence length is of the order of the diameter of its monomer. When polymer's persistence length is much bigger than the monomer's diameter, this polymer is called a semi-flexible polymer. Theory has approximated a single semi-flexible rod's orientation entropy as Equation 3.83. The mixing entropy and packing entropy for semi-flexible polymers are

nearly the same as the hard rod if we ignore the higher order terms.

$$\sigma(\alpha, \frac{L}{P}) = \ln(\alpha) - 1 + \pi e^{-\alpha} + \frac{L}{6P}(\alpha - 1) + \frac{5}{12} \ln \left( \cosh \left( \frac{L}{P} \frac{\alpha - 1}{5} \right) \right). \quad (3.83)$$

Generally, increasing flexibility destabilized the nematic phase by shifting the I-N transition to higher volume fraction. Increasing the flexibility also drastically reduces the width of the concentration difference between the co-existing isotropic and nematic phases and the order parameter of the nematic phase.

### 3.7.2 Appendix B: Order Parameter S and Orientational Distribution Function

This subsection largely follows Tom Lubensky's book "principles of condensed matter physics" [11]. Liquid crystals are composed of rod-like molecules. In the isotropic phase, the orientations of the molecules are random. In the nematic phase, the long axes of those molecules are trying to point to the same direction. This particular direction is specified by a unit vector  $\mathbf{n}$  called the director. Thus the nematic phase has a broken rotational symmetry. It is reasonable to associate the order parameter with the unit vector  $\nu$  which points along the long axis of the molecule.  $\nu$  and  $-\nu$  are equivalent because of symmetry. Here we use a second rank tensor to sufficiently describe the system's order behavior. The system's order parameter should be zero when it is in the isotropic phase. A symmetric traceless tensor will yield zero when averaged over directions, so we construct the order

parameter from the symmetric traceless tensor formed from  $\nu$ . Let

$$Q_{ij} = \langle \nu_i \nu_j - \frac{1}{3} \delta_{ij} \rangle . \quad (3.84)$$

$\langle \underline{Q} \rangle$  is the tensor with components  $Q_{ij}$ . In a coordinate system with one axis along the direction of molecular alignment, the matrix  $\langle \underline{Q} \rangle$  is diagonal:

$$\langle \underline{Q} \rangle = \begin{pmatrix} \frac{2}{3}S & 0 & 0 \\ 0 & -\frac{1}{3}S + \eta & 0 \\ 0 & 0 & -\frac{1}{3}S - \eta \end{pmatrix} . \quad (3.85)$$

If  $\eta$  is nonzero,  $\langle \underline{Q} \rangle$  is biaxial. Except in exceptional cases, nematic liquid crystals are uniaxial so that  $\eta = 0$ . In this case,

$$\langle Q_{ij} \rangle = S(n_i n_j - \frac{1}{3} \delta_{ij}) . \quad (3.86)$$

where the unit vector  $\mathbf{n}$ , called the Frank director, specifies the direction of the principal axis of  $\langle Q_{ij} \rangle$ . From Equation 3.84, we have:

$$\sum_i \sum_j n_i \langle Q_{ij} \rangle n_j = \langle (\nu \cdot \mathbf{n})^2 - \frac{1}{3} \rangle . \quad (3.87)$$

From Equation 3.86, we have:

$$\sum_i \sum_j n_i \langle Q_{ij} \rangle n_j = \frac{2}{3} S. \quad (3.88)$$

Combining Equation 3.87 and Equation 3.88, we obtain the definition of order parameter

S:

$$\begin{aligned} S &= \frac{1}{2} \langle 3(\nu \cdot \mathbf{n})^2 - 1 \rangle = \frac{1}{2} \langle 3 \cos^2 \theta - 1 \rangle \\ &= \int_0^\pi \frac{1}{2} (3 \cos^2 \theta - 1) P(\theta) \sin \theta d\theta. \end{aligned} \quad (3.89)$$

where  $P(\theta)$  is the rod-like molecules' orientational distribution function. It can be defined as:

$$\int_{\theta_0 - \Delta\theta}^{\theta_0 + \Delta\theta} P(\theta) d\theta = \frac{n(\theta_0 - \Delta\theta, \theta_0 + \Delta\theta)}{N}. \quad (3.90)$$

where  $N$  is the total number of the particles, and  $n(\theta_0 - \Delta\theta, \theta_0 + \Delta\theta)$  is the total number of the particles in a subgroup. In the subgroup, the angles between the particles' long axes and the director fall in the range  $[\theta_0 - \Delta\theta, \theta_0 + \Delta\theta]$ .

Since the particles' fluctuation is related to the nematic order parameter, the orientational distribution function can also be defined as:

$$\int_{\theta_0 - \Delta\theta}^{\theta_0 + \Delta\theta} P(\theta) d\theta = \frac{t(\theta_0 - \Delta\theta, \theta_0 + \Delta\theta)}{T}. \quad (3.91)$$

where  $T$  is the total time over which we collect the data, and  $t(\theta_0 - \Delta\theta, \theta_0 + \Delta\theta)$  is the

total time when the angle between the particle's long axis and the director falls in the range  $[\theta_0 - \Delta\theta, \theta_0 + \Delta\theta]$ .

When the particles are perfectly aligned, the order parameter should be 1. The orientational distribution function should be a  $\delta$  function. Because of  $P(\nu) = P(-\nu)$ ,  $P(\theta) = \delta(\cos^2 \theta - 1)$ . Thus,

$$\begin{aligned}
 S &= \frac{1}{2} \int_0^\pi (3 \cos^2 \theta - 1) P(\theta) \sin \theta d\theta \\
 &= \frac{1}{2} \int_{-1}^1 dx (3x^2 - 1) \delta(x^2 - 1) \\
 &= \frac{1}{2} \int_{-1}^1 dx (3x^2 - 1) \left( \frac{\delta(x+1)}{2} + \frac{\delta(x-1)}{2} \right) \\
 &= 1.
 \end{aligned} \tag{3.92}$$

Here we used  $\delta(x^2 - 1) = \frac{\delta(x+1)}{2} + \frac{\delta(x-1)}{2}$ .

Our experiment system is composed of long semi-flexible polymers immersed in nematic solvent. Those polymers elongate along and fluctuate around the nematic solvent's director. Based on polymer's fluctuation, we can define the polymer's orientation distribution function as defined by Equation 3.91. In a strong nematic field, the orientation distribution function can be approximated by a Gaussian distribution:

$$\begin{aligned}
 P(\theta_0) &\equiv A \exp\left(-\frac{\theta_0^2}{2\alpha^2}\right), & (0 \leq \theta_0 \leq \frac{\pi}{2}) \\
 &\equiv A \exp\left(-\frac{(\pi - \theta_0)^2}{2\alpha^2}\right), & (\frac{\pi}{2} \leq \theta_0 \leq \pi).
 \end{aligned} \tag{3.93}$$

where  $A$  is the normalization factor,  $\theta_0$  is the angle between the polymer's local tangent and the local nematic director, and  $\alpha$  is the width of the Gaussian distribution. If we experimentally obtain  $\alpha$ , we can obtain the polymer's order parameter as below:

$$\begin{aligned}
 S &= \frac{\int_0^{\frac{\pi}{2}} (\frac{3}{2} \cos^2 \theta_0 - \frac{1}{2}) \exp(-\frac{\theta_0^2}{2\alpha^2}) \sin \theta_0 d\theta_0 + \int_{\frac{\pi}{2}}^{\pi} (\frac{3}{2} \cos^2 \theta_0 - \frac{1}{2}) \exp(-\frac{(\pi-\theta_0)^2}{2\alpha^2}) \sin \theta_0 d\theta_0}{\int_0^{\frac{\pi}{2}} \exp(-\frac{\theta_0^2}{2\alpha^2}) \sin \theta_0 d\theta_0 + \int_{\frac{\pi}{2}}^{\pi} \exp(-\frac{(\pi-\theta_0)^2}{2\alpha^2}) \sin \theta_0 d\theta_0} \\
 &= \frac{\int_0^{\frac{\pi}{2}} (\frac{3}{2} \cos^2 \theta_0 - \frac{1}{2}) \exp(-\frac{\theta_0^2}{2\alpha^2}) \sin \theta_0 d\theta_0}{\int_0^{\frac{\pi}{2}} \exp(-\frac{\theta_0^2}{2\alpha^2}) \sin \theta_0 d\theta_0}. \tag{3.94}
 \end{aligned}$$

In our experiment, the director is located inside the observation plane. Thus there are two important directions in our system: one is the director and the other one is the one perpendicular to the observation plane. As shown in Fig. 3.7, we define  $z$  axis along the director and  $x$  axis perpendicular to the observation plane. Therefore we have to define two sets of angles: one is  $\theta_0$ , the angle between the polymer and  $z$  axis, and it is the 3D fluctuation angle; the other set is  $(\theta, \phi)$ , the spherical coordinates with  $x$  axis as the azimuthal axis, and  $\phi$  is the measured 2D fluctuation angle.

If we define  $\mathbf{e}_r$  as the unit vector along the polymer direction, we have:

$$\mathbf{e}_r = (\cos \theta, \sin \theta \sin \phi, \sin \theta \cos \phi). \tag{3.95}$$

Since  $\cos \theta_0 = \mathbf{e}_r \cdot \mathbf{z}$ , we have:

$$\cos \theta_0 = \sin \theta \cos \phi. \tag{3.96}$$

When  $\theta_0$ ,  $(\frac{\pi}{2} - \theta)$ , and  $\phi$  are very small, we have:

$$\theta_0^2 = (\frac{\pi}{2} - \theta)^2 + \phi^2. \quad (3.97)$$

Thus  $\theta_0$ ,  $\theta$ , and  $\phi$  share the same distribution function. Experimentally we measured the 2D angle  $\phi$ 's orientational distribution function, and found it was a Gaussian distribution with width  $\alpha$ . Therefore the 3D angle  $\theta_0$ 's orientational distribution function is also a Gaussian distribution with width  $\alpha$ . Since we know  $\theta_0$ 's orientation distribution function, we can easily obtain the polymer's order parameter:

$$\begin{aligned} S &= \langle \frac{3}{2} \cos^2 \theta_0 - \frac{1}{2} \rangle = \langle 1 - \frac{3}{2} \theta_0^2 \rangle \\ &= \langle 1 - 3\phi^2 \rangle = \frac{\int_{-\pi}^{\pi} (1 - 3\phi^2) \exp(-\frac{\phi^2}{2\alpha^2}) d\phi}{\int_{-\pi}^{\pi} \exp(-\frac{\phi^2}{2\alpha^2}) d\phi}. \end{aligned} \quad (3.98)$$

Here we used the symmetry:  $(\frac{\pi}{2} - \theta)^2 = \phi^2$ .



## **Chapter 4**

# **Colloidal Particle Synthesis**

### **4.1 Introduction**

Solid particles are often encountered in everyday life. They are major components of common materials, e.g., paints and inks. They are widely found in industrial processing, e.g., drug precipitation, oil-drilling, and food processing. They are also ubiquitous as objects of research and application in soft condensed matter physics, in chemical engineering, and increasingly in biology and medical science. In our lab we have traditionally obtained particles from commercial companies. However, experimental demands for improved stabilization of particles in a variety of solvents, improved polydispersity, improved index of refraction mismatch between particle and solvent, and unusual particle shapes for novel self-assembly, have led us to develop the capability to synthesize and stabilize particle suspensions at PENN.

Table 4.1: Physical Properties of Commonly and Uncommonly Used Particles

	PMMA	PS	SiO <sub>2</sub>	ZnS
density (gm/cc)	1.2	1.05	2.1	4.1
refractive index	1.49	1.59	1.45	2.38

In this chapter, we discuss some colloidal particle synthesis schemes we have put into place at PENN. In §4.2, we cover two basic synthesis methods: emulsion polymerization and sol-gel processing. In §4.2.1, we focus on emulsifier free emulsion polymerization of PMMA (poly(methyl methacrylate)) particles. In §4.2.2 and §4.2.3, we describe how to synthesize silica and ZnS particles with the sol-gel method. Finally, we demonstrate how to obtain non-spherical particles by mechanically stretching spherical PMMA or PS (polystyrene) particles (§4.2.4). In some cases these procedures are closely adapted from existing literature; in other cases we have developed new methods for creation of particles. These latter developments are worthy of publication in their own right.

## 4.2 Colloidal Particle synthesis

Generally there are two major methods to synthesize common colloidal particles. One method is emulsion polymerization, which is usually applied to make organic particles, and the other method one is the sol-gel process, which is usually applied to make inorganic particles. In Table 4.1, the physical properties of some common and uncommon colloidal particles are given.

### 4.2.1 PMMA Colloidal Particle Synthesis

Emulsion polymerization is a widely used process for the production of synthetic latexes. It was first introduced on an industrial scale in the mid-1930s. Today, millions of tons of synthetic polymer latexes are prepared by the emulsion polymerization process for use as commodity polymers in a wide variety of applications such as: synthetic rubber, high-impact polymers, latex foam, latex paints, paper coatings, carpet backing, adhesive, binders for non-woven fabrics, barrier coatings additives for construction materials such as Portland cement, mortar and concrete, and sealants. Emulsion polymerization is a free-radical-initiated chain polymerization in which a monomer or a mixture of monomers is polymerized in the presence of an aqueous solution of a surfactant to form a product, known as a latex. Latex is defined as a colloidal dispersion of polymer particles in an aqueous medium.

In 1927 people started to use emulsifiers and peroxide initiators to polymerize butadiene into a latex. Harkins and his coworkers brought up the first model for emulsion polymerization [22]. In their model, they found four indispensable ingredients for emulsion polymerization: a water soluble initiator, an emulsifier, a monomer that is only slightly soluble in water, and water. The emulsifier is an amphiphilic molecule; it enables one to mix organic molecules into water. It is also called a surfactant. Because these molecules have hydrophilic and hydrophobic parts, they self-assemble into spherical aggregates in water when their concentration is above a certain value called the critical micelle concentration (CMC). This spherical structure is called a micelle. When there is monomer

present in the solvent, the monomer penetrates into the micelle cores, since the inner cores of the micelles are hydrophobic. Another way to understand this phenomenon is that the surfactant prefers to stay at the interface between monomer and water in order to decrease monomer droplets' surface tension in suspension. Consequently, surfactant will decrease the monomer droplet size and increase the monomer droplet total surface area. Besides stabilizing monomers in droplets, the surfactant can also stabilize the final product latex particles. This is because the surfactant's hydrophobic part sticks to the particle surface, and the hydrophilic part, which usually has a charged ionic group, electrostatically prevents latex particle aggregation.

The general free radical polymerization has four major reaction stages: initiation, propagation, termination and transfer.

Initiation:



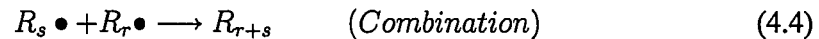
where  $I_2$  represents initiator, M represents monomer, and  $\bullet$  represents a unpaired electron.

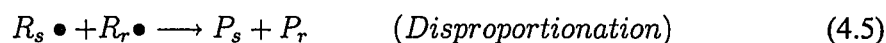
Propagation:



where  $R_r\bullet$  is free radical composed of  $r$  monomers.

Termination:





where  $P_r$  or  $P_s$  are polymer molecules with a terminal double bond.

Chain transfer:



where T is the chain transfer agent. The initiation stage involves creation of free-radical active center and usually takes place in two steps. The first step is the formation of free radicals from the initiator, and the second step is the addition of one of these free radicals to a molecule of monomer. The propagation stage involves growth of the polymer chain by rapid sequential addition of monomer molecules to the active center. In the stage of termination, growth of the polymer chain is terminated. Combination and disproportionation are the two most common termination reactions; both involve reactions between two growing polymer chains. Combination involves the coupling together of two growing chains to form a single polymer molecule; disproportionation involves a hydrogen atom's abstracting from one growing chain to another, and two polymer molecules being formed, one with a saturated end group and the other with an unsaturated end group. Besides combination and disproportionation, there are a number of other reactions which terminate the growth of a chain radical. These reactions are collectively defined as chain transfer reactions. All molecular species present in a free-radical polymerization are potential sources of chain transfer.

As noted before, monomer, surfactant, initiator and water are four primary components

for emulsion polymerization. The monomer is often an unsaturated organic molecule. For surfactant, NaDDBS (sodium dodecylbenzene sulfonate) is commonly used because of its low price. Initiators are usually thermal- or photo- activated molecules.  $\text{Na}_2\text{PS}$  (sodium persulfate) and  $(\text{NH}_4)_2\text{PS}$  (ammonium persulfate) are commonly used initiators in aqueous phase polymerization. After decomposition, the persulfate group of the initiator will be split into two identical, ionic  $-\text{SO}_4^-$  groups. Since most monomers are not charged themselves, the charge of the final particles' surface comes solely from the initiators. This offers us a possibility to modify the type and strength of a particle's surface charge by choosing different initiators. We will describe this in detail later.

For emulsion polymerization, the monomer is emulsified in water, and an emulsion is formed. There are three phases in the emulsion system: the aqueous phase, the monomer droplet phase, and the monomer swollen micelle phase. Correspondingly, there are three kinds of nucleation mechanisms. One is *homogeneous nucleation*, referring to polymerization happening in the aqueous phase, wherein dissolved monomer molecules and dissolved initiator molecules meet each other and react. *Droplet nucleation* refers to polymerization at monomer droplet surfaces. *Micelle nucleation* refers to polymerization inside monomer swollen micelles. For a slightly water soluble monomer (like styrene), homogeneous nucleation can be ignored. If the monomer is emulsified well in water, droplet nucleation can also be ignored. The reason is as follows: swollen micelle size is of order 10 nm, while the monomer droplet size is of order 10 micron, thus the micelle would have 6 orders of magnitude higher available surface area for reaction than the monomer droplet.

Since there is only one nucleation mechanism working here, the final particle size should be highly monodispersed as long as everything in the solution is kept uniform.

Sometimes monomers, such as MMA (methyl methacrylate), have reasonable solubility in water. In this case homogeneous nucleation becomes a significant nucleation mechanism. In our lab, we have use a method of *surfactant free emulsion polymerization* to synthesize monodispersed submicron and micron sized PMMA particles. With this method we synthesized highly monodispersed particles with size range from 250 nm to 1.5  $\mu\text{m}$ . For particle sizes smaller than 250 nm, we used the conventional emulsion polymerization method.

For both surfactant free emulsion polymerization and emulsion polymerization, there are two methods of reaction: one is the batch method, the other is the semi-batch method. For the batch method, the monomer is fed once into water and allowed to react. In this case, we generally make 250 nm seed particle with surfactant free emulsion polymerization. For the semi-batch method, we use small particles as seeds, and then feed the monomer to the solution to help the seeds to grow to bigger particles. In the remaining of this subsection, we first describe how we use batch method of surfactant free emulsion polymerization to prepare  $\sim 250$  nm PMMA seed particles; then we describe how we use  $\sim 250$  nm particles as seeds, and then use a semi-batch method of surfactant free emulsion polymerization to grow bigger particles; lastly, we describe how we prepare particles smaller than 250 nm by emulsion polymerization.

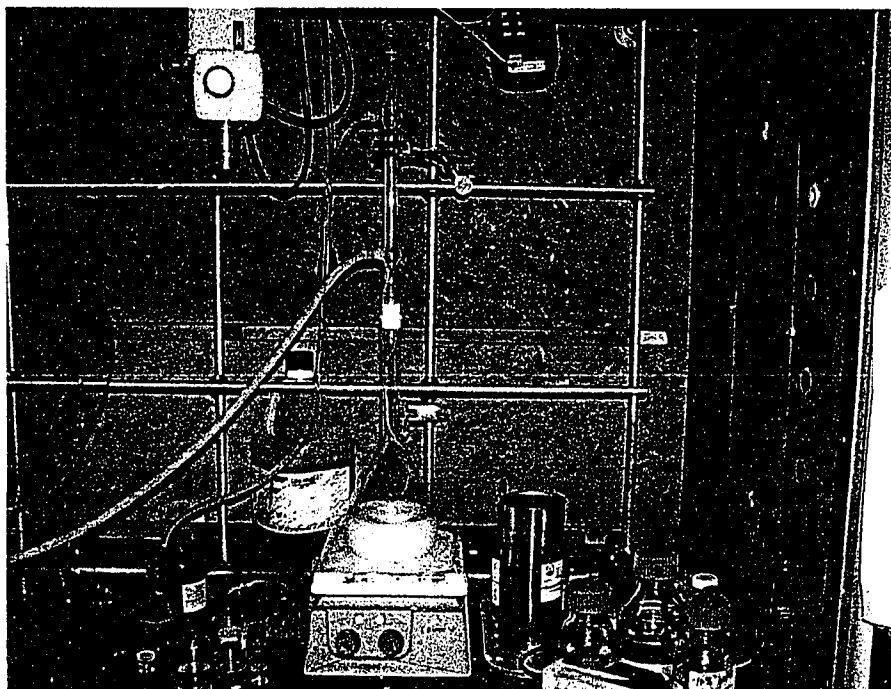


Figure 4.1: Sketch of the experiment setup of our surfactant free emulsion polymerization of PMMA particles. The milky solution is the PMMA colloidal dispersion in reaction.

### Synthesis of 250 nm Seeds

The setup we used during synthesis is composed of a ceramic-top stirring hotplate (from Fisher Scientific), a 1000 mL flask, a water cooling condenser, a thermal couple temperature meter, and a magnetic stirrer bar. The assembled setup is as showed in Fig. 4.1.

For  $\sim 250$  nm seed particles, the recipe ingredients are shown in Table 4.2. We add 2% MMA to water, heat it to around  $85^{\circ}\text{C}$ , hold it for 5 minutes, and then add initiator  $\text{Na}_2\text{PS}$  (0.1 wt% based on the monomer) to the solution. The whole solution is under mild agitation all the time. After about 20 minutes, we notice the solution's color changes from transparent to weakly blue, and then to uniformly milky white. After the solution turns milky white, we maintain the reaction for 20 more minutes to ensure completeness of the



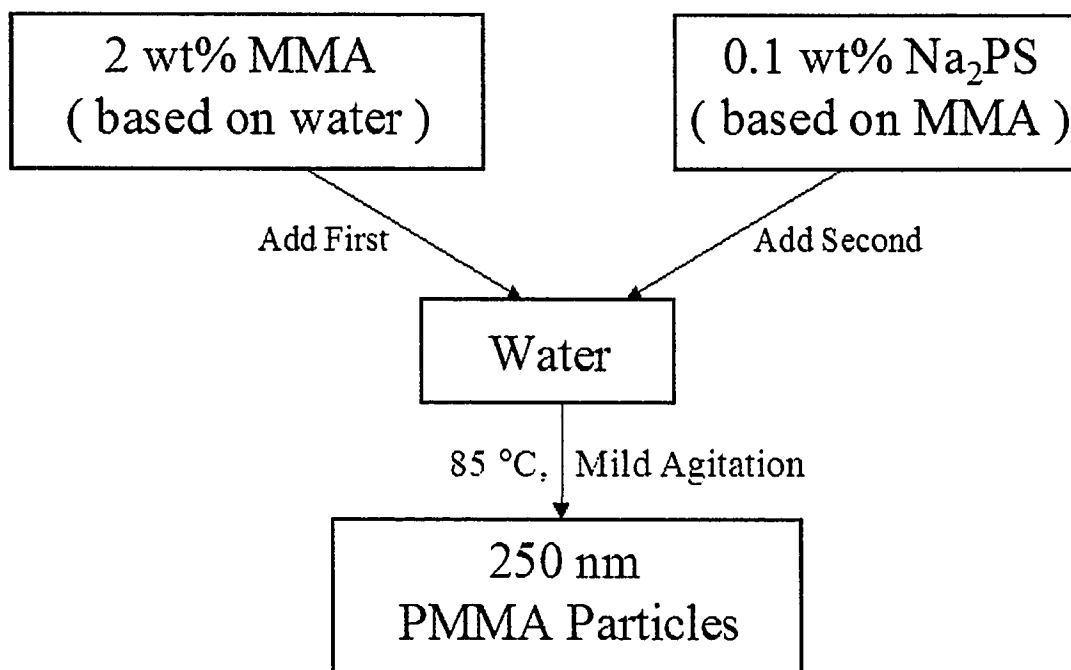


Figure 4.2: Flow chart of the synthesis of 250 nm PMMA particles.

reaction. The full reaction scheme is shown in the flow chart in Fig. 4.2. All chemicals used are from Sigma-Aldrich. They are used as received, without further purification. The water is deionized ultra-filtered water. We choose 85°C as our reaction temperature for two reasons: one, because initiators decompose with a proper speed at this temperature, and two, because it is close to PMMA polymer's glass transition temperature (95 °C), and monomers can easily penetrate and swell the existing nucleates without nucleating new particles. This helps to improve the final product monodispersity by preventing second nucleation of new particles. Dynamic Light Scattering (DLS) measurements indicate that the final product size is 248 nm with polydispersity 3.2%.

The high monodispersity of the final dispersion requires that homogeneous nucleation

Table 4.2: Recipe of the Synthesis of PMMA 250 nm Seed Particles

material	water	MMA	$Na_2PS$
Amount	500 cc	10 gm	10 mg

is the only nucleation mechanism. As long as the solution is kept uniform by mild agitation, the final product should have mono-size distribution. The disadvantage of this method is that since we add monomer once, the final particle size is more or less fixed. No matter how much monomer you added to water (e.g. from 1% to 8%), the final particle size is always around 250 nm. We speculate that this size is probably determined by the surface tension between PMMA and water. More monomer means more particles.

### Synthesis of Particles above 250 nm

In order to achieve larger particles, we turned to the semi-batch method. We add small size PMMA particles as seeds, and then feed the monomer to the solution to help the seeds to grow to the desired size. There exist two nucleation mechanisms in this process: one is heterogeneous nucleation (which is desired), wherein the feeding monomer swells the existing seed particles and polymerizes; the other is homogeneous nucleation (which is what we try to avoid), wherein the feeding monomers polymerize in aqueous phase and generate new particles instead of helping existing particles to grow. In order to prevent homogeneous nucleation, we add a cosolvent (n-Butanol) to our system. n-Butanol has two functions: it decreases MMA's solubility in water to prevent homogeneous nucleation,

Table 4.3: Recipe of the Synthesis of 420 nm PMMA Particles

material	water	seed	Butanol	MMA	$Na_2PS$
Amount	220 cc	31.25 cc	5 cc	5 gm	5 mg

\*Seed is composed of 2 % 248 nm particle suspension.

and it makes the existing PMMA particles soft, so it is easier for the feeded monomers to swell the existing particles.

Our recipe of the semi-batch synthesis is very simple. For example, we already have 248 nm seed particles. Suppose we want to make  $\sim 420$  nm particles. As shown in Table 4.3, we add 31.25 cc 2% 248 nm seed solution and 5 cc of Butanol to 220 cc of water. We then heat the solution to 85 °C and hold it at this temperature for 10 minutes. Then we add 5 mg initiator  $Na_2PS$ . After 5 minutes, we add in 5 cc monomer. We then hold the sample for 30 mins for completeness of the reaction. DLS shows that the final particle size is 412.6 nm with polydispersity within 5%. The scheme is shown in the flow chart in Fig. 4.3. With this method, we can grow sizes even bigger than the 1  $\mu m$  monodispersed PMMA particles. Shown in Fig. 4.4(a) is a bottle of seed particle solution. The particles sediment to the bottom of the bottle and crystallize there. The crystallization can be confirmed by the iridescence. Fig. 4.4(b) shows an optical microscopy of 580 nm size PMMA particles we synthesized. As we can see, those particles are monodispersed enough to form nice triangular surface crystal.

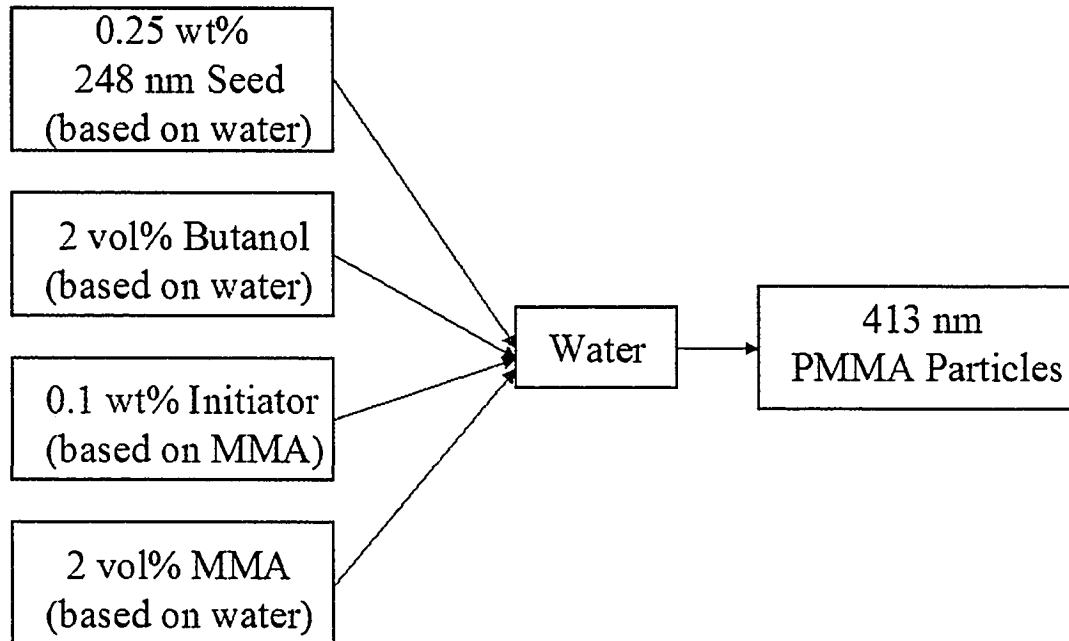


Figure 4.3: Flow Chart of how to use semi-batch method to grow particles with size bigger than 250 nm.

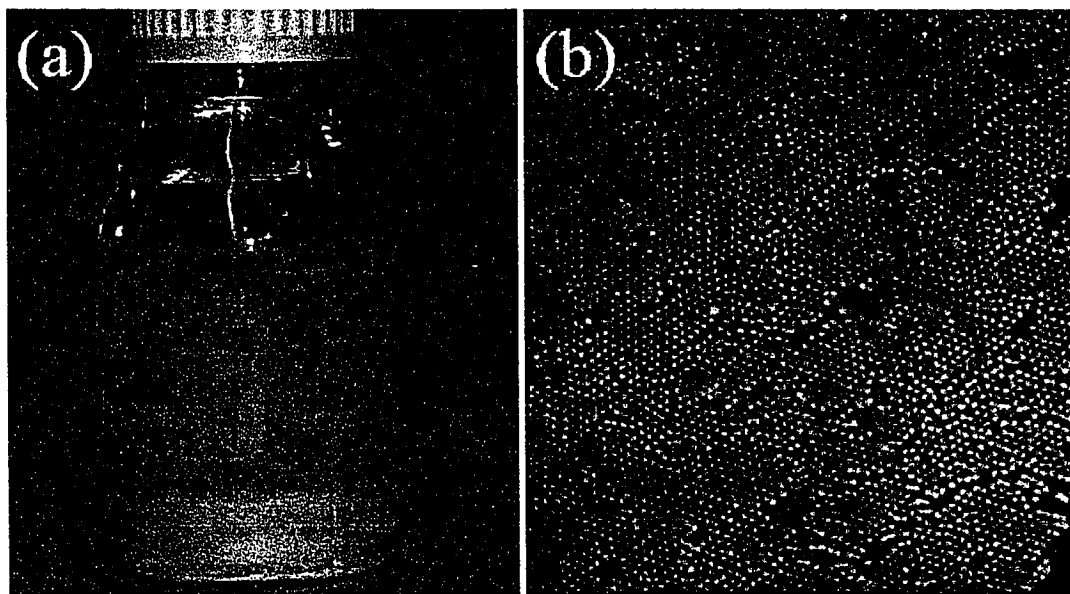


Figure 4.4: (a) A bottle of 248 nm PMMA particles synthesized by us. The particles crystallize at the bottom of the bottle and give iridescent color. (b) Surface crystallization of 580 nm PMMA particles synthesized by us.

### **Synthesis of Particles below 250 nm**

Sometimes our research requires particles smaller than 250 nm. In order to achieve such a small size, we must add surfactant to the system to decrease the surface tension between PMMA particles and water. As we have mentioned, the surfactant will induce polydispersity into the system. Thus, it is really an art to find a recipe that works. Here is an example of the preparation of 70 nm monodispersed PMMA beads, which largely follows US Patent 4427836. As shown in Table. 4.4, the recipe is composed of heel charge, monomer emulsion and initiator solution. The synthesis procedure is: charge the heel to the reactor, heat to 85 °C with stirring. When the heel charge's temperature stabilize at 85 °C, add in 10 gm of monomer emulsion followed by initiator solution. Wait 15 minutes and begin dropwise addition of remaining monomer emulsion at 3 mL/min. After addition is completed, hold 20 minutes more. The whole reaction scheme is shown in the flow chart in Fig. 4.5. DLS shows that the final particle's size is 69.7 nm with 4.0 % polydispersity. For particle sizes between 70 nm and 250 nm, we can use 70 nm particles as seeds, and then use semi-batch method to grow to the desired size.

### **Surface Modification of PMMA Particles**

Our PMMA particles will have a much broader application if we can modify their surface properties. For example, amino, or carboxylic acid surface group can covalently bind biopolymers to the particle surface, and silane surface group will make it possible for us to coat PMMA particles with a silica shell. In our lab, we succeeded in fabricating

Table 4.4: Recipe of the Synthesis of 70 nm PMMA Particles

Materials	Amount
A. Heel Charge	
DI Water	580 cc
NaDDBS	1.1023 gm
B. Monomer Emulsion	
DI Water	53.09 gm
NaDDBS	0.0798 gm
MMA	160.00 gm
MAA	2.15 gm
C. Initiator Solution	
Ammonium Persulfate	0.6077 gm
DI Water	2 cc

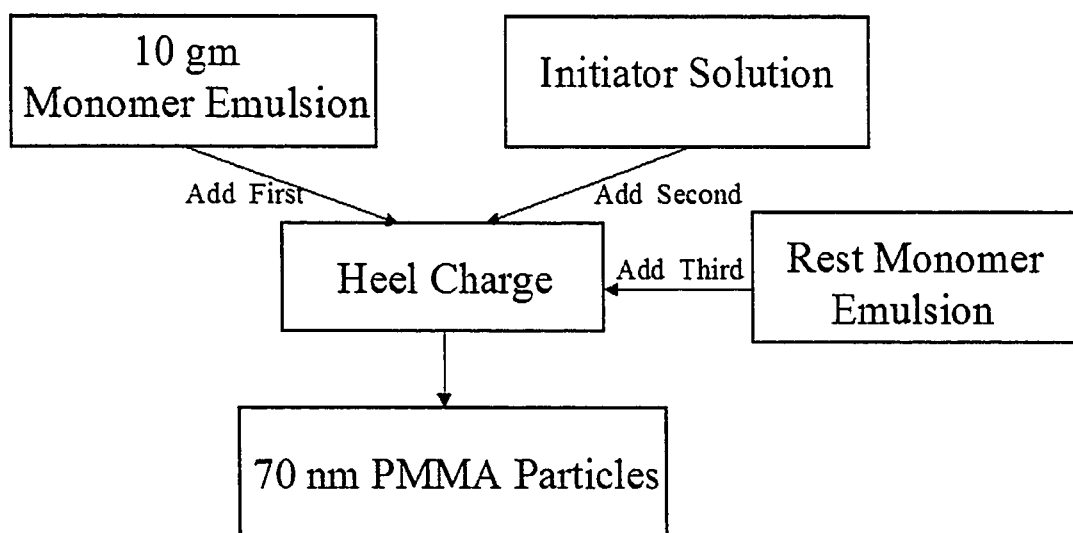


Figure 4.5: Flow Chart of how to synthesize 70 nm PMMA particles.

PMMA beads with amino or carboxylic acid by choosing the right initiators. We can also synthesize silane grouped PMMA particles by adding the right co-monomer to MMA.

For particles with amino or carboxylic acid surface groups, we use *Vazo 56 WSP* (2,2'-Azobis(2-methylpropionamidine) dihydrochloride, from Dupont), or *Vazo 68 WSP* (4,4'-Azobis(4-cyanovaleric acid), from Dupont) as initiator. The recipe for the synthesis with these two new initiators is similar to the above surfactant free emulsion polymerization. But there exist two differences. One, because of the special chemical structure of these two initiators, we are able to add 1 % initiator based on monomer instead of 0.1 %. This large amount of initiator helps to increase the final particle surface charge density. The second difference is that since the final particles are highly charged, we are able to add salt to the reacting solution. For example, when we use *Vazo 56 WSP* as initiator, we can add as much as 100 mM NaCl without destabilizing the colloid suspension. This high ionic strength tends to decrease the particles' surface tension. So we can achieve ~400 nm seed particles with the batch method. The reaction scheme is as shown in the flow chart in Fig. 4.6. Fig. 4.7 is a SEM picture of carboxyl modified PMMA beads we synthesized. The bead size is ~350nm, and they are sufficiently monodisperse to form a crystal. For particles with silane surface group, we add 10 % 3-(trimethoxysilyl)propyl methacrylate to the MMA as comonomer. The rest recipe is the same as pure PMMA particles.

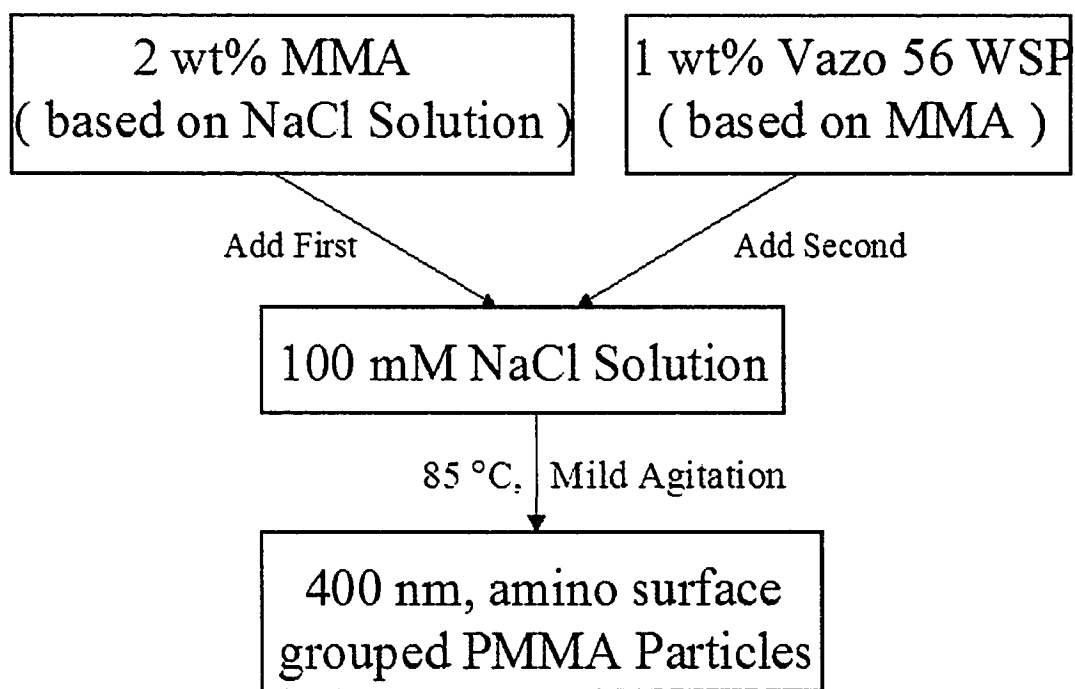


Figure 4.6: Flow Chart of how to synthesize amino surface grouped PMMA particles.

#### Synthesis of Nonaqueous PMMA Particles

Besides synthesizing aqueous PMMA particles, people have succeeded in fabricating monodisperse nonaqueous PMMA particles. Those particles are stabilized by poly(12-hydroxy stearic acid) graft copolymer stabilizer (PHSA). The interaction between those sterically stabilized PMMA particles is close to hard-sphere. What's more, people fluorescently label those particles. Thus, they are model particles to study the colloidal crystallization and interaction.

Here is a straightforward recipe to synthesize fluorescent labelled, monodispersed, nonaqueous PMMA particles [23]: 0.27 g of  $\alpha, \alpha'$  azo-bis-isobutyronitrile (from Acros), 8.3 mg of the dye 1,1'-dioctadecyl-3,3,3',3'-tetramethylindocarbocyanine perchlorate (DiIC<sub>18</sub>,





Figure 4.7: SEM picture of  $\sim 300$  nm PMMA particles we synthesized.

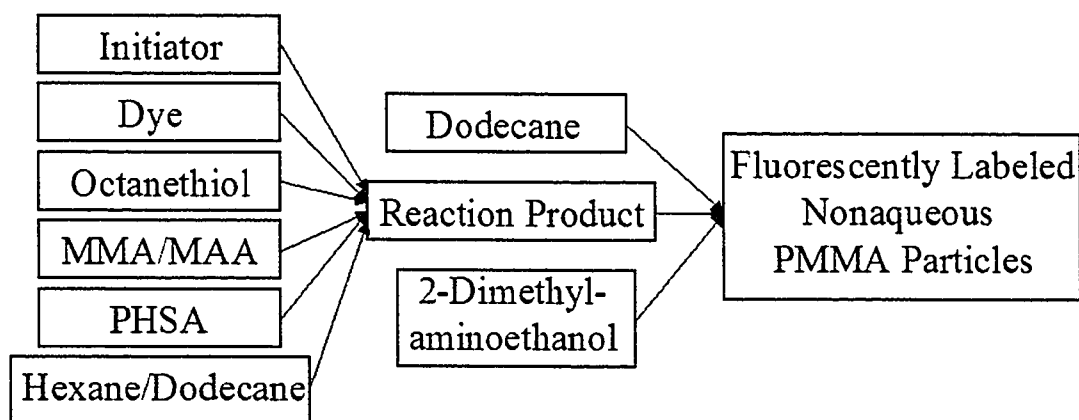


Figure 4.8: Flow Chart of how to synthesize fluorescently labelled, nonaqueous PMMA particles.

from Fluka), and 0.18 g of octanethiol (from Aldrich) are dissolved at room temperature in a mixture of 34.4 g MMA (from Aldrich) and 0.71 gm methacrylic acid (MAA, from Aldrich) in a 250 mL round-bottomed flask equipped with a reflux condenser. A solution of 1.76 g of PHSA (synthesized according to [24]), 15.8 gm hexane and 7.9 g dodecane are added and the polymerization starts by placing the reaction mixture in an thermostated oil bath at 80°C. The reaction is continued for 2 hours to ensure the completeness of the reaction. This reaction only polymerizes MMA into PMMA particles. But we still need to covalently graft PHSA onto particle surfaces. Thus, add 15.8 gm dodecane and 0.15 gm of 2-dimethylaminoethanol (from Acros) and the mixture refluxed at 120 °C for a further 24 hours. After the reaction is complete, dilute the solution with dodecane and then filter through glass wool to remove coagulum. Then do centrifuge/exchange solvent with clean dodecane several times to ensure the final solution is clean. The whole process is as shown in the flow chart in Fig. 4.8.

### **4.2.2 Silica Colloidal Particle Synthesis**

Monodispersed inorganic particles have found many applications of technological interest in ceramics, pigments, and catalysis. Most inorganic colloidal particles are prepared by a solution sol-gel (SSG) process. For sol-gel method, the synthesis always starts with a homogeneous precursor solution. When the solute's concentration passes a critical concentration, the primary particles precipitate out of the solution. Those primary particle size is always below 50 nm and they are not stable in water. They start sticking to each other to form bigger particles. Eventually, sub-micron or micron sized colloidal particles are generated. For example, micron sized silica particles are composed of 3 nm nucleates, and ZnS particles are composed of 15 nm nucleates. The keys for producing monodispersed inorganic particles are: the reaction solution should be kept uniform all the time, the reaction speed should be under control so that the aggregation of the primary nucleates does not happen too quickly nor too slowly, and there should be an effective stabilizer to prevent the particles from aggregation during the synthesis.

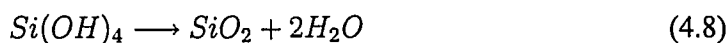
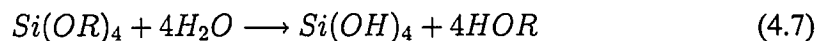
#### **Synthesis of Plain Silica Particles**

Silica is an example of one of the earliest monodispersed inorganic particle successfully synthesized. Before researchers used nonaqueous core-shell PMMA particles as model particles, researchers used monodispersed silica particles as model particles to study particle interaction and crystallization. The pioneering work on silica colloidal particle synthesis was done by Stöber and his coworkers [25]. The scheme of their method is hydrolyzing

Table 4.5: Recipe of the Synthesis of Monodispersed Silica Particles

	Material	Amount
Solution 1	IPA	200 mL
	H <sub>2</sub> O	14 mL
	TEOS	23.50 gm
Solution 2	NH <sub>3</sub> · H <sub>2</sub> O	36 mL

tetraethyl orthosilicate (TEOS) in an alcohol medium in the presence of water and ammonia:



Our experiment largely follows the *Stöber method*. We get TEOS from Fluka, ethanol, isopropyl alcohol from Aldrich Sigma, and ammonium hydroxide (28.82 wt%) from Fisher Scientific. One example of the recipe is shown in Table 4.5 and in the flow chart in Fig. 4.10. We prepare Solution 1 in an Erlenmeyer flask, and there is a magnetic stirrer bar in it. We put the flask in an oven at 40 °C. We also put a magnetic stirrer in the oven to agitate solution1. After that, we prepare Solution 2 in another Erlenmeyer flask and put it into the oven. It will take about 20 minutes for the solutions' temperature to reach equilibrium. We then add Solution 2 to Solution 1 and keep mild agitating the mixed solution. After about one hour, the solution becomes milky white, which is an indication of colloidal particles produced. We take the flask out and do centrifuge/exchange water/redisperse cleaning process at least 3 times to get rid of excess TEOS, ammonium and alcohol. Fig.

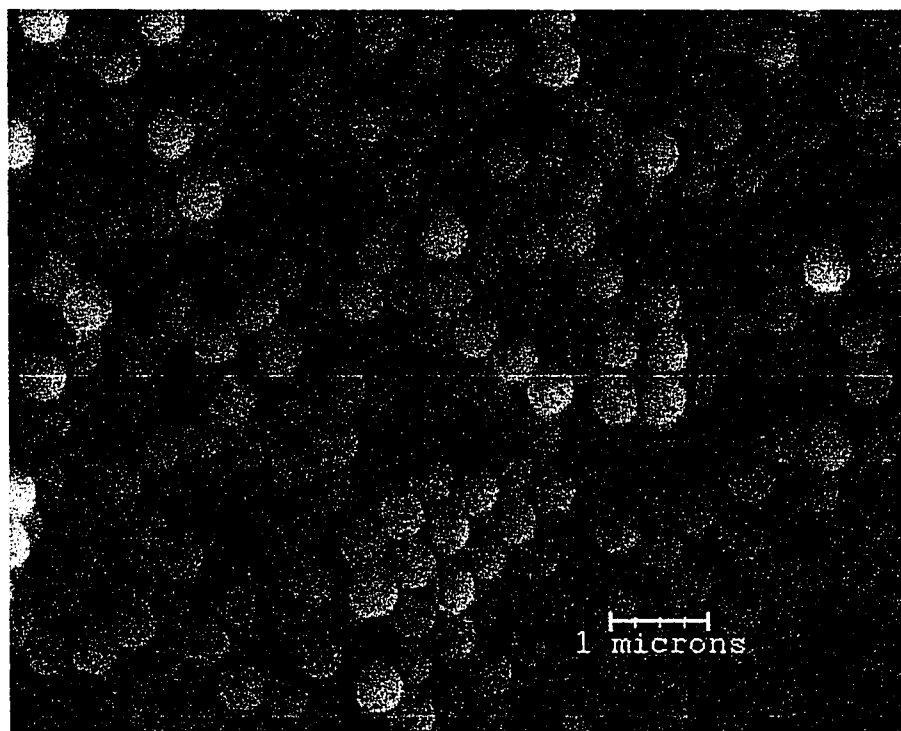


Figure 4.9: SEM picture of  $\sim 500$  nm silica particles we synthesized.

4.9 is a SEM picture of the silica beads we made. Their size is 500 nm, and they are fairly monodisperse. Their sedimentation gives iridescent color.

We can vary the final particle size by changing the ratio of each reactant. By this method we can achieve particles with size below  $0.8 \mu\text{m}$ . For particle size bigger than  $0.8 \mu\text{m}$ , we have to use small silica beads as seeds, and then grow bigger beads out of the seeds. There is a general recipe as shown in Table. 4.6.

### Synthesis of Fluorecently Labelled Particles

Scientists have found a way to synthesize fluorescently label silica particles [30]. The dye can be either fluorescein isothiocyanate (FITS, isomer I, sigma), or rhodamine B

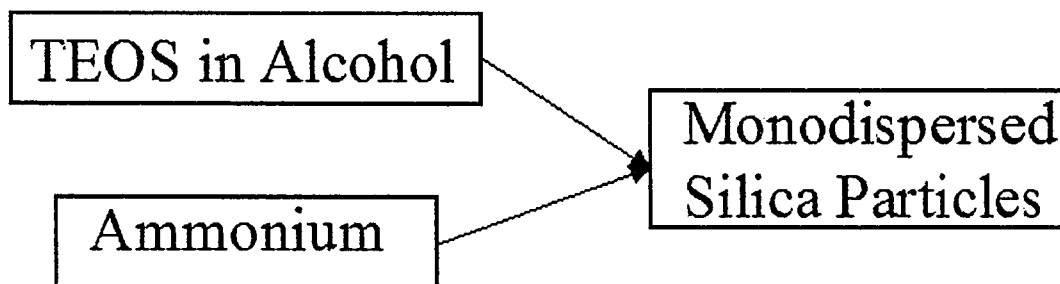


Figure 4.10: Flow Chart of how to synthesize monodispersed silica particles.

Particle diameter ( $\mu\text{m}$ )	0.22	0.32	0.46	0.68	0.78	1.0 <sup>a</sup>	1.2 <sup>a</sup>
TEOS ( $\text{mol dm}^{-3}$ )	0.20	0.25	0.30	0.35	0.45	0.45+0.45	0.5+0.5
$\text{NH}_3$ ( $\text{mol dm}^{-3}$ )	0.79	0.90	1.13	1.16	1.16	2.0	2.0
$\text{H}_2\text{O}$ ( $\text{mol dm}^{-3}$ )	14.4	8.0	6.4	3.1	3.1	5.0	5.0
Alcohol ( $\text{cm}^3$ )	330 <sup>b</sup>	383 <sup>b</sup>	390 <sup>c</sup>	410 <sup>c</sup>	400 <sup>c</sup>	130 <sup>c</sup>	120 <sup>c</sup>
Total volume ( $\text{cm}^3$ )	500	500	500	500	500	200	200

Table 4.6: Particle Diameter ( $\mu\text{m}$ ) of Silica Obtained by Aging at 40 °C for 1 h Solutions of Reactants at Given Concentrations ( $\text{mol dm}^{-3}$ ) and Volumes ( $\text{cm}^3$ ). <sup>a</sup>Indicates a two-step addition of TEOS, as described in the text. <sup>b</sup>Ethanol. <sup>c</sup>Isopropanol.

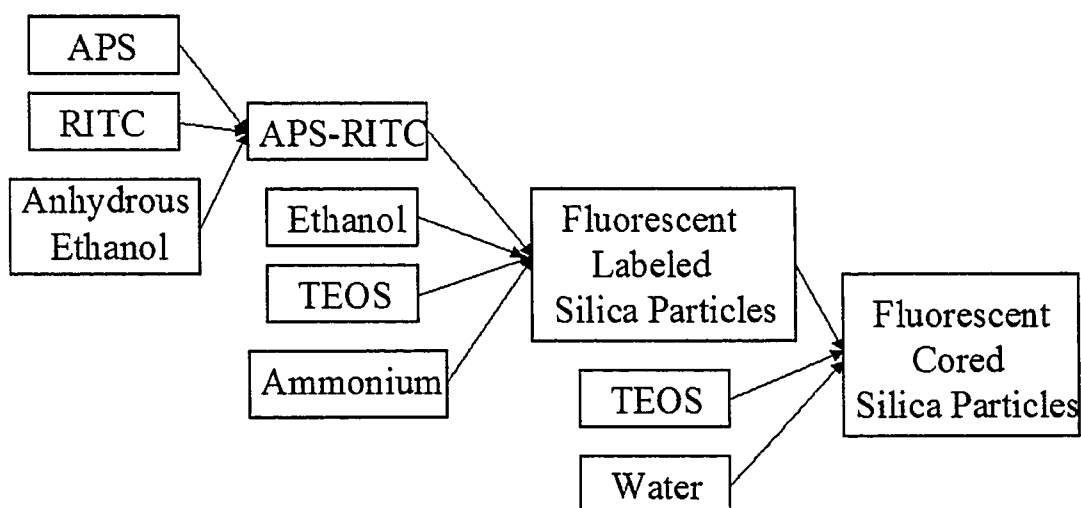


Figure 4.11: Flow Chart of how to synthesize fluorescently labelled silica particles.

isothiocyanate (RITC mixed isomers, Fluka). The methods for these two dyes are similar. The scheme of the synthesis is based on the fact that (3-aminopropyl) triethoxysilane (APS) can couple with both dye molecules and silica beads. The synthesis is divided into 3 steps. The first step is to couple APS to the dye RITC: add 0.0938 g APS to 0.1178 g RITC in a medium of 10 cc anhydrous ethanol. The reaction proceeds for 17 h in the dark under magnetic stirring. The second step is to transfer the coupled APS-RITC solution to a mixture of 670 cc ethanol and 51 cc of ammonia (final concentration, 1M  $\text{NH}_3$  and 2.8 M  $\text{H}_2\text{O}$ ). Then add reagent 28.3 mL TEOS to the solution and hold the reaction for 5.5 h under mild magnetic stirring. Up to now, we succeeded in making fluorescent labelled 100 nm particles. The third step is to coat more silica around the fluorescent core: add only 0.7 cc TEOS to the solution first to prevent flocculation by increasing the ionic strength too much. After that, a total amount of 253 cc of TEOS is added in larger portions with intervals at least 2h. Water is regularly added as well, to maintain the molar ratio water:TEOS at least 10:1. The final particle's size should be around 200 nm. The whole synthesis process is as shown in the flow chart in Fig. 4.11.

### **4.2.3 ZnS Particle Synthesis**

ZnS has attractive applications in many fields such as light-emitting diodes (LED), electrochromic devices, infrared window materials and phosphors for cathode ray tubes [26, 27, 28]. With the emergence of the theory of PBG materials, some people find ZnS particle to be an ideal building block for PBG material because of its high refractive index

(2.38). However, it's a challenging task to synthesize monodispersed ZnS particles for further crystallization. In our lab, we succeeded in synthesizing monodispersed, submicron sized ZnS particles, which can be used for PBG application.

The basic reaction of ZnS synthesis is:



In our experiment,  $Zn^{2+}$  is supplied by Zinc Acetate dihydrate, and  $S^{2-}$  is supplied by the hydrolysis of TAA (thioacetamide).



Reaction speed is crucial for the final product's quality because too quick a reaction speed will result in gelation of the final product and too slow a reaction speed will result in polydispersity of final particle size distribution. We control the reaction speed by controlling the TAA's hydrolysis speed. TAA's hydrolysis speed is related to the solvent's pH value. We find that the optimum pH value is 8.6. In order to increase the reaction's yield, we use concentrated Zinc Acetate solution. We also add EDTA (ethylenediaminetetraacetic acid, disodium salt dihydrate) to the solution to keep the free Zinc ions' concentration constant. Besides controlling the reaction speed, final particle stability is an important factor to achieve monodispersed ZnS colloidal suspension. It is especially important for ZnS because ZnS and water's refractive indexes mismatches a lot, which results in a



strong van der Waals attraction among ZnS particles. In our experiment, we use gelatin as stabilizer and it works well [29]. All the reactants we used are from Sigma-Aldrich.

The recipe we used is shown in Table. 4.7. The procedure is shown in the flow chart in Fig. 4.12. We prepare a mixture composed of 20 cc water, 1.317 gm Zinc Acetate dihydrate, 2.256 gm EDTA, 3.083 gm ammonium acetate, and 0.2 gm gelatin. We denote this mixture as solution 1. We prepare solution 1 in a 40 cc glass vial and put a magnetic stirrer bar in the vial too. Then we adjust solution 1's pH value to 8.6 by adding ammonium hydroxide to solution 1. After that we mild agitate solution 1 and keep it in an oven. The oven's temperature is set at 60 °C. We then prepare solution 2 in a 10 cc glass vial and also put it into the oven. Solution 2 is composed of 5 cc water and 0.45 gm TAA. TAA does not dissolve in water at room temperature, but it will quickly dissolve in water at 60 °C. Wait couple of minutes until the TAA totally dissolve in solution 2, and then add solution 2 to solution 1. Hold the reaction for at least 4 hours. After holding, do centrifuge/exchange water/redisperse cleaning cycle at least 5 times. The resultant ZnS particles are as shown in Fig. 4.13. From the figure, we can see those particles even form hexagonal crystal, which is a proof that they are quite monodispersed.

Because TAA's concentration will affect the reaction's speed and usually the reaction speed will affect the final particle's size, we can vary the particle's size by varying the TAA's amount we add. Table 4.8 is a summary of our experiments.

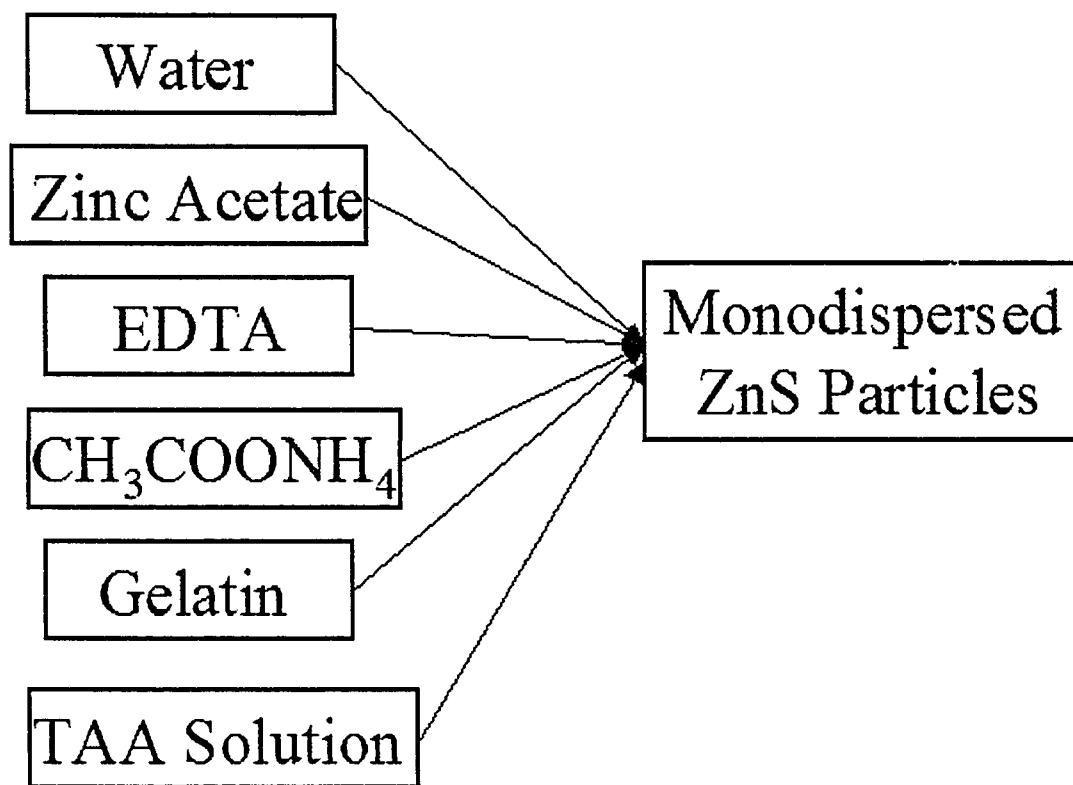


Figure 4.12: Flowchart of how to synthesize monodispersed ZnS particles.

Table 4.7: Recipe of the Synthesis of Monodispersed ZnS Particles

	Material	Amount
Solution1	H <sub>2</sub> O	20 mL
	Zn(CH <sub>3</sub> CO <sub>2</sub> ) <sub>2</sub> · 2H <sub>2</sub> O	1.317 gm
	EDTA	2.256 gm
	CH <sub>3</sub> COONH <sub>4</sub>	3.083 gm
	gelatin	0.2 gm
Solution2	H <sub>2</sub> O	5 mL
	TAA	0.45 gm

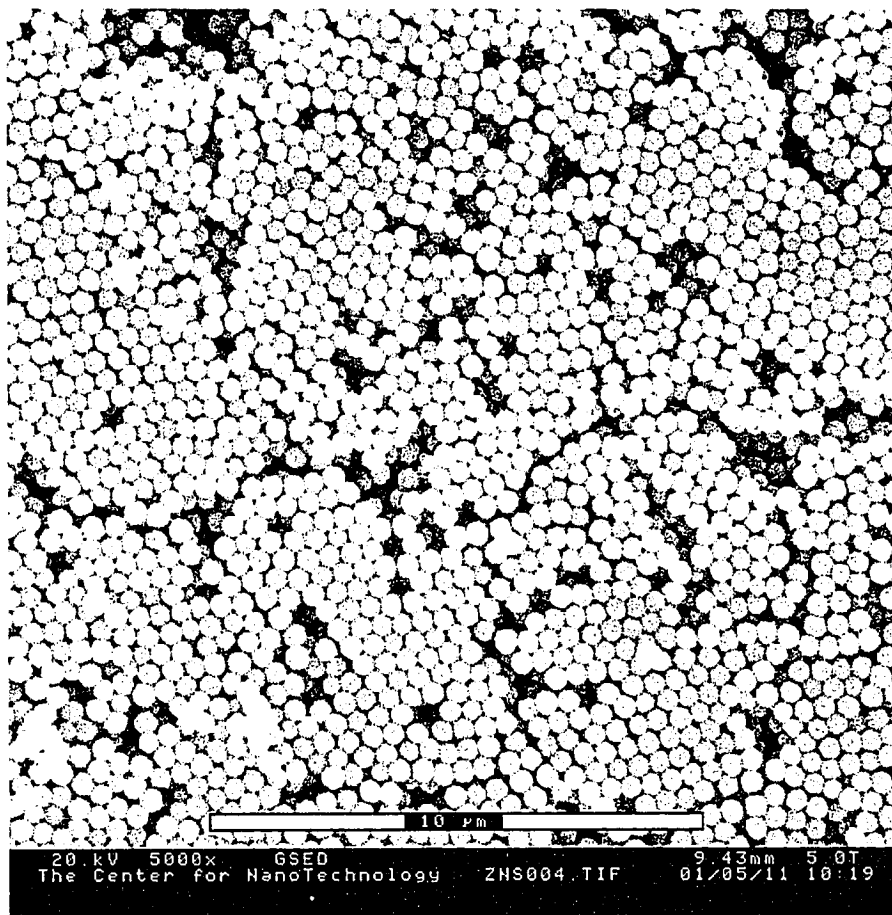


Figure 4.13: SEM picture of  $\sim 500$  nm ZnS particles we synthesized.

Table 4.8: Particle Size Dependence on TAA Concentration.

Series	TAA (gm)	Size (nm)	Size Distribution (%)
1	0.50	360.1	5.36
2	0.35	484.3	4.45
3	0.36	521.0	2.29

## 4.2.4 Synthesis of Ellipsoid Particles

### Introduction

Up to now, all we have discussed is how to synthesize spherical particles. From researchers point of view, a non-spherical colloidal dispersion will sometimes be much more exciting because they present richer phase behavior than spherical colloidal dispersions due to their anisotropic shape. Researchers have already known that hard rod-like dispersions will exhibit isotropic, nematic and smectic phases with an increase of particle concentration. There are still a lot of unknowns about this system, for example, in a 2D system, whether the isotropic-nematic phase transition is first or second order. Because of the special size range of colloidal particles, people can directly visualize their motion with the optical microscope. Thus, an ellipsoid colloidal dispersion will offer a powerful tool for the physicist to explore some open areas. There has been some success in making monodispersed ellipsoid inorganic particles [31]. Because of their high density and high refractive index, they are difficult to observe by optical microscopy. For organic particles, the situation is not as good. It is possible to synthesize monodispersed ellipsoid particles by mechanically stretching monodispersed spherical particles. The pioneering stretching work was done by Ottewill and coworkers [32], and later Xia and coworkers made some improvements [33]. The basic scheme of their methods is imbedding organic (PS or PMMA) particles into a matrix of another polymer PVA (poly(vinyl alcohol)). Since PVA's glass transition temperature ( $\sim 180^\circ\text{C}$ ) is much higher than PMMA or PS's glass transition temperature ( $\sim 105^\circ\text{C}$ ), they could easily deform the imbedded particles by

stretching the PVA film at  $\sim 200^{\circ}\text{C}$  in an oil bath. They used isopropanol-water mixture (3:7 v/v) to dissolve the PVA matrix, and then tried to redisperse the stretched particles in water. They found only small fraction of the stretched particles can be redispersed, and most of the stretched particles aggregated. In general, the yield is too low to do any realistic study on the ellipsoid particles' phase behavior.

In order to improve the yield, we made three modifications. We chose the right PVA, we stretched it at  $135^{\circ}\text{C}$  in an oven instead of at  $200^{\circ}\text{C}$  in oil bath, and we used pure water to dissolve the PVA matrix instead of using a mixture of isopropanol-water. Our results are exciting: we nearly redispersed all the particles we stretched, thus our yield is close to 100%. Also, we stretched the particles as large as 7 times, which corresponds to a particle size ratio  $\sim 20$ .

## **Experimental**

### **Materials**

We used distilled ultra-filtered water. The PVA used is ordered from Sigma-Aldrich. Their molecular weight varies from 13k to 186k, and their hydrolysis ratio varies from 87% to 99+%. They are used as received. The spherical polystyrene beads are ordered from Bangs Labs, and the PMMA beads are homemade particles.

### **PVA Film Formation**

The optimum PVA's molecular weight is 85k-146k, and its hydrolysis ratio is 87-89%. 10 wt% PVA is added to hot water. With gentle stirring, the PVA slowly dissolves into hot water. Then we sonicate the PVA solution to get rid of air bubbles. After that, we add high concentrated PS or PMMA particle solution into PVA solution. The particle concentration based on PVA is from 1 to 5 %. We gently stir the solution during the adding process. Care should be taken to prevent air bubbles. Finally, we pour the particle/PVA solution into a flat bottomed tray and put the tray in a hood. After one night, a uniform, particle imbedded, PVA film is formed.

### **Stretching of Films**

In our lab, we bind two ends of the film to a vice, and then put the vice into an oven. The vice is connected to a motor outside. We set the oven's temperature at  $135^{\circ}\text{C}$ . After the oven's temperature reaches equilibrium, we turn on the motor to stretch the film. Since we already calibrated each turn's stretching distance, we can control how much we stretch the film by controlling how many turns we let the motor turn. Thus, we can control the shape of the final ellipsoid particles.

### **Recovery of the Ellipsoid Particles**

We only kept the center part of the stretched film because only there the stretching field is uniform. We cut the film into small pieces by scissors, and then add them to hot water.

With the agitation from a stirrer bar, the PVA scraps will easily dissolve into water. In order to completely get rid of PVA from the solution, we have to do centrifuge/exchange solvent with DIUF water cycle at least three times.

## Results

We use SEM to characterize our resultant ellipsoidal particles. Fig. 4.14 shows the SEM pictures of the ellipsoid particles we obtained with the stretching technique. Those ellipsoidal particles look reasonably monodisperse. As showed in Fig. 4.14a, the particles are individually dispersed. Fig. 4.14b is a SEM picture of dried remain of a drop of high concentration ellipsoid particles. We can see that those particles form structures similar to nematic ones after drying out.

## Discussion

There exist various types of PVA polymer. We need two parameters to characterize them: one is the hydrolysis ratio, and the other one is the molecular weight. Before we talk about hydrolysis ratio, let's first talk about how PVA is synthesized. In industry, PVA ( $[CH_2CH(OH)]_n$ ) is obtained from hydrolysis of poly(vinyl acetate) ( $[CH_2CH(O_2CCH_3)]_n$ ). The reaction is shown in Equation 4.11. So the hydrolysis ratio is the percentage of how much poly(vinyl acetate) transforms into PVA. From their molecular formula, we can see that poly(vinyl acetate) is a polymer with long side chains, while PVA is a polymer with very short side chains. As a result, poly(vinyl acetate) film's structure is amorphous, and 100% hydrolyzed PVA film's structure is semi-crystalline. Thus, a higher hydrolysis ratio

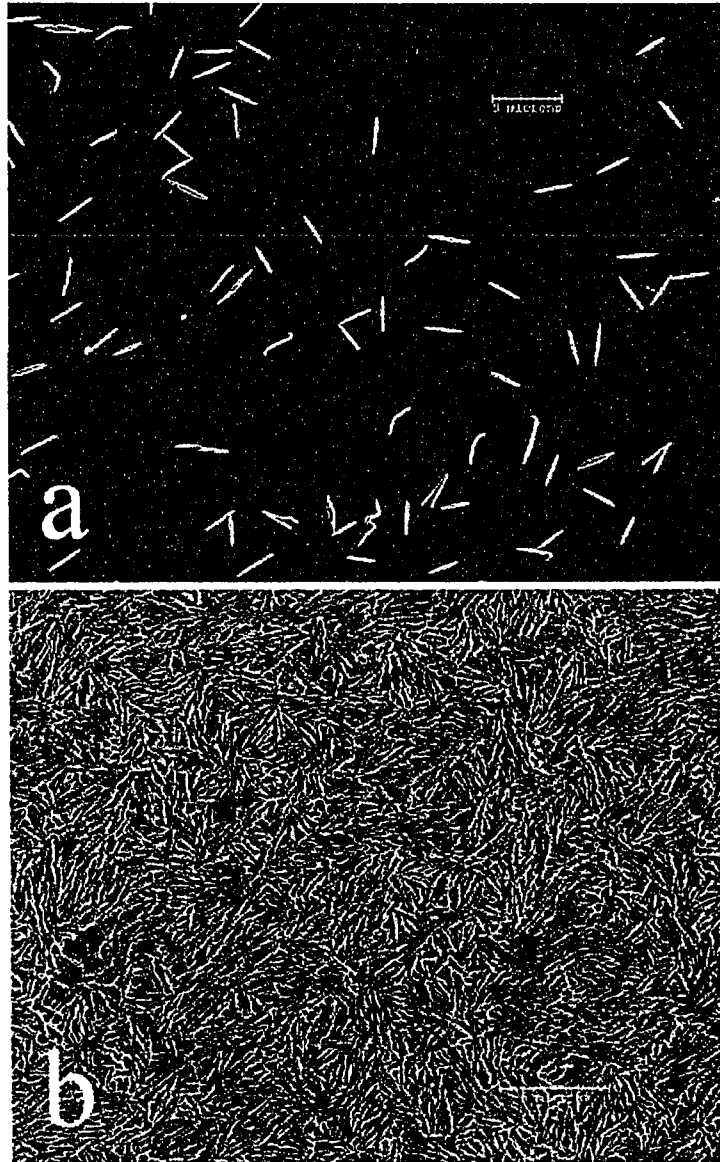
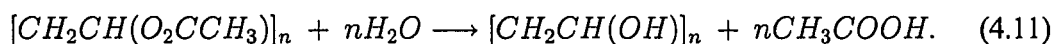


Figure 4.14: SEM picture of the rods we made. a) is a sample with dilute ellipsoid concentration. From which we can see individual rods' configuration. b) is a sample with high ellipsoid concentration.



means that the polymer film will be more crystalline, and consequently the more the film can be stretched without breakage, but it also means the film is more difficult to redissolve in water. Besides hydrolysis ratio, the other important parameter is molecular weight. In general, the larger the molecular weight, the more the polymer film can be stretched without breakage, but it also indicates the film is more difficult to redissolve in water. So we are balancing between the film's stretchability and the film's solubility. As showed in Table 4.9, we tried about a dozen different kinds of PVA, and we found the best one was the one with molecular weight at 124k-186k, and with hydrolysis ratio at 87-89%. For the kind of PVA we chose, its film can be stretched as many as 8 times, and at the same time it can be readily redissolved in hot water. The hydrolysis ratio of the PVA used by previous groups was at least 97%. This high hydrolysis ratio is the reason why they were only be able to redisperse small fraction of their final particles.



In previous work, particles embedded PVA film were stretched at  $\sim 200^\circ C$  in oil bath. The reason they use hot oil bath is because at  $\sim 200^\circ C$ , the organic particles and PVA film will burn out in air. It appeared that something happened to the PVA film when it was exposed to hot oil, because we found that PVA film's solubility in water was significantly decreased after it was exposed to hot oil. Instead of stretching PVA at  $\sim 200^\circ C$  in hot oil, we found we could stretch the particle embedded PVA film at  $135^\circ C$  in air. There was no combustion at this temperature and the embedded particles were uniformly stretched as

Table 4.9: PVA We Have Tried in Our Experiment

	Molecular Weight	Hydrolysis Ratio
1	89k-98k	99+%
2	85k-146k	99+%
3	124k-186k	99+%
4	31k-50k	98-99%
5	85k-146k	98-99%
6	124k-186k	98-99%
7	13k-23k	98%
8	50k-85k	97%
9	85k-146k	96%
10	13k-23k	87-89%
11	31k-50k	87-89%
12	85k-146k	87-89%
13	124k-186k	87-89%

the film being stretched. Since there was no contact between the PVA film and hot oil, the film was easily dissolved in hot water after stretching.

Another modification we made was to use water to dissolve the PVA film instead of using a mixture of isopropanol-water. We did control experiments and found PVA was hardly dissolved in isopropanol, and it was readily dissolved in water. We concluded that water was much a better solvent for PVA than isopropanol. Thus we use pure water as the solvent to dissolve PVA film.

## 4.3 Conclusion

In this chapter, we demonstrated how to synthesize monodispersed, spherical and non-spherical colloidal particles. We focused primarily on the synthesis of PMMA particles. For aqueous PMMA particles, we used surfactant free emulsion polymerization to achieve monodispersed, particles larger than 250 nm. For particles smaller than 250 nm, we turned to emulsion polymerization. We also described how to synthesize nonaqueous, fluorescently labelled PMMA particles. After exploring the synthesis of organic particles, we discussed inorganic particles' synthesis. We started with silica. We described in detail how to fabricate monodispersed, submicron silica beads. Furthermore, we discussed how to synthesize fluorescent labelled silica beads. The other inorganic particle we have synthesized is ZnS. ZnS has potential PBG application because of its high refractive index. We succeeded in synthesizing fairly monodispersed ZnS particles for further application. Finally, we demonstrated how we obtain monodispersed ellipsoid particles by mechanically stretching monodispersed PMMA and PS particles.

## Chapter 5

### Conclusions and Future Work

This thesis covers a wide range of topics in colloidal science, i.e. colloidal crystallization, semiflexible biopolymer and colloidal particle synthesis.

For colloidal crystallization, we succeeded in using two-dimensional grating templates to drive the growth of three-dimensional, face-centered-cubic (fcc) colloidal crystals by convective assembly. The template we used had square symmetry, corresponding to (100) planes parallel to the substrate. The square symmetry was transferred to the colloidal crystal and maintained throughout its growth of  $\sim 50$  layers. We used both electron microscopy and small-angle-X-ray scattering (SAXS) to characterize crystals growth on flat and templated substrate. SAXS measurements of the templated samples clearly show four-fold diffraction patterns that arise from fcc domains without stacking faults.

For semiflexible biopolymer work, we showed that direct visualization of semi-flexible polymers is a powerful tool to study polymer liquid crystals. Through direct visualization,

we demonstrated that semiflexible polymers dissolved in a background fd solution experience a coil-rod phase transition when we change the background solvent from isotropic to nematic. We also showed the polymer fluctuations are driven by fluctuations of the background nematic field. Dissolving semiflexible polymers in nematic liquid crystals provides a potentially easy way to achieve high alignment of biopolymers which is complimentary to existing techniques.

For colloidal particle synthesis, we demonstrated how to synthesize monodispersed, spherical and non-spherical colloidal particles. We focused primarily on organic PMMA particles. We extensively described the methods used to fabricate aqueous PMMA particles with sizes smaller than 250 nm and sizes bigger than 250 nm. We also described how to synthesize nonaqueous, fluorescently labelled PMMA particles. We then discussed our methods to fabricate both plain and fluorescently labelled monodispersed, submicron sized silica beads, and our methods to synthesize monodispersed ZnS particles, which have potential application in photonic bandgap materials. Finally, we demonstrated how to obtain monodispersed ellipsoid particles by mechanically stretching monodispersed PMMA and PS particles.

Beyond the achievements listed above, there are several open questions or new directions in connection with each topic.

For the template-directed convective assembly work, the mechanism of three dimensional convective assembly is still a poorly understood question. In order to make further

progress we must design an experiment to directly visualize the convective assembly induced crystallization process. This can probably be done with confocal microscopy. This direct visualization experiment will provide clear experimental details about the process. Furthermore, we can explore the effect of two-dimensional template's structure on the final three-dimension colloidal crystal driven by convective assembly. We can possibly synthesize bcc colloidal crystals as long as we prepare a deep enough template with correct pattern [(100)- or (110)- plane of bcc], and we can try to synthesize non-close-packing crystals out of convective assembly via templates.

For direct visualization of polymers in nematic liquid crystals, in order to complete our story, we will systematically explore actin's tangent-tangent correlation function (TTCF) in nematic fd solvents with various nematic strengths. Unlike the wormlike micelles, actin's rigidity helps us to achieve a more reliable TTCF data for distances smaller than  $0.5 \mu\text{m}$ . Another open question is the nature of hairpin defect structure. The hairpin's formation, evolution and dissolution has been studied theoretically but not experimentally. Finally, it is desirable to try to stretch DNA. To this end we might try nematic solvents with smaller length rods.

# Bibliography

- [1] J.C. Crocker and D.G. Grier, *Journal of Colloid and Interface Science* 179, 298(1996).
- [2] E.R. Weeks, J.C. Crocker, A.C. Levitt, A. Schofield, and D.A. Weitz, *Science* 287, 627(2000).
- [3] A.D. Dinsmore, and D.A. Weitz, *Journal of Physics: Condensed Matter* 14, 7581(2002).
- [4] U. Gasser, E.R. Weeks, A. Schofield, P.N. Pusey, and D.A. Weitz, *Science* 292, 258(2001).
- [5] B.J. Alder and T.E. Wainwright, *J. Chem. Phys.* 27, 1207(1957).
- [6] W.W. Wood, J.D. Jacobsen, *J. Chem. Phys.* 27, 1207(1957).
- [7] B.J. Alder, T.E. Wainwright, *J. Chem. Phys.* 27, 1208(1957).
- [8] W.G. Hoover, F.H.J. Ree, *Chem. Phys.* 49, 3609(1968).
- [9] B.J. Alder, W.G. Hoover, D.A. Young, *J. Chem. Phys.* 49, 3688(1968).

- [10] L. Onsager, Ann. NY Acad. Sci. 51, 627(1949).
- [11] P.M. Chaikin, and T.C. Lubensky, Principles of Condensed Matter Physics, Cambridge University Press, 1997.
- [12] Z. Dogic, A.P. Philipse, S. Fraden, J. Chem. Phys. 113, 8368(2000).
- [13] Z. Dogic, S. Fraden, Langmuir 16, 7820(2000).
- [14] Philosophical Transactions of the Royal Society of London A 359, 997 (2001).
- [15] M.A.Cotter and D.C. Wacker, Phys. Rev. A 18, 2669(1978).
- [16] M.A. Cotter, Hard particles theories of nematics, In G.R. Luckhurst and G.W. Gray, editors, The Molecular Physics of Liquid Crystals, 169, Academic Press, London, 1979.
- [17] Z.Y. Chen, Macromolecules 26, 3419(1993).
- [18] G.J. Vroege and H.N.W. Lekkerkerker, Rep. Prog. Phys. 55, 1241(1992).
- [19] R.D. Kamien, P.L. Doussal, and D.R. Nelson, Phys. Rev. A. 45, 8727(1992).
- [20] E. Yablonovitch, Phys. Rev. Lett. 58, 2059(1987).
- [21] C.M. Bowden, J.P. Dowling, and H.O. Everitt, J. Opt. Soc. Am. B. 10, 280(1993).
- [22] W.V. Smith, and R.H. Ewart, J. Chem. Phys. 16, 592(1948).
- [23] A.I. Campbell, and P. Bartlett, J Colloid Interf Sci. 256, 325(2002).



- [24] L. Antl, J.W. Goodwin, R.D. Hill, R.H. Ottewill, S.M. Owens, S. Papworth, and J.A. Waters, *Colloid Surf.* 17, 67(1986).
- [25] W. Stober, A. Fink, and E. Bohn, *J Colloid Interf Sci.* 26, 62(1986).
- [26] H. Katayama, S. Oda, and H. Kukimoto, *Appl. Phys. Lett.* 27, 697(1975).
- [27] C. Lawther, S. Fujita, and T. Takagi, *J. Appl. Phys.* 19, 939(1980).
- [28] T. Taguchi, and T. Yokogawa, *J. Phys. D.* 17, 1067(1984).
- [29] T. Sugimoto, G.E. Dirige, and A. Muramatsu, *J Colloid Interf Sci.* 180, 305(1996).
- [30] A. van Blaaderen, and A. Vrij, *Langmuir* 8, 2921(1992).
- [31] E. Matijevic, *Langmuir* 10, 8(1994).
- [32] C.C.Ho, A.Keller, J.A. Odell, and R.H. Ottewill, *Colloid Polym Sci* 271, 469(1993).
- [33] Y. Lu, Y. Yin, and Y. Xia, *Adv. Mater.* 13, 217(2001).
- [34] J.E.G.J. Wijnhoven, and W.L. Vos, *Science* 281, 802(1998).
- [35] E. Yablonovitch, *Nature* 401, 539(1999).
- [36] S.Y. Lin, E. Chow, V. Hietala, P.R. Villeneuve, and J.D. Joannopoulos, *Science* 282, 274(1998).
- [37] , G. Pan, R. Kesavamoorthy, and S.A. Asher, *Phys. Rev. Lett.* 78, 3860(1997).

- [38] , M. Megens, J.E.G.J. Wijnhoven, A. Lagenkijk, and W.L. Vos, *Phys. Rev. A.* 59, 271(1999).
- [39] , P.T. Tanev, M. Chibwe, and T.J. Pinnavaia, *Nature* 368, 321(1994).
- [40] K. Lewandowski, P. Murer, F. Svec, and J.M.J. Frechet, *Anal. Chem.* 70, 1629(1998).
- [41] D.B. Akolekar, A.R. Hind, and S.K. Bhargava, *J. Colloid Interface Sci.* 199, 92(1998).
- [42] P.N. Pusey, and W. van Megen, *Nature* 320, 340(1986).
- [43] A.D. Dinsmore, A.G. Yodh, and D.J. Pine, *Phys. Rev. E.* 52, 4045(1995).
- [44] A. van Blaaderen, R. Ruel, and P. Wiltzius, *Nature* 385, 321(1997).
- [45] S.R. Yeh, M. Seul, and B.I. Shraiman, *Nature* 386, 57(1997).
- [46] A. Yethiraj, and A. van Blaaderen, *Nature* 421, 513(2003).
- [47] J. Aizenberg, P.V. Braun, and P. Wiltzius, *Phys. Rev. Lett.* 84, 2997(2000)
- [48] D. Qin, Y.N. Xia, B. Xu, H. Yang, C. Zhu, and G.M. Whitesides, *Adv. Mater.* 11, 1433(1999).
- [49] B. Gates, D. Qin, and Y.N. Xia, *Adv. Mater.* 11, 466(1999).
- [50] R. Micheletto, H. Fukuda, and M. Ohtsu, *Langmuir* 11, 3333(1995).

- [51] N.D. Denkov, O.D. Velez, P.A. Kralchevsky, I.B. Ivanov, H. Yoshimura, and K. Nagayama, *Nature* 361, 26(1993).
- [52] A.S. Dimitrov, and K. Nagayama, *Langmuir* 12, 1303(1996).
- [53] P. Jiang, J.F. Bertone, K.S. Hwang, and V.L. Colvin, *Chem. Mater.* 11, 2132(1999).
- [54] K.P. Velikov, C.G. Christova, R.P.A. Dullens, and A. van Blaaderen, *Science* 296, 106(2002).
- [55] R. Rengarajan, P. Jiang, D.C. Larrabee, V.L. Colvin, and D.M. Mittleman, *Phys. Rev. B.* 64, 205103(2001).
- [56] K. Lin, J.C. Crocker, V. Prasad, A. Schofield, D.A. Weitz, T.C. Lubensky, and A.G. Yodh, *Phys. Rev. Lett.* 85, 1770(2000).
- [57] Y. Yin, and Y. Xia, *Adv. Mater.* 14, 605(2002).
- [58] T. Alfrey Jr., E.B. Bradford, J.W. Vanderhoff, and J. Oster, *J. Opt. Soc. Am.* 44 603(1954)
- [59] H.E. Kubitschek, *Nature* 192 1148(1961).
- [60] W. Luck, M. Klier and H. Wesslau, *Naturwissenschaften* 14, 485 (1963).
- [61] I.M. Krieger, and F.M. O'Neill, *J. Am. Chem. Soc.* 90, 3114(1968).
- [62] J.A. Davidson, and E.A. Collins, *J. Colloid Interface Sci.* 40, 437 (1972).
- [63] H.W. Deckman, and J.H. Dunsmuir, *Appl. Phys. Letters* 41, 377(1982).

- [64] S. Hayashi, Y. Kumamoto, T. Suzuki, and T. Hirai, *J. Colloid Interface Sci.* 144, 538(1991).
- [65] P.A. Kralchevsky, and K. Nagayama, *Langmuir* 10, 23(1994).
- [66] Y. Ye, F. Leblanc, A. Hache, and V. Truong, *Appl. Phys. Lett.* 78, 52(2001).
- [67] Y.N. Xia, E. Kim, X. Zhao, J.A. Rogers, M. Prentiss, and G.M. Whitesides, *Science* 273, 347(1996).
- [68] Y.H. Ye, S. Badilescu, V. Truong, P. Rochon, and A. Natansohn, *Appl. Phys. Lett.* 79, 872(2001).
- [69] D. Yi, E. Seo, and D. Kim, *Appl. Phys. Lett.* 80, 225(2002).
- [70] Y. Xia, J.J. McClelland, R. Gupta, D. Qin, X.M. Zho, L.L. Sohn, R.J. Celotta, G.M. Whitesides, *Adv. Mater.* 9, 147(1997).
- [71] S.A. Jenekhe, and X.L. Chen, *Science* 283, 372(1999).
- [72] S.B. Smith, L. Finzi, and C. Bustamante, *Science.* 258, 1122(1992).
- [73] T.T. Perkins, D.E. Smith, and S. Chu, *Science.* 276, 2016(1997).
- [74] M. Rief, M. Gantel, F. Oesterhert, J.M. Fernandez, and H.E. Ganb, *Science.* 276, 1109 (1997)
- [75] P. Cruzel, *Science.* 271, 792(1996).

- [76] M.D. Wang, H. Yin, R. Landick, J. Gelles, and S.M. Block, *Biophysics. J.* 72, 1335(1997).
- [77] T.R. Strick, J.F. Allemand, D. Bensimon, A. Bensimon, and V. Croquette, *Science* 271, 1835(1996).
- [78] V. Namasivayam, R.G. Larson, D.T. Burke, and M.A. Burns, *Anal. Chem.* 74, 3378(2002).
- [79] X. Michalet, R. Etkin, F. Fongrousse, S. Rousseaux, C. Schurra, N. Homigold, M. Van Slegtenforst, J. Wolfe, S. Povey, J.S. Beckmann, and A. Bensimon, *Science*. 277, 1518(1997).
- [80] A.R. Khokhlov and A.N. Semenov, *Physica* 112a, 605(1982).
- [81] A.R. Khokhlov and A.N. Semenov, *Physica* 108a, 548(1981).
- [82] R. Hentschke, *Macromolecules* 23, 1192(1990).
- [83] T. Odijk, *Macromolecules* 19, 2313(1986).
- [84] D.P. Dupre and S. Yang, *J. Chem. Phys.* 94, 7466(1991).
- [85] P.G. deGennes, *Polymer Liquid Crystals* Academic, New York, (1982).
- [86] J.P. Cotton and F. Hardouin, *Prog. Poly. Sci.* 22, 795(1997).
- [87] M.H. Li, A. Brulet, P. Davidson, P. Keller, and J.P. Cotton, *Phys. Rev. Lett.* 70, 2297(1993).

- [88] J. Sambrook, E.F. Fritsch, and T. Maniatis, in *Molecular Cloning: A Laboratory Manual* (Cold Spring Harbor Laboratory Press, 1989), chap.4, 2nd ed.
- [89] J.F. Leterrier, J. Kas, J. Hartwig, R. Vegners, and P.A. Janmey, *J. Biol. Chem.* 271, 15687(1996).
- [90] M.A. Hillmyer and F.S. Bates, *Macromolecules* 29, 6994(1996).
- [91] M.D. Wang et al., *Biophys. J.* 72, 1335(1997).
- [92] H. Aranda-Espinoza et al, to be published
- [93] Y.Y. Won et al., *Science* 283, 960(1999).
- [94] J.A. Spudich, S. Watt, *J Biol Chem* 246 (15), 4866(1971).
- [95] A. Ott, M. Magiasco, A. Simon, and A. Libchaber, *Phys. Rev. E.* 48, R1642(1993).
- [96] K.R. Purdy, Z. Dogic, S. Fraden, A. Ruhm, L. Lurio, and S.G.J. Mochrie, *Phys. Rev. E.* 67, 31708(2003).
- [97] F. Gittes, B. Mickey, J. Nettleton, and J. Howard, *J. Cell. Biol.* 120, 923(1993).
- [98] Z. Dogic and S. Fraden, *Liquid Crystals* 19, 459 (1995).
- [99] Z. Dogic and S. Fraden, *Langmuir* 16, 7820 (2000).
- [100] T. Odijk, *Macromolecules* 19, 2313 (1986).

- [101] Phase Transition, Vol.21, edited by B.J.Ackerson (Gordon and Breach, New York, 1990).
- [102] P.N. Pusey, in Liquids, Freezing and the Glass Transition, edited by D. Levesque, J. P. Hansen, and J. Zinn-Justin (Elsevier, Amsterdam, 1990).
- [103] J.E.G.J. Wijnhoven and W.L. Vos, Science 281, 802(1998).
- [104] S.E. Paulin and B.J. Ackerson, Phys. Rev. Lett. 64, 2663(1990).
- [105] B.J. Ackerson, Hard Sphere Crystallization by Sedimentation, in Statistical Physics, edited by M. Tokyama and I Oppenheim (World Scientific, Singapore, 1998).
- [106] J. Zhu, M. Li, R. Rogers, W. Meyer, R.H. Ottewill, STS-73 Space Shuttle Crew, W.B. Russel, and P.M. Chaikin, Nature 387, 883(1997).
- [107] U. Gasser, E.R. Weeks, A. Schofield, P.N. Pusey, D.A. Weitz, Science 292, 258(2001).
- [108] G.J. Vroege and H.N.W. Lekkerkerker, Rep. Prog. Phys. 55, 1241(1992).
- [109] Z. Dogic, Liquid Crystalline Phase Transition in Virus and Virus/Polymer Suspensions, Ph.D. Dissertation (2000).
- [110] from website: [info.med.yale.edu/genetics/ward/tavi/FISHdyes2.html](http://info.med.yale.edu/genetics/ward/tavi/FISHdyes2.html).